Dynamical Paleoclimatology of Mars

Thesis by

Alejandro Soto

In Partial Fulfillment of the Requirements

for the Degree of

Doctor of Philosophy

California Institute of Technology

Pasadena, California

2012

(Defended November 30^{th}, 2011)

To those without whom I would never have been able to do this work,

but who will never see it.

Acknowledgements

Back when I was an engineer at the Jet Propulsion Laboratory, I learned first hand that Caltech professors were generous and supportive, especially about science. I was a 20-something JPL engineer, which means that, like all 20-something JPL engineers, I was enthusiastic and fearless, completely confident that despite the hurdles we were going to get the bird off the ground and to whatever exotic planet the spacecraft was destined. And if I *did not actually know* what I was doing, which we all secretly feared, well, that was just another engineering challenge to be solved like all others.

With this passion, with this hubris, I naively demanded the various scientists with whom I worked to teach me the science for which we designed and built instruments and spacecraft. While I was working on designing within strict mass and constraints a Michelson interferometer destined for Mars, I insisted that members of the science team explain not just the needed resolution or sampling rate or whatever, but also explain what atmospheric chemicals were measured, with what did they react, and how this told us something interesting about the universe. And Professor Paul Wennberg did. And Professor Mark Richardson chimed in with more. This went on for a number of years until my hubris inspired me to go to graduate school and study planetary science.

Thus, I wandered over to Caltech to ask for advice on where to apply. That was all

I intended. I had no illusions about applying to Caltech, who had already rejected me for the undergraduate program (thank God!). But Paul and Mark decided to up the ante in terms of support and encouragement. I came to Caltech that day looking for advice on graduate schools and I left with orders to immediately apply to the Geological and Planetary Sciences (GPS) division at Caltech. And I did. So, thanks to Wennberg and Richardson for encouraging (demanding) my application to Caltech and supporting my admission into GPS.

My thesis research focused on the climate dynamics of the Martian atmosphere, and I benefited from an amazing amount of expertise at Caltech. I thank Dr. Mark Richardson and Professor Tapio Schneider for advising me on my thesis research. I learned much about climate dynamics and atmospheric modeling from them. Similarly, Professor Andrew Ingersoll, with his extensive knowledge of Martian science, was always available to discuss my research, for which I am very grateful.

In the long term, I am interested in the interaction between the atmosphere and the surface of terrestrial planets. Due to the diversity of research in the GPS division at Caltech, I learned more than was expected of a climate scientist about surface processes and sedimentology, though this fact is not reflected in this thesis. Professor John Grotzinger generously invited me on a sedimentology field trip where I became hooked on the subject. Professors Woody Fischer and Michael Lamb helped foster this interest by allowing me, a climate dynamicist, to sit in on and participate in their regular sedimentology group meetings. I thank all of these geologists for what they taught me about geology, and I hope to use this knowledge in future research.

Opportunities for learning come not only from the professors, but also from the post-doctoral scholars. The open and friendly environment of the GPS division fosters strong interaction between the postdocs and the grad students. I thank Dr. Deanne Rogers and Dr. Timothy Glotch for teaching me how to analyze Martian spectra. Meanwhile, I owe gratitude to Dr. Greg Wilson, Dr. Clair Newman, and Dr. Christopher Lee for teaching me how to work with the PlanetWRF climate model. I particularly thank Dr. Lee for years of patience in teaching me about the model, about programming, and about calculating climate diagnostics. I owe a few years worth of high-quality beer (i.e., not English beer) to that surprisingly patient and unsurprisingly sardonic Welshman.

Era bendecido con una familia que animaban la educación y la búsqueda de la ciencia. Tal suerte no puede ser ignorado. Sin duda, le debo a mi hermana, Dr. Victoria Maria Vazquez, por todo su apoyo. Por último, gracias a mis padres, Angel Manuel Soto y Myriam Migdalia Soto, quien apoyaron mis esfuerzos a lo largo de mi vida. Es una lástima que no sobrevivieron a ver este tesís.

Abstract

We investigated the dynamical paleoclimatology of Mars with a focus on three areas: large-scale dynamics, atmospheric collapse, and controls on precipitation and aridity of a warm, wet Mars. We explored the changes, and lack of changes, in the large-scale circulation over a range of atmospheric masses. We present the results here, with an emphasis on the response of the winds and the meridional transport.

The conditions for continuous condensation of the CO_2 atmospheres in the polar regions, often called 'atmospheric collapse', were explored by simulating the Martian atmosphere over a wide range of obliquities for a wide range of atmospheric thicknesses. As expected, atmospheric collapse occurs at low obliquities, but surprisingly, collapse occurs for high obliquities (up to 40°) for moderate atmospheric thicknesses (100s of millibars up to 1000 millibars). Using the MarsWRF model, we show that a competition between atmospheric heating feedbacks, including the greenhouse feedback and the heat transport feedback, and the condensation temperature feedback determines whether atmosphere collapse occurs.

Finally, we explored the precipitation and aridity of a warm, wet Mars with an active hydrological system. Even an extremely wet climate with a northern hemisphere ocean produces an extremely dry, desert climate in the southern hemisphere, with an equatorial

band of rain and runoff. Cross-equatorial flows deliver moist air from the northern ocean into the southern region, but topography and the distribution of land versus ocean limit the extent of the rainfall.

Contents

List of Figures

List of Tables

Chapter 1

Introduction

1.1 Initiations

This thesis focuses on two possible physical process of the Martian paleoclimate: the complete condensation of the CO_2 atmosphere and ocean-driven persistent rainfall. Part of the goal of this research was to use a fully developed Martian general circulation model (GCM) to capture the three-dimensional dynamics that control the paleoclimate. Rather than focus on the slow response of the climate system, as much of the previous Mars paleoclimate research has done, we were more interested in the Martian paleoclimate's seasonal and annual response to transitions and forcings in the climate system, i.e., condensation of the bulk atmosphere and ocean-driven precipitation, respectively. And with the work on Martian rainfall, we strove to provide a new perspective on the Mars scientific community's struggle to reconcile the contradiction between the current cold and dry Martian atmosphere and the ancient warm and wet Martian atmosphere.

1.2 Contradictions

Viewed from a great distance, or with poor resolution, the surface and atmosphere of Mars tell a consistent story, one of impacts craters and volcanos and desolate stretches filled with nothing but wind and sand. The thin atmosphere, with a global mean surface pressure of 6 to 7 millibars (mb), cannot sustain persistent liquid water, which leaves the atmosphere and surface extremely dry. The meager amount of water available is cold trapped in the polar regions, and the planet's hydrological system is limited to moving the water among the few cold traps available as reservoirs, including the north and south pole and the subsurface of the planet. The largely basaltic surface is riddled with impact craters, ranging from small meter scale craters to large craters that stretch over thousands of kilometers (and possibly a hemisphere (*Marinova et al.*, 2008; *Nimmo et al.*, 2008)). This view of Mars led some journalists covering the Mariner 4 fly-by of Mars, the first of its kind, to report that Mars appeared to be more like the Moon than the Earth (*Taylor*, 2010).

The closer one looks and the longer one looks, Mars begins to reveal itself to be far more vibrant. Made primarily of CO_2 and filled at times with dust, the Martian atmosphere exhibits a similar range of phenomena as Earth's atmosphere, from extremely local cyclonic activity like dust devils (*Thomas and Gierasch*, 1985) to large frontal storm systems (*Tillman et al.*, 1979). With global scale dust storms, the Martian atmosphere arguably surpasses the Earth's in terms of activity (*Zurek*, 1982). But still, this is a cold, dry atmosphere that flows over an ancient surface.

But once the dust is swept aside and ones looks closely at the surface of Mars, the consistency gives way to contradiction. The surface reveals features that seem to have been

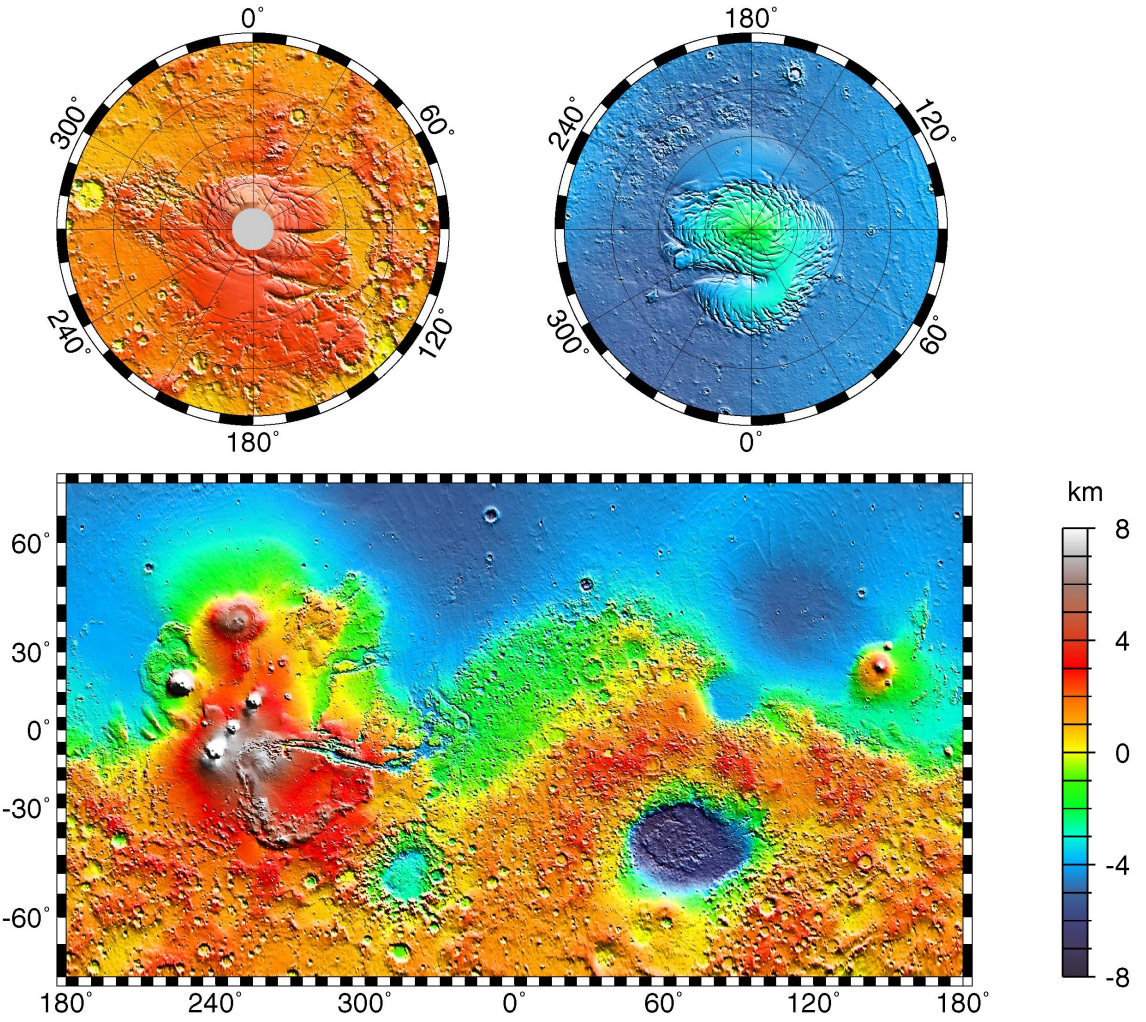

Figure 1.1: A map of the global topography of Mars. This topographic map highlights the primary features of the Martian surface, including: the elevation dichotomy between the northern and southern hemispheres; the Tharsis volcanic and tectonic region centered about the equator in the longitude range 220° E to 300° E; Olympus Mons at the northwestern edge of Tharsis; the Valles Marineris canyon system at the eastern end of Tharsis; the Hellas Basin at 45 S and 70 E; and the north and south polar deposits. This map uses an areocentric coordinate system with east longitude positive.

formed by liquid water, either standing or flowing (*Carr*, 1996) (see Figure 1.1). Valley networks and channels stretch across the surface, suggestive of riverbeds (*Baker et al.*, 1992); channel features terminate into delta-like deposits that look like snapshots of meandering river mouths (*di Achille and Hynek*, 2010); sedimentary deposits sit in the bottom of basins and craters like the detritus of ancient persistent water (*Malin and Edgett*, 2003); and even some ridges fleetingly hint at the possibility of a northern hemisphere ocean (*Head et al.*, 1999). Whereas the Martian atmosphere creates a dry though active climate, the surface geology reveals a wet paleoclimate with hydrological features resembling Earth's hydrology.

Reconciling this contradiction has been a goal of the Mars scientific community for decades (*Baker et al.*, 1992; *Carr*, 1996). With geological and geochemical observations as a guide, climate scientists have struggled to determine a paleoatmosphere state of Mars that can sustain persistent and flowing liquid water while also being susceptible to removal over the eons in order to arrive at the current Martian climate. The traditional strategy involves hypothesizing Martian paleoatmospheres of various thickness, all much greater than the current atmospheric thickness, and invoking various atmospheric chemical species that contribute to greenhouse warming (*Haberle*, 1998). The goal is to produce a Martian paleoclimate model that has persistent mean surface temperatures greater than the melting temperature of water, 273 K. This task has proven challenging and a clear solution remains to be found (*Haberle*, 1998).

Our contribution to this contradiction attempts to flip the process around. We ask, What would a warm and wet Mars look like? How would the warm and wet climate be recorded

by the surface and stored for posterity by the geology? Let us just prescribe a warm Mars and see the type of hydrological system that such a climate creates. If the patterns of rainfall and aridity produced by a warm and wet Mars produce surface geology that proved to be inconsistent with the current observations, then we would rule out that paleoclimate scenario. And if the results of the warm and wet Mars modeling proves to be consistent with surface geology, perhaps this would be useful process for constraining the type of paleoclimate

1.3 Transitions

With a primarily carbon dioxide (CO_2) atmosphere, the Martian atmosphere experiences a constant struggle between CO_2 gas and CO_2 ice due to the climate's proximity to the vapor pressure (or condensation) temperature of CO_2 . This leads to a unique feature of the Martian atmosphere: the CO_2 atmosphere freezes seasonally and possibly freezes secularly over tens to thousands of years. A fraction, sometimes a large one, of the atmosphere becomes surface ice. The consequences of this remarkable process were first explored by *Leighton and Murray* (1966), who hypothesized that the Martian atmospheric pressure was buffered by large sheets of perennial CO_2 ice in the polar regions. Although later observations proved that the most of the surface CO_2 ice is seasonal with only a small reservoir of perennial ice at the south pole (*Byrne and Ingersoll*, 2003), the condensation of atmospheric CO_2 is an important process in the evolution of the Martian atmosphere.

With a condensable primary atmospheric constituent, the Martian climate is sensitive to changes in insolation in the polar regions. Insolation variations driven by periodic orbital

changes of obliquity, eccentricity, and perihelion might have led to variations in surface pressure and climate state. Additionally, the secular increase in solar luminosity with the age of the solar system would have affected atmospheric changes due to CO_2 condensation. *Haberle et al.* (1994) and *Manning et al.* (2006), among others, have looked at how the evolution of the Martian atmosphere has responded to insolation driven condensation of CO_2 , among other climate controls. This previous work leveraged simple energy balance models to investigate long-term variations in the Martian climate. We, however, were intrigued by another puzzle: how does the condensation of the main atmospheric component of the Martian climate affect, and is affected, by the three-dimensional atmospheric circulation, for both thick and thin atmospheres? And for that matter, how does the circulation differ between a thick and thin Martian atmosphere?

1.4 Intentions

In the following chapters we investigate these two themes, contradictions and transitions. First, however, in Chapter 2 we study the large-scale circulation of the Martian atmosphere over a wide range of atmospheric thicknesses. We do so to provide better context about transport and dynamics in the Martian paleoclimate. Then, in Chapter 3 we tackle paleoclimate transition by looking at the dynamics of atmospheric collapse. Finally, in Chapter 4 we reach some bold conclusions about oceans, rainfall, and valley networks on Mars.

Chapter 2

Martian Climate Dynamics Through Thick and Thin

Abstract

We investigated the paleoclimate dynamics of thin and thick Martian atmospheres using a three-dimensional general circulation model. Both the global mean surface pressure and the solar luminosity were used as variable parameters in our study. We found that increasing the global mean surface pressure had the largest effect on large-scale circulation and the meridional transport of dry static energy. The condensation flow due to condensing CO_2 also has a large contribution to the mean circulation. Changing the solar luminosity profoundly changes the amount of CO_2 condensation at higher surface pressures.

2.1 Introduction

Since the beginning of the spacecraft exploration of Mars, the surface of Mars has provided evidence of an ancient hydrological cycle that included surface liquid water (*Carr*, 1996). Recent spacecraft observations have added to the evidence, including but not limited to

sedimentary features consistent with persistent flow of water (*Malin and Edgett*, 2003), precipitation formed crater morphologies (*Craddock and Howard*, 2002), precipitation fed lake basins (*Fassett and Head*, 2008), extensive precipitation fed valley networks (*Hynek et al.*, 2010), and evaporitic sediments consistent with groundwater and possibly surface water flow (*Squyres et al.*, 2004; *Grotzinger et al.*, 2005, 2006). These hydrological surface features imply a planetary climate history that begins warm and wet before transitioning to the current cold and dry climate (*Bibring et al.*, 2006; *Carr and Head III*, 2010). Since the current Martian climate can only sustain transient surface liquid water (*Richardson and Mischna*, 2005), the Martian atmosphere must have had a larger thermal capacity than currently available in order to achieve an ancient warm and wet climate. Although there are a number of proposals for warming ancient Mars, including impact-induced atmospheres (*Segura et al.*, 2008, 2002) and volcanically driven warming (*Johnson et al.*, 2009, 2008), to sustain long lived surface liquid water the ancient Martian atmosphere likely required a thicker atmosphere (*Haberle*, 1998).

The bulk of Martian paleoclimate modeling has focused on determining which combination of atmospheric mass and composition produces a warm Martian climate (*Haberle* (1998) provide and overview of this work). Early work relied on energy balance models to estimate the greenhouse effect of a number of atmospheric compositions (*Sagan and Mullen*, 1972; *Sagan et al.*, 1973; *Sagan*, 1977; *Pollack et al.*, 1987; *Kasting*, 1991; *Squyres and Kasting*, 1994; *Forget and Pierrehumbert*, 1997). Generally, the energy balance models required thick atmospheres, with mean surface pressures of 1 bar or greater, to achieve a climate warm enough to sustain surface liquid water. Some of the modeling

identified significant challenges in achieving these warm temperatures (*Squyres and Kasting*, 1994; *Kasting*, 1991; *Mischna et al.*, 2000). More recent paleoclimate modeling has utilized modern general circulation models (GCMs), again focusing on achieving a warm ancient climate. GCM simulations have explored various mechanisms for warming ancient Mars, including cyclical variations of the orbital parameters of Mars and the inclusion of secondary greenhouse gases, e.g., SO_2 species (*Johnson et al.*, 2008).

In lieu of focusing on mechanisms for warming ancient Mars, we investigated the dynamics of thicker Martian atmospheres. Regardless of the ability to sustain surface liquid water, if Mars once had a thicker atmosphere, this may have impacted the orientation and magnitude of surface winds generated by the general circulation. This possible change in wind regimes would have affected the type and distribution of aeolian activity on the surface of Mars and therefore the type of aeolian sedimentary deposits recorded in the rock. By studying the changes in the circulation due to a thicker Martian atmosphere, we have qualitatively identified possible changes to the aeolian regime in ancient Mars.

2.2 Paleoclimate simulations using the MarsWRF GCM

For these paleoclimate studies, we used a version of the Mars Weather Research and Forecasting (MarsWRF) general circulation model (GCM) (*Richardson et al.*, 2007), which is based on the NCAR Weather Research and Forecasting model (*Skamarock et al.*, 2005). MarsWRF solves the primitive equations on a finite difference mesh using an Arakawa C-grid (*Arakawa and Lamb*, 1997). As well, the model calculates CO_2 sublimation and condensation and adjusts the CO_2 ice and atmosphere inventories, along with the column

mass and pressure, accordingly. We did not include dust nor water vapor in our simulations, both because the quantity and distribution of dust and water in the the past are unknown and because the lack of dust and water simplifies this GCM study of thick Martian atmospheres. To calculate the radiative transfer, we used a two-stream radiation code that implements a k-distribution radiative transfer scheme (*Johnson et al.*, 2008). Simulations are run with a latitude and longitude resolution of $5^\circ \times 5^\circ$ and with 40 vertical levels provided by a terrain-following modified sigma vertical coordinate. The sigma vertical coordinate is defined as

$$\sigma = \frac{P - P_t}{P_s - P_t} \tag{2.1}$$

where P is the pressure in a given grid of the model, P_t is the pressure at the top of the model atmosphere, and P_s is the surface pressure. For surface temperature calculations, MarsWRF uses surface albedo and thermal inertia maps derived from MGS-TES observations in a multilayer subsurface thermal diffusion and surface energy balance model (*Christensen et al.*, 2001; *Putzig et al.*, 2005; *Richardson et al.*, 2007). The MarsWRF model uses the high resolution MOLA topography maps (1/32 degree) downsampled to the $5^\circ \times 5^\circ$ horizontal resolution of our simulations (*Smith et al.*, 2001). The current polar basal units are included for the current solar luminosity simulations, while the affect of removing the basal units will be explored for the faint young sun simulations.

MarsWRF was modified to handle changes in total atmospheric mass and solar insolation. For global mean surface pressures, we chose pressures that sample a wide range of possible paleoclimate scenarios: 6 mb, 60 mb, 300 mb, 600 mb, 1200 mb, and 3000 mb. The 3000 mb CO_2 inventory is the maximum inventory in our simulations since our

version of MarsWRF does not include a CO_2 cloud scheme that would be required at the higher atmospheric pressures (*Forget and Pierrehumbert*, 1997; *Mischna et al.*, 2000). The simulations are run for both current solar luminosity and 75% of current solar luminosity, often called the 'faint young sun' luminosity. These two values bookend the range of luminosities that Mars would have experienced since early in the solar system history until the present (*Gough*, 1981; *Gilliland*, 1989).

For many of the diagnostics calculated in this work, we analyzed the seasonal dynamics of the atmosphere, with a focus on capturing the dynamics associated with either the solstitial or equinoctial insolation. Each seasonal range has a length of 60° and is asymmetric about either a solstice or an equinox, as detailed in Table 2.1. This asymmetry accounts for both the short radiative timescale of thin atmospheres and the long radiative time scales of thick atmospheres.

Season	L_s Range
Northern Spring	$345 < L_s < 360$ and $0 < L_s < 45$
Northern Summer	$75 < L_s < 135$
Northern Fall	$165 < L_s < 225$
Northern Winter	$255 < L_s < 315$

Table 2.1: The range of solar longitudes of Mars, L_s, used for calculating each of the Martian seasons.

Over the lifetime of Mars, the Martian orbital parameters have oscillated with periods ranging from 10^4 to 10^6 years. The eccentricity varies from 0 to $\sim$0.14 with two oscillation periods, $\sim$96 kyr and $\sim$2 Myr, while the apsidal precession, which changes the time of year of perihelion passage, has a period of $\sim$175 kyr (*Ward*, 1974; *Laskar et al.*, 2004). These two parameters have a large impact on the annual insolation at Mars. The large range

in eccentricity can lead to a seasonal insolation that varies by as much as 40% (*James and North*, 1982). The changing time of perihelion changes the season in which peak insolation falls on the surface of Mars. The oscillating obliquity, with a period of 120 kyr and a range of possible values from 0° to ~80°, creates an even larger change in the distribution of insolation at the surface of Mars (*Ward*, 1974; *Laskar et al.*, 2004). The combination of these parameter spaces creates a large number of possible paleoclimates. For this investigation, we chose to limit these orbital parameters, thus allowing us to isolate the impact of increasing atmospheric thickness on the paleoclimate. We used an obliquity of 25°, which is similar to the current Martian obliquity, and zero eccentricity.

Mean Pressure	Solar Luminosity
6 mb	100%
60 mb	100%
300 mb	100%
600 mb	100%
1200 mb	100%
3000 mb	100%
6 mb	75%
60 mb	75%
300 mb	75%
600 mb	75%
1200 mb	75%
3000 mb	75%

Table 2.2: The simulations conducted for this investigation, where the obliquity is 25° and the eccentricity is zero for each simulation.

The goal of these simulations is to highlight the aspects of climate dynamics that are driven by the atmospheric thickness. Hence, we have omitted other features of the Martian system, such as eccentricity or water vapor. This work provides the foundation for future

investigations of these other features. This strategy is reflected in Table 2.2, which lists the types of simulations conducted.

2.3 Results from the current luminosity simulations

We first look at the current luminosity simulations, since these simulations can more easily be compared to current Mars climate dynamics. The thin atmosphere, i.e., 6 mb, simulation will differ from current Mars in the lack of eccentricity driven variations in seasonal insolation and the lack of dust and water vapor radiative feedbacks. From this point we build an understanding of how the thicker atmospheres are changing the dynamics of the climate.

2.3.1 CO_2 condensation

The relatively high condensation temperature of CO_2 gas, compared to the volatiles in other solar system atmospheres, combined with the amount of insolation that reaches the Martian surface results in the condensation of the Martian atmosphere in the polar regions. This unique characteristic of the Martian atmosphere was identified early in the history of the exploration of Mars (*Leighton and Murray*, 1966) and observed by subsequent spacecraft missions (*Hess et al.*, 1979; *Kieffer*, 1979; *Hess et al.*, 1980; *Paige and Ingersoll*, 1985; *Tillman et al.*, 1993; *Kelly et al.*, 2006). For the current Martian atmosphere, a seasonal balance exists between the atmospheric CO_2 and surface ice CO_2 , where CO_2 frost condenses on to the winter pole and sublimates off of the summer pole (*Kieffer*, 1979; *Paige and Ingersoll*, 1985; *Titus et al.*, 2008). Although there exists a permanent CO_2 ice cap

in the current south pole of Mars, Mars GCMs generally do not capture this phenomenon in the current Martian atmosphere without being specifically tuned to do so (*Guo et al.*, 2010). For this work, no perennial CO_2 ice cap is forced to exist in the simulations, but rather the CO_2 is allowed to equilibrate between gas and ice based on the energy balance of the model, which may or may not lead to the formation of perennial CO_2 ice.

Figure 2.1 shows the zonal mean accumulation of ice as a function of time for five simulation years, including the early spin-up of the model (roughly the first 6 months). For the 6 mb and 3000 mb simulated atmospheric thicknesses, the 25° obliquity simulations produce seasonal CO_2 caps at each pole, but no perennial ice. For the 60 mb, 300 mb, 600 mb, and 1200 mb simulations, there is a perennial and growing CO_2 ice cap in the northern hemisphere along with the seasonal caps in both hemisphere. Since these simulations have zero eccentricity, the total summer insolation is the same for northern summer and southern summer. Thus, the asymmetry in CO_2 ice deposition is created by the different surface temperatures due to the different topography between the northern polar region and the southern polar region. The higher elevations of the southern region have lower surface pressure, which leads to a lower condensation temperature due to the Clausius-Clapeyron relationship. On the other hand, the lowlands in the northern hemisphere have a higher surface pressure and thus a higher condensation temperature which leads to the thicker CO_2 ice deposits and the perennial ice in the middle atmospheric thicknesses.[1]

The thickest atmospheres deposit CO_2 ice onto Olympus Mons, as seen around 20° N and -130° E in Figures 2.1(e) and 2.1(f). This CO_2 ice deposition represents a competi-

[1]The physics that control whether perennial ice forms in the simulations are explored in a later chapter of this thesis.

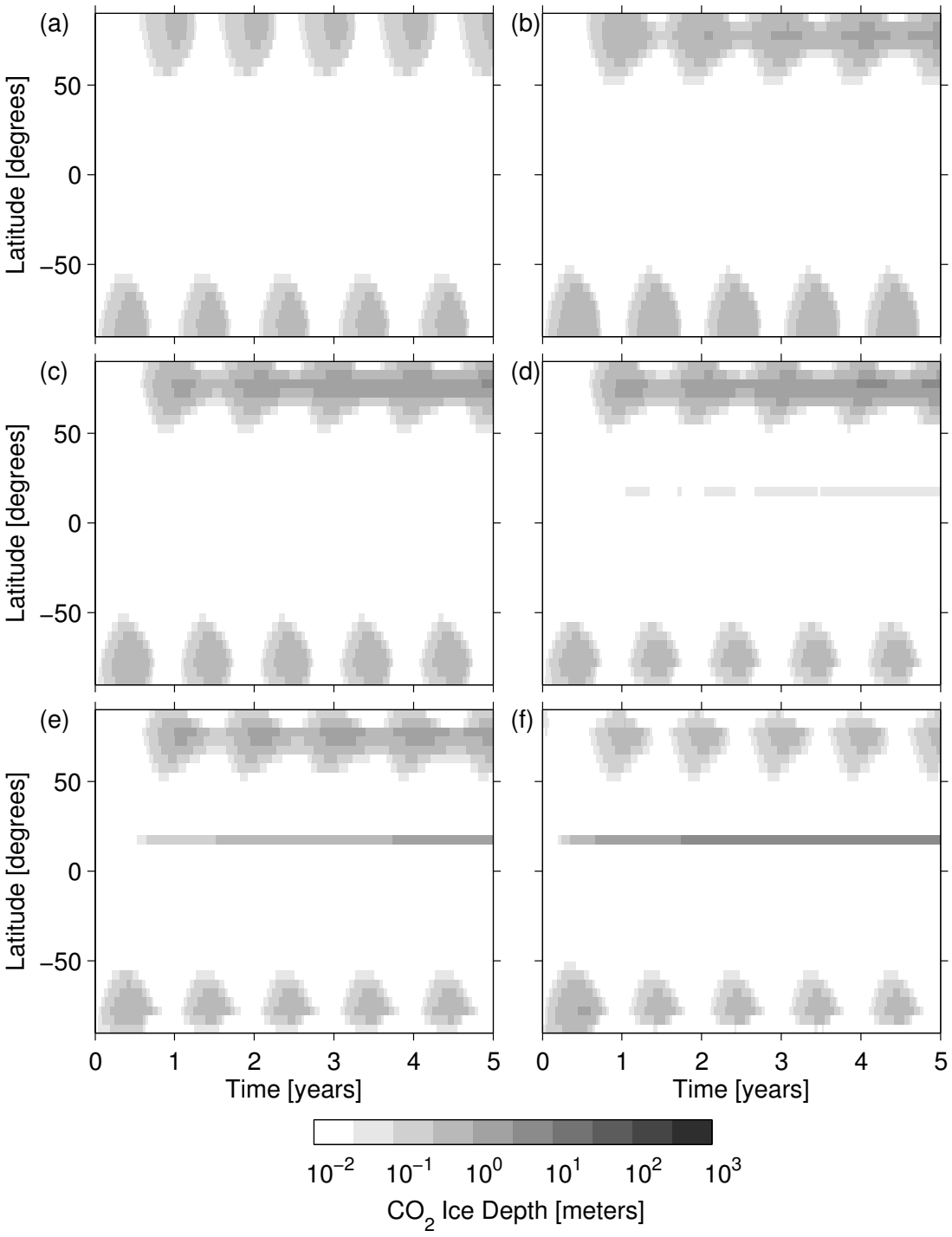

Figure 2.1: Zonal CO_2 ice versus time for the current luminosity. The plots include the following initial surface pressures: (a) 6 mb, (b) 60 mb, (c) 300 mb, (d) 600 mb, (e) 1200 mb, and (f) 3000 mb. The plots show the thickness of CO_2 ice assuming an ice density of 1600 kg/m^3 (*Kieffer*, 2007).

tion between the changing surface temperature due to local atmospheric surface pressure and the changing CO_2 condensation temperature, which also depends logarithmically on atmospheric surface pressure. To first order, the surface temperature at Olympus Mons is controlled by the greenhouse effect of the atmospheric column that resides over the mountain. This surface temperature will grow linearly with increasing surface pressure. The condensation temperature, however, is a function of the Clausius-Clapeyron relation and thus the condensation temperature grows logarithmically with surface pressure. As the simulations move to thicker atmospheres, the rate of increase in condensation temperature outstrips the rate of increase in surface temperature and thus the deposition of CO_2 ice on Olympus Mons becomes favorable. Ultimately, the combination of basal ice melting and the slopes of the Olympus Mons region would limit the deposition, but this phenomena is not captured in our five year simulations.[2]

2.3.2 Temperature and winds

A thicker Martian atmosphere leads to the homogenization of the zonal mean air temperature and an associated weakening of the zonal jets in the midlatitudes. Figures 2.2 to 2.5 show the zonal mean temperature and zonal wind for the four seasons of the Martian year. In each figure, the results of the six different atmospheric thickness simulations are shown, ranging from an atmosphere with mean surface pressure of $\sim$6 mb to $\sim$3000 mb.

The Martian spring, shown in Figure 2.2, shows how the climate responds to a latitudinally symmetric insolation. In each of the simulations, the peak insolation occurs near the

[2]Similarly, the limits of CO_2 ice deposit height on Olympus Mons due to basal melting is addressed in more details in a later chapter.

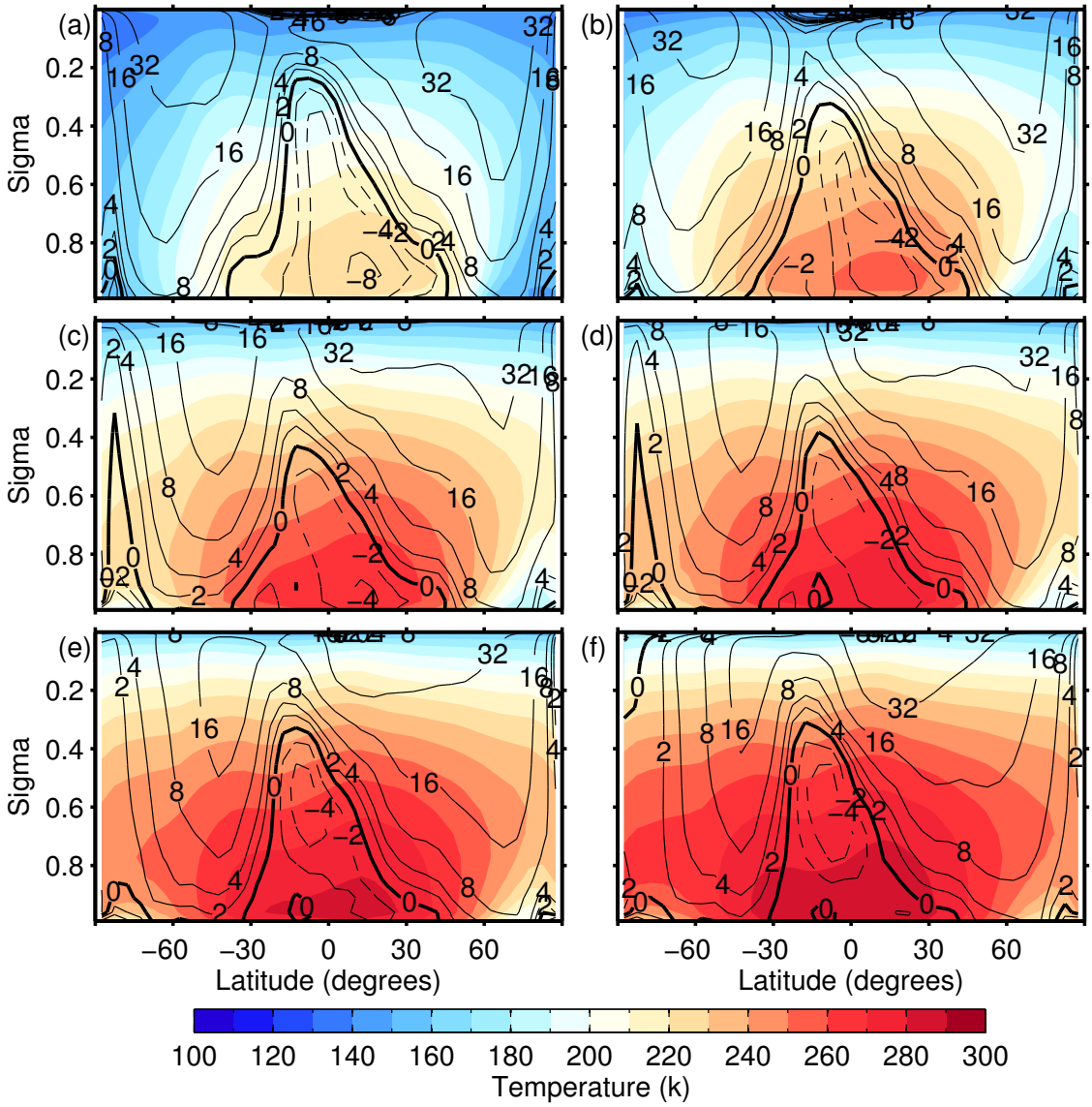

Figure 2.2: The seasonal mean of the zonal mean temperature (K) and zonal wind (m s^{-1}) for the northern spring ($L_s = 345$ to $L_s = 45$) as a function of mean surface pressure. The figure shows mean surface pressures of (a) 6 mb, (b) 60 mb, (c) 300 mb, (d) 600 mb, (e) 1200 mb, and (f) 3000 mb. The color contours represent air temperature, ranging from 100 K to 300 K. The solid black lines are contours of positive zonal wind with contour levels that uses a geometric progression (2, 4, 8, 16, ...) for level spacings. The bolded solid black line is the zero zonal wind contour. The dashed black lines are contours of negative zonal wind with contour levels that uses a geometric progression (-2, -4, -8, -16, ...) for level spacings.

equator with decreasing temperatures poleward. For the 6 mb simulation, Figure 2.2(a), the near surface temperature gradient in the tropics is $\sim$10 K over 30° of latitude. Once you reach the extratropics, this horizontal temperature gradient, for the same latitudinal extent, reaches $\sim$30 K in the southern hemisphere and $\sim$5 K in the northern hemisphere. These sharp horizontal temperature gradients in the extratropics are reflected in the zonal wind through the thermal wind balance, and thus in the extratropics there is a strong vertical zonal wind shear due to the horizontal temperature gradient. This vertical zonal wind peaks in both hemispheres at an altitude of roughly $\sigma \sim 0.3$ and is located over the steepest portion of the horizontal gradient. In both the 6 mb and 60 mb simulations, the two thinnest atmosphere simulations in this investigation, the vertical zonal wind shear generates a zonal jet with peak speeds of $\sim$32 m s^{-1} in both hemispheres. Starting with the 300 mb simulation, however, the thicker atmospheres have a significantly smaller horizontal temperature gradient and weaker zonal jets. The 1200 mbar simulation, which is representative of the other thick atmospheres, the extratropical temperature gradient is $\sim 10^\circ$ to $\sim 20^\circ$ in the southern hemisphere and $\sim 30^\circ$ in the northern hemisphere. This leads to a weaker zonal jet in the southern hemisphere, where wind speeds peak at $\sim$16 m s^{-1}, and a higher altitude peak zonal wind ($\sim$32 m s^{-1} at $\sigma = 0.2$) in the northern hemisphere. Surface winds, both extratropical westerlies and tropical easterlies, experience a similar decrease in wind speed for the thicker atmosphere simulations.

During northern summer the air temperature responds to the latitudinally asymmetric insolation by shifting warm temperatures poleward, well past the northern summer maximum subsolar point and into the lower north polar regions (see Figure 2.3). The low

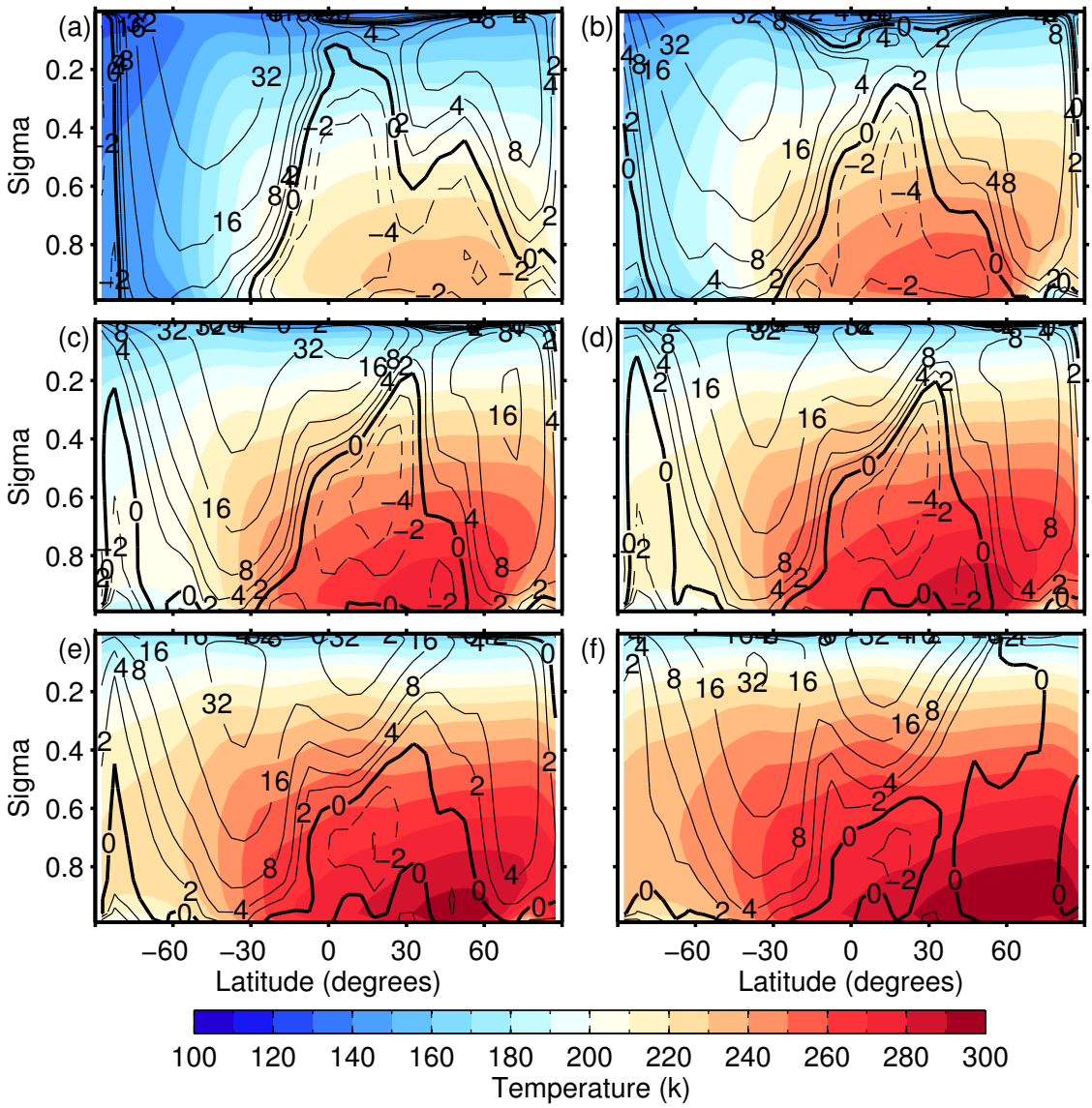

Figure 2.3: The seasonal mean of the zonal mean temperature (K) and zonal wind (m s^{-1}) for the northern summer ($L_s = 75$ to $L_s = 135$) as a function of mean surface pressure. The figure shows mean surface pressures of (a) 6 mb, (b) 60 mb, (c) 300 mb, (d) 600 mb, (e) 1200 mb, and (f) 3000 mb. The color contours represent air temperature, ranging from 100 K to 300 K. The solid black lines are contours of positive zonal wind with contour levels that use a geometric progression (2, 4, 8, 16, ...) for level spacings. The bolded solid black line is the zero zonal wind contour. The dashed black lines are contours of negative zonal wind with contour levels that use a geometric progression (-2, -4, -8, -16, ...) for level spacings.

thermal inertia of the Martian surface helps create this large poleward shift in peak near surface air temperatures by rapidly responding to changing insolation that is absorbed at the surface. In the 6 mb simulation, Figure 2.3(a), the warm temperatures (210 K to 240 K) stretch from the north polar region to the southern tropics. In the southern midlatitudes and extratropics there is a strong horizontal temperature gradient, as the near surface air temperature decreases by $\sim$50 K over 30° of latitude. The strong temperature gradient decreases as the atmospheric thickness is increased. For the 300 mb simulation, Figure 2.3(c), the southern midlatitudes horizontal temperature gradient is only $\sim$30 K over 30° of latitude, and for the 3000 mb simulation, Figure 2.3(f), the temperature gradient is $\sim$20 K over 30°. The strongest change in the horizontal temperature gradient occurs in the first few hundred millibar of atmospheric thickness. Once the simulation has greater than 50 times the atmospheric mass as current Mars then the climate transitions to a more uniform temperature distribution with smaller horizontal temperature gradients.

As with the northern spring simulations, the zonal winds are weaker at all heights in the thicker atmosphere northern summer simulations. The strength and depth of the southern zonal jets are diminished at high atmospheric thicknesses as compared to the 6 mb simulation, while surface winds in the midlatitudes are smaller in the thicker atmosphere simulations, by a factor of two or greater. Unlike the northern spring simulations, the location of the transition from equatorial easterlies to midlatitude westerlies has shifted in both latitude and height between the thin and thick atmosphere simulations. For the thicker atmosphere simulations, 1200 mb and 3000 mb, for example, the easterly-westerly transition has shifted northward and downward. For the 3000 mb simulation, the northern polar jet

has disappeared completely, as seen in Figure 2.3(f), and at the upper heights the westerly flow has pushed into almost the entire northern hemisphere. This wind structure is very different from the northern summer zonal wind structure of the 6 mb simulation, as seen in Figure 2.3(a), where there is a distinct and relatively strong north polar jet.

The northern fall and northern winter temperature fields, shown in Figure 2.4 and Figure 2.5, are similar to their seasonal counterpart. Again the increasing atmospheric thickness leads to a homogenization of horizontal temperatures. And again this decrease in horizontal temperature gradients leads to smaller zonal winds due to the weaker vertical wind shear created by the thermal wind balance. The northern winter simulations have one significant difference that exists at almost all atmospheric thicknesses: the southern upper atmosphere structure includes multiple zonal jets (Figure 2.5).

Maps of the surface wind provide another view of the transition in dynamics from thin to thick atmospheres. For example, Figure 2.6 shows a map of surface winds and a histogram of zonal wind speeds both for the 6 mb thin atmosphere (Figure 2.6(a)) and the 1200 mb thick atmosphere (Figure 2.6(b)) during northern spring. In each wind map, both wind direction and speed are indicated by an arrow, thus allowing us to determine the seasonal flow of the wind at the surface. For each map, there is an associated histogram showing the distribution of zonal wind speeds.

The near surface winds are strongly influenced by the large topographic variations of the Martian surface. This influence is still evident in the thicker atmosphere simulations. In both the 6 mb and 1200 mb simulations, for all seasons, there are persistent eddies associated with the Olympus Mons and Tharsis Mons regions in the northern hemisphere

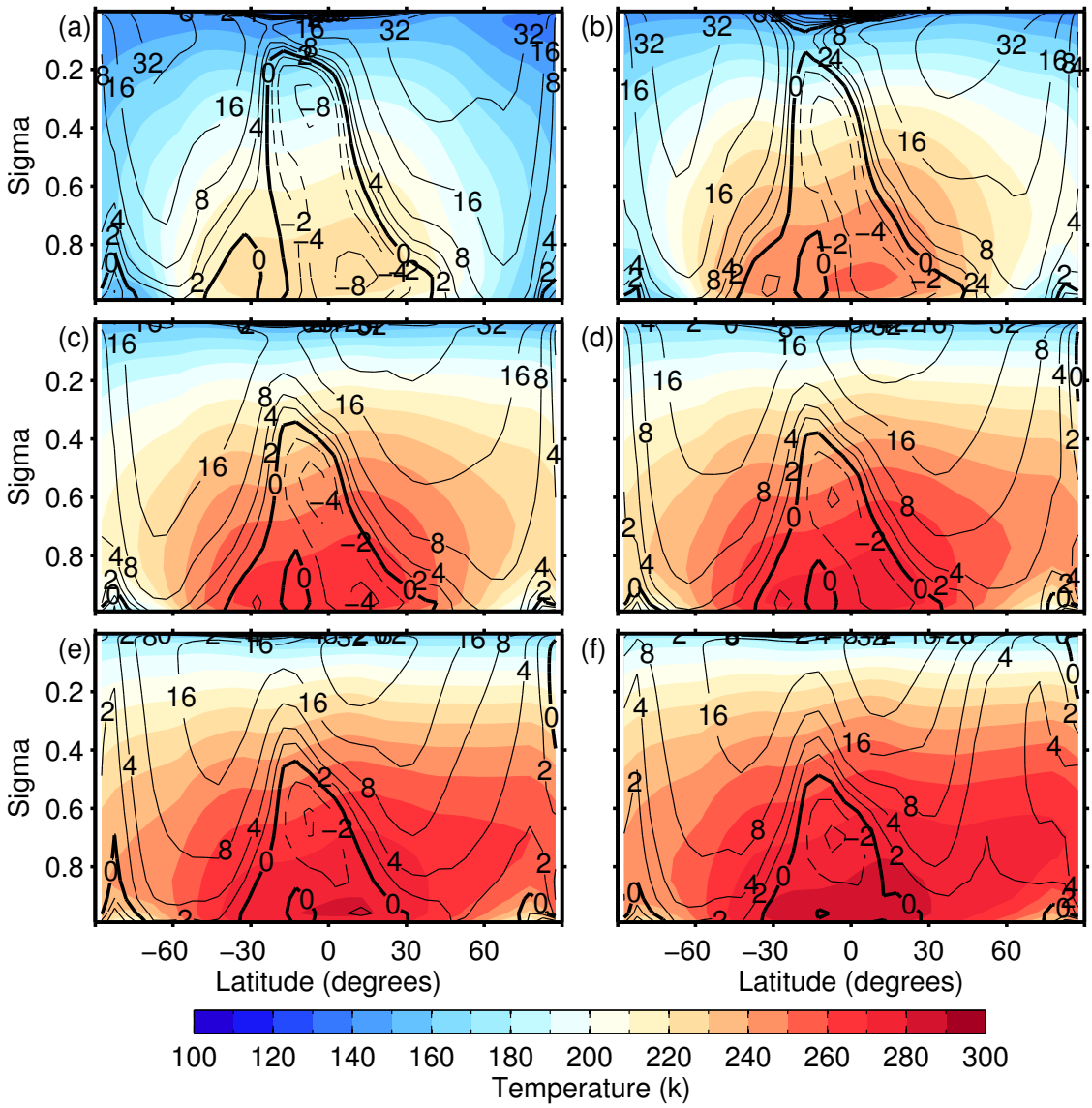

Figure 2.4: The seasonal mean of the zonal mean temperature (K) and zonal wind (m s^{-1}) for the northern fall ($L_s = 165$ to $L_s = 225$) as a function of mean surface pressure. The figure shows mean surface pressures of (a) 6 mb, (b) 60 mb, (c) 300 mb, (d) 600 mb, (e) 1200 mb, and (f) 3000 mb. The color contours represent air temperature, ranging from 100 K to 300 K. The solid black lines are contours of positive zonal wind with contour levels that use a geometric progression (2, 4, 8, 16, ...) for level spacings. The bolded solid black line is the zero zonal wind contour. The dashed black lines are contours of negative zonal wind with contour levels that use a geometric progression (-2, -4, -8, -16, ...) for level spacings.

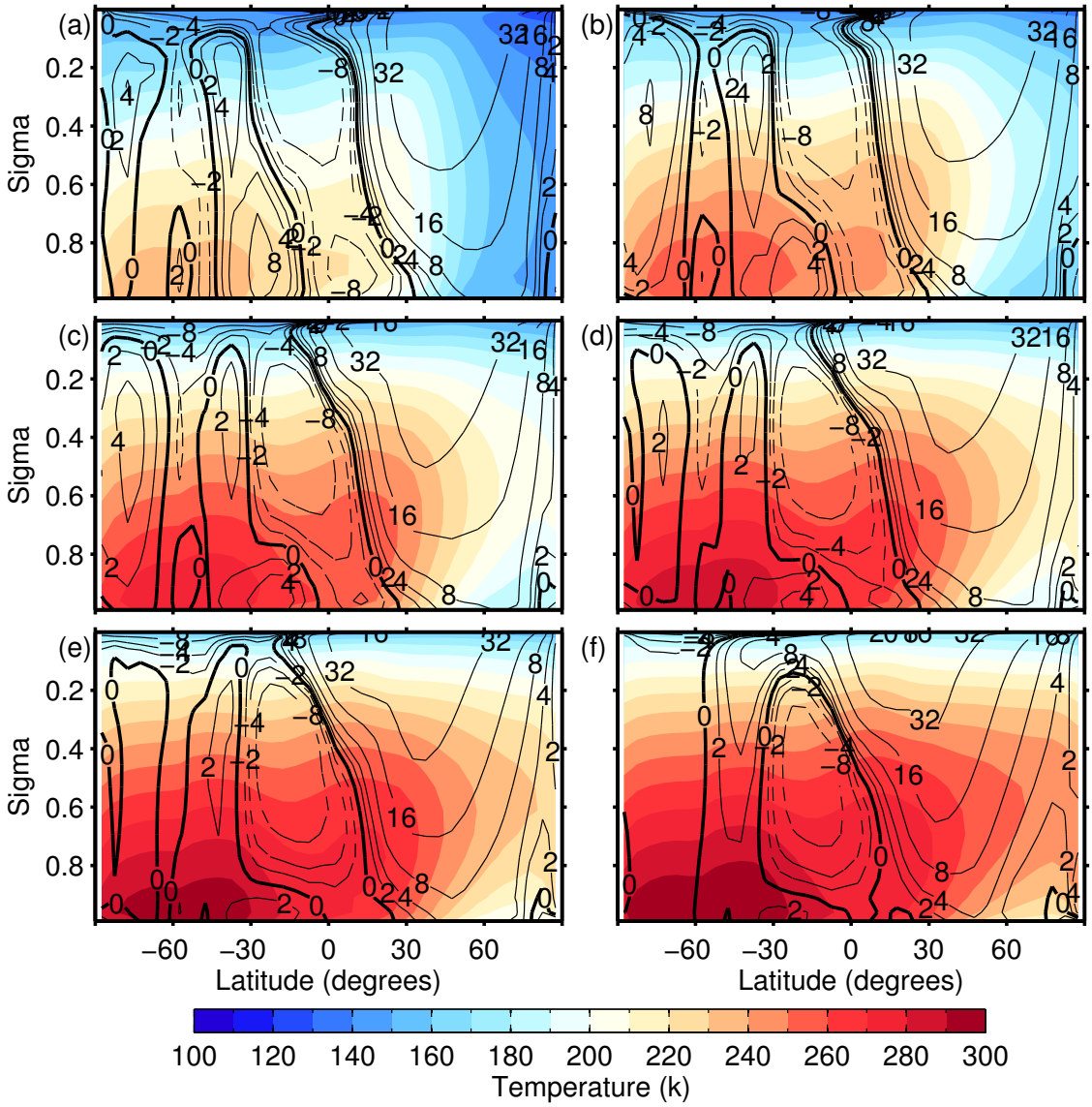

Figure 2.5: The seasonal mean of the zonal mean temperature (K) and zonal wind (m s^{-1}) for the northern winter ($L_s = 255$ to $L_s = 315$) as a function of mean surface pressure. The figure shows mean surface pressures of (a) 6 mb, (b) 60 mb, (c) 300 mb, (d) 600 mb, (e) 1200 mb, and (f) 3000 mb. The color contours represent air temperature, ranging from 100 K to 300 K. The solid black lines are contours of positive zonal wind with contour levels that use a geometric progression (2, 4, 8, 16, ...) for level spacings. The bolded solid black line is the zero zonal wind contour. The dashed black lines are contours of negative zonal wind with contour levels that use a geometric progression (-2, -4, -8, -16, ...) for level spacings.

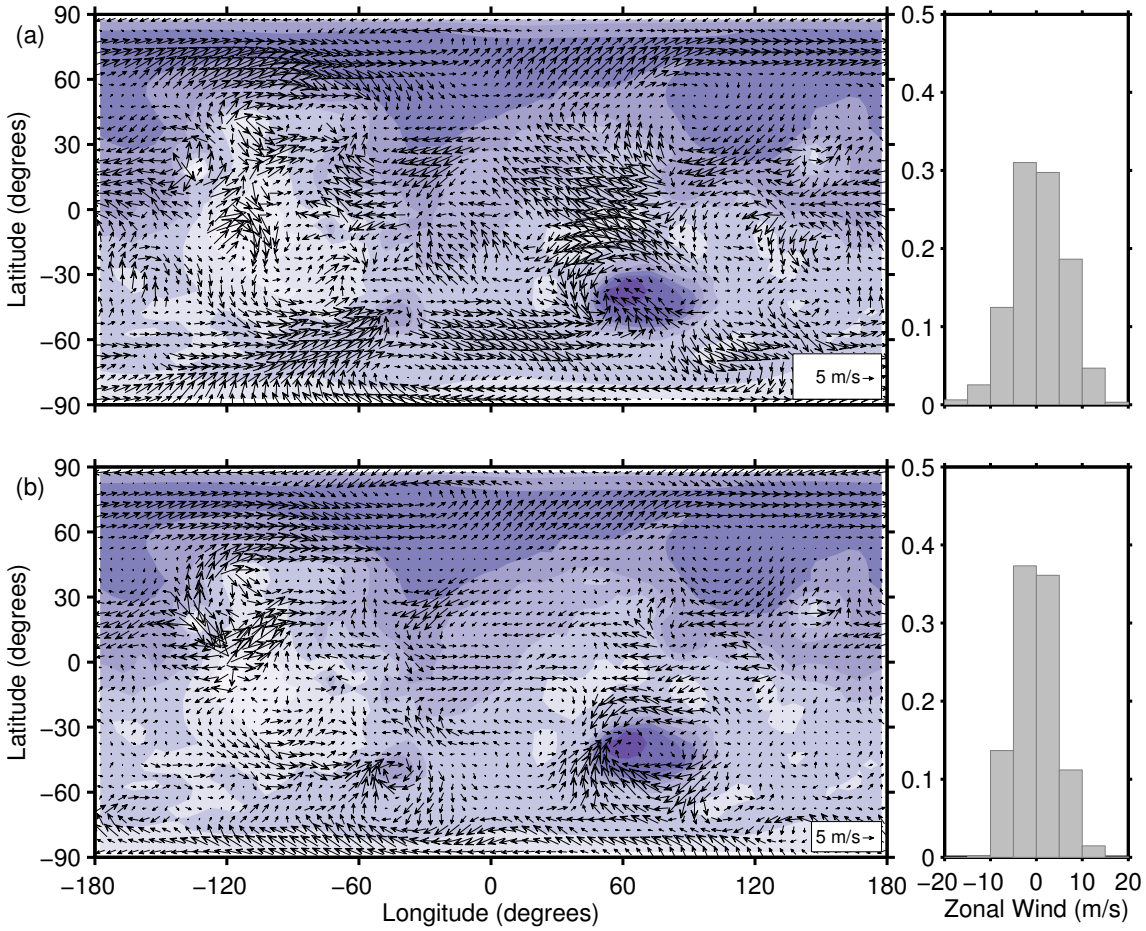

Figure 2.6: A map of surface winds and a histogram of the zonal wind speeds for (a) the 6 mb simulation and (b) the 1200 mb simulation. These results are for northern spring ($L_s = 345$ to $L_s = 45$). The vectors represent the resulting wind field due to the zonal and meridional winds. High elevation topography is shown as light purple contours and low elevation topography is shown as dark purple. The histogram shows the distribution of zonal wind speeds in 1 m s^{-1} bins. The 6 mb simulation has a mean zonal wind speed of 0.7 m s^{-1} and a standard deviation of zonal wind speeds of $\pm$ 6 m s^{-1}, while the 1200 mb simulation has a mean zonal wind speed of 0 m s^{-1} and a standard deviation of zonal wind speeds of $\pm$ 4 m s^{-1}.

as well as standing waves over the Argyre and Hellas Basins in the southern hemisphere (see Figures 2.6 through 2.9). These stationary eddies have winds that are up to two times stronger in the 6 mb simulation.

While the same topographically driven winds appear in both thin and thick atmosphere simulations, many of the planetary scale waves seen in the 6 mb simulation are missing or almost completely missing in the thicker, 1200 mb simulation. For example, in the northern spring, fall, and winter, the 6 mb simulation shows a strong planetary wave in the northern lowlands above 60° N (see Figures 2.6(a), 2.8(a), and 2.9(a)). This wave spans almost 20° of latitude in the northern hemisphere and consists of winds with speeds mostly ~ 10 m s^{-1} that race around the northern lowlands. While this planetary wave is still evident, though weak, in the 1200 mb northern spring simulation (Figure 2.6(b)), the planetary wave is almost nonexistent in the 1200 mb atmosphere during northern fall and winter.

The histograms in Figures 2.6 through 2.9 show how the distribution of zonal winds speeds, which are the dominant component of the total wind speeds, differs for the thicker atmosphere simulations. In the northern spring case, the 6 mb simulation has a larger range of maximum and minimum wind speeds than the 1200 mb simulation. In Figure 2.6(a), the mean zonal wind speed is ~ 0.7 m s^{-1} with a standard deviation of $\pm$ 6 m s^{-1} and the maximum and minimum wind speeds approach $\pm$ 20 m s^{-1}. The 1200 mb simulation has a narrower distribution of zonal winds with a standard deviation of zonal wind speeds of $\pm$ 4 m s^{-1} and peak zonal winds speeds less than $\pm$ 15 m s^{-1}. This narrowing of the zonal wind speed distribution at thicker atmospheres and weakening of the maximum zonal wind speed is consistent with both the zonal wind and temperature data in Figures 2.2 to 2.5

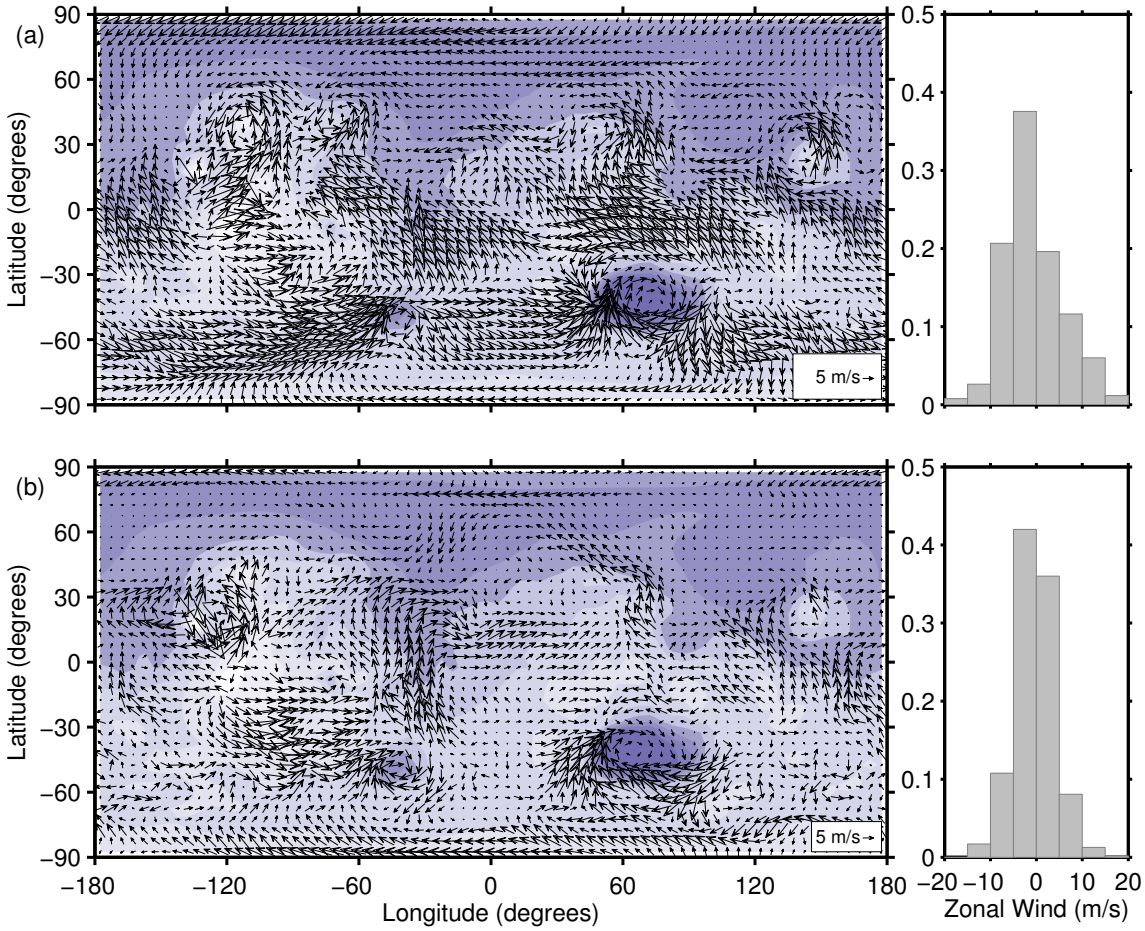

Figure 2.7: A map of surface winds and a histogram of the zonal wind speeds for (a) the 6 mb simulation and (b) the 1200 mb simulation. These results are for northern summer ($L_s = 75$ to $L_s = 135$). The vectors represent the resulting wind field due to the zonal and meridional winds. High elevation topography is shown as light purple contours and low elevation topography is shown as dark purple. The histogram shows the distribution of zonal wind speeds in 1 m s^{-1} bins. The 6 mb simulation has a mean zonal wind speed of 0.6 m s^{-1} and a standard deviation of zonal wind speeds of $\pm$ 6 m s^{-1}, while the 1200 mb simulation has a mean zonal wind speed of 0.4 m s^{-1} and a standard deviation of zonal wind speeds of $\pm$ 4 m s^{-1}.

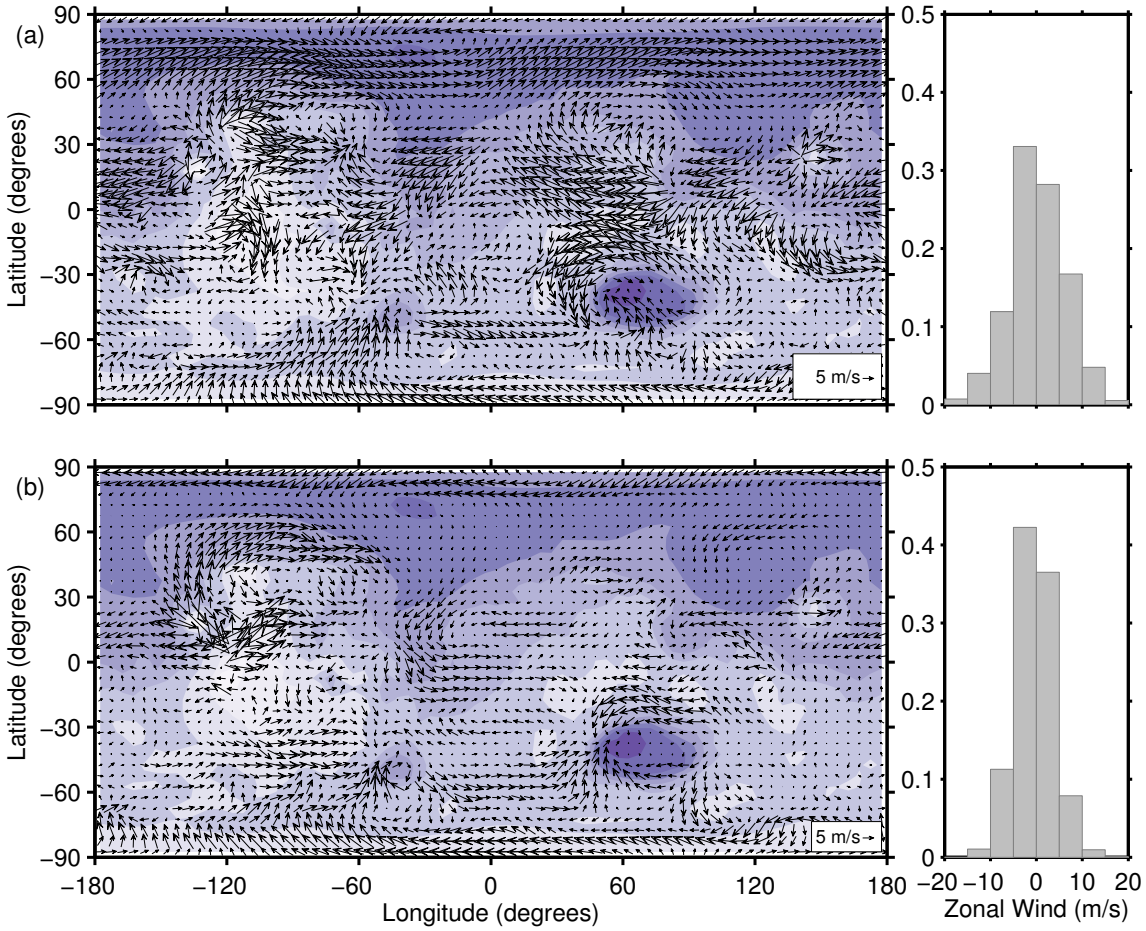

Figure 2.8: A map of surface winds and a histogram of the zonal wind speeds for (a) the 6 mb simulation and (b) the 1200 mb simulation. These results are for northern fall ($L_s = 165$ to $L_s = 225$). The vectors represent the resulting wind field due to the zonal and meridional winds. High elevation topography is shown as light purple contours and low elevation topography is shown as dark purple. The histogram shows the distribution of zonal wind speeds in 1 m s^{-1} bins. The 6 mb simulation has a mean zonal wind speed of 0.3 m s^{-1} and a standard deviation of zonal wind speeds of $\pm$ 6 m s^{-1}, while the 1200 mb simulation has a mean zonal wind speed of 0.4 m s^{-1} and a standard deviation of zonal wind speeds of $\pm$ 4 m s^{-1}.

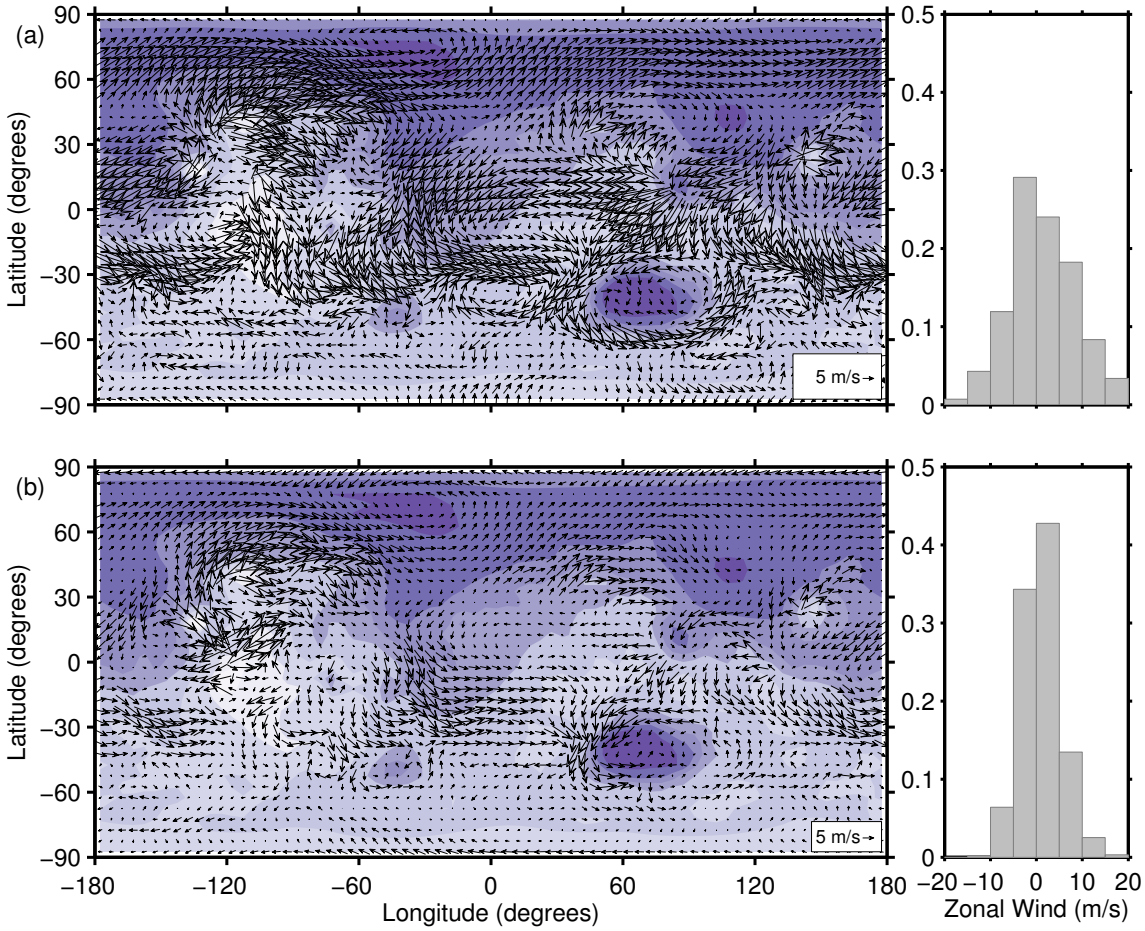

Figure 2.9: A map of surface winds and a histogram of the zonal wind speeds for (a) the 6 mb simulation and (b) the 1200 mb simulation. These results are for northern winter ($L_s = 255$ to $L_s = 315$). The vectors represent the resulting wind field due to the zonal and meridional winds. High elevation topography is shown as light purple contours and low elevation topography is shown as dark purple. The histogram shows the distribution of zonal wind speeds in 1 m s^{-1} bins. The 6 mb simulation has a mean zonal wind speed of 1.5 m s^{-1} and a standard deviation of zonal wind speeds of $\pm$ 7 m s^{-1}, while the 1200 mb simulation has a mean zonal wind speed of 1.2 m s^{-1} and a standard deviation of zonal wind speeds of $\pm$ 4 m s^{-1}.

and is consistent with the surface wind maps in Figures 2.6 through 2.9. At increased atmospheric thicknesses, the wind patterns are similar, but weaker.

2.3.3 Vertical structure of the circulation

The contours of the streamfunction, i.e., the streamlines, are snapshots of the path of the circulation. The streamlines for the 6 mb and 1200 mb simulations are shown in Figures 2.10 and 2.11, respectively. These pressures are chosen as representative of thin and thick atmospheres, respectively. For each simulation, we show the annual mean streamlines as well as the seasonal mean streamlines. The streamlines are calculated from the streamfunction, ψ, which is defined as $\vec{v} = \nabla \times \vec{\psi}$ where $\vec{v} = (0, v, w)$, $\vec{\psi} = (\psi, 0, 0)$, and v and w are the meridional and vertical velocity, respectively (*Peixoto and Oort*, 1992). Solving for ψ and converting to sigma coordinates, the streamfunction for our use is

$$\psi = 2\pi R \cos\phi \frac{(P_s - P_t)}{g} \int_0^\sigma \left[\overline{v}\right] \mathrm{d}\sigma' \tag{2.2}$$

where R is the planetary radius, ϕ is latitude, P_s is surface pressure, P_t is the pressure at the top of the atmosphere, and g is gravity (*Peixoto and Oort*, 1992).[3]

The annual mean streamlines for the 6 mb simulation, in Figure 2.10(a), indicate that the dominant circulation involves upwelling in the southern tropics and downwelling in the northern tropics. This annual mean Hadley cell generates an annual mean cross-equatorial

[3]The line over the quantity, $\overline{(\cdot)}$, signifies a time mean of the data and the square brackets, $\left[\,\cdot\,\right]$, signify the zonal mean of the data. In order to properly account for the divergent mass fields that occur due to the large topographical changes on Mars, we define the Eulerian time average as $\overline{(\cdot)} = \overline{(P_s \cdot)}/\bar{P}_s$ where P_s is the surface pressure (Tapio Schneider, 2011, pers. comm.). Similarly, we define the Eulerian zonal average as $\left[\,\cdot\,\right] = \left[P_s \cdot\right]/\left[P_s\right]$.

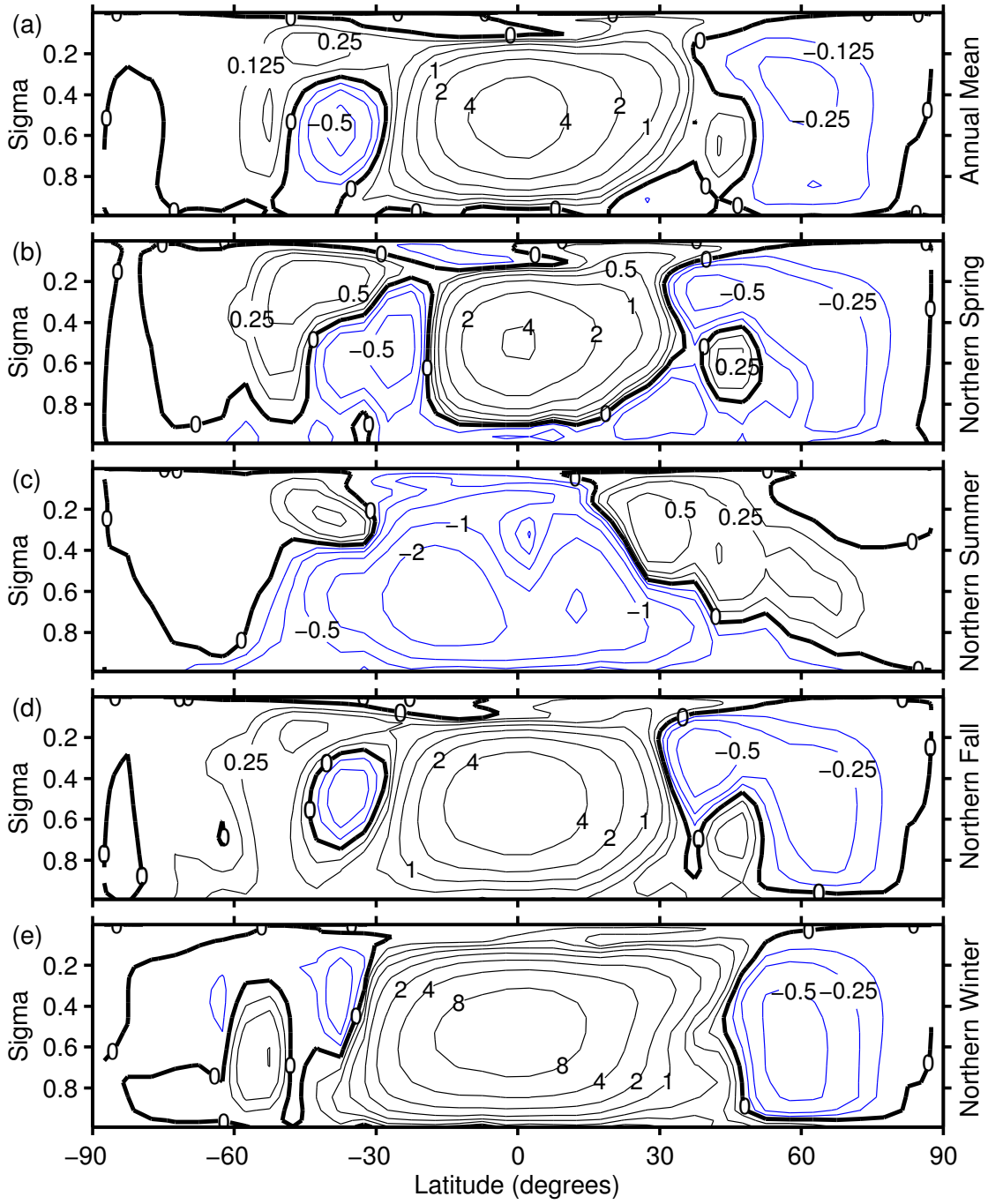

Figure 2.10: Annual and seasonal mean streamlines, in units of 10^9 kg/s, for the 6 mb atmosphere at 25° obliquity. Positive contours (black lines) correspond to clockwise rotation and use a geometric progression (0.125, 0.25, 0.5, 1, 2, 4, ...) for level spacings, while negative contours (blue lines) correspond to counter-clockwise rotation and also use a geometric progression (-0.125, -0.25, -0.5, -1, -2, -4, ...) for level spacings. The bolded solid black line is the zero streamline contour.

flow from the north to the south near the surface and an opposing south to north cross-equatorial flow in the upper altitudes. This general structure is seen in the northern spring, northern fall, and northern winter plots (Figures 2.10(b), 2.10(d), and 2.10(e)). In the northern spring, the convergence of the Hadley cells occurs in the southern tropics near the equator. The southern Hadley cell then pushes northward during the northern summer such that the zonal mean circulation is dominated by a cross-equatorial cell that rises in the northern midlatitudes and sinks in the southern midlatitudes (Figure 2.10(c)). This circulation is reversed in the northern fall and northern winter, where the cross-equatorial cell rises in the southern tropics and sinks in the northern tropics (Figures 2.10(d) and 2.10(e)).

The structure seen in the 1200 mb simulation, Figure 2.11, is representative of the vertical structure of the circulation in all of the thicker atmosphere simulations. Along with stronger circulations compared to the 6 mb simulation, the streamlines in the 1200 mb simulation exhibit greater complexity. The northern spring and northern fall circulations, Figures 2.11(b) and 2.11(d), do not have the traditional equinoctial structure expected of Hadley circulation (see *Held and Hou* (1980) and *Peixoto and Oort* (1992) for examples). Instead, the northern spring circulation has a cross-equatorial cell that rises in the southern tropics and sinks in the northern tropics, while flanked by two opposing cells of approximately equal strength. The northern fall also has a cross-equatorial cell with a similar flow pattern. While also flanked by two opposing cells in each midlatitude region, the northern midlatitude cell is confined to a smaller latitudinal region by a relatively strong extratropical, polar cell that rises in the midlatitudes and sinks in the polar regions. The solstitial circulations, however, largely exhibit the expected cross-equatorial circulation that

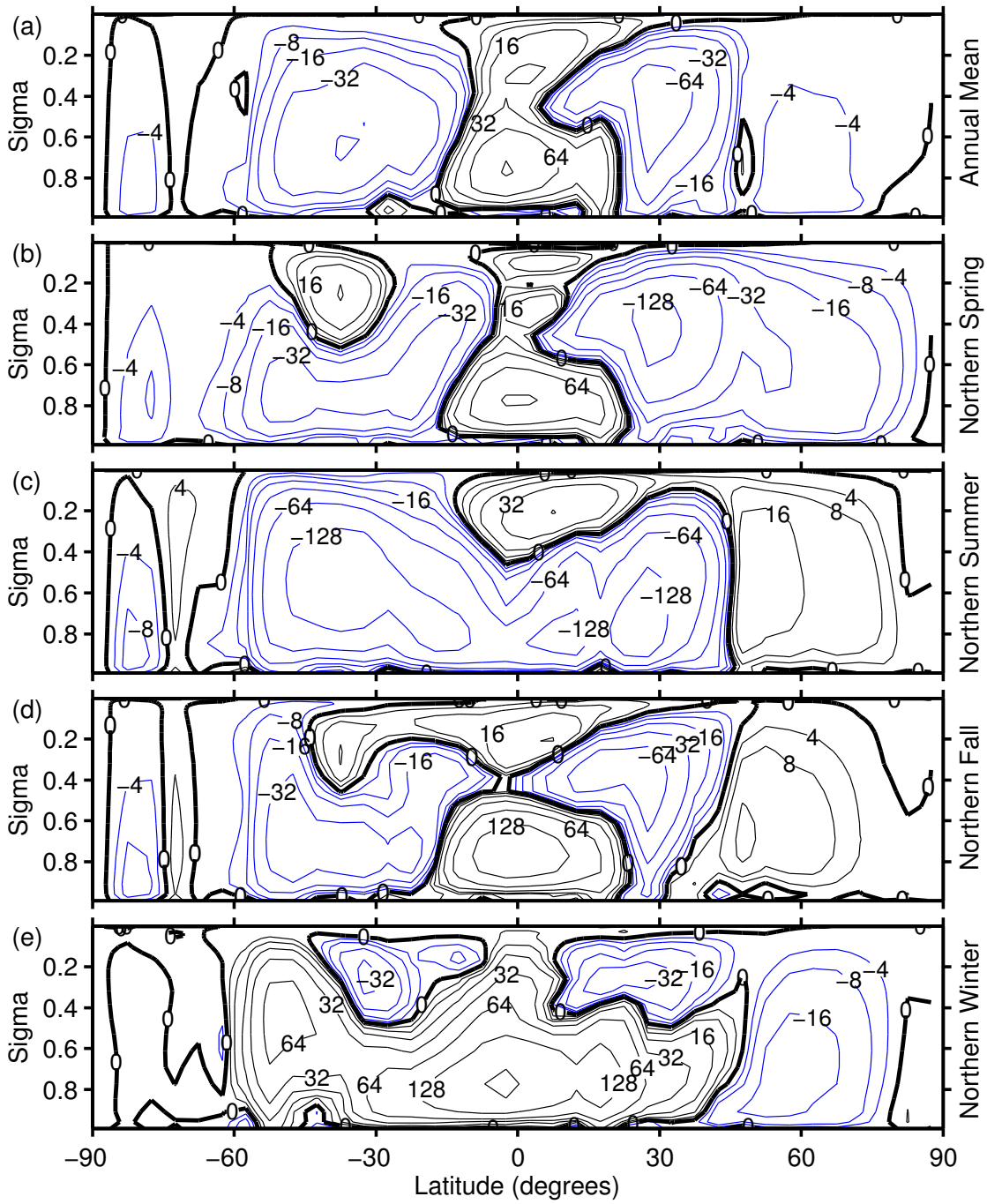

Figure 2.11: Annual and seasonal mean streamlines, in units of 10^9 kg/s, for the 1200 mb atmosphere at 25° obliquity. Positive contours (black lines) correspond to clockwise rotation and use a geometric progression (4, 8, 16, 32, 64, 128, 256, 512, ...) for level spacings, while negative contours (blue lines) correspond to counter-clockwise rotation and also use a geometric progression (-4, -8, -16, -32, -64, -128, -256, -512, ...) for level spacings. The bolded solid black line is the zero streamline contour.

extends deep into the winter hemisphere midlatitudes (*Lindzen and Hou*, 1988; *Caballero et al.*, 2008). Both the northern summer and northern winter circulations (Figures 2.11(c) and 2.11(e)) extend from -60° S to 45° N and provide the strongest circulation during the Martian year.

2.3.4 Meridional transport of energy

We investigated how the meridional transport of energy changes with global mean atmospheric pressure. Specifically, we calculated the seasonal and zonal mean of the dry static energy, which is defined as

$$E = gz + c_p T \tag{2.3}$$

where g is gravity, z is height, c_p is the specific heat capacity, and T is the air temperature. Essentially, the dry static energy consists of the atmospheric potential energy, gz, and the atmospheric internal energy, $c_p T$ (*Peixoto and Oort*, 1992). Thus, the dry static energy captures the adiabatic and diabatic heating in the atmosphere.

In order to understand the meridional transport of the dry static energy, represented by vE where v is the meridional wind velocity, we used Reynolds decomposition to identify the mean circulation, stationary eddy, and transient eddy terms of the meridional transport (*Peixoto and Oort*, 1992). Generally, a diagnostic field can be decomposed into a mean field and a perturbation field. A quantity is related to the time mean and time perturbation by $(\cdot) = \bar{(\cdot)} + (\cdot)'$, where $\bar{(\cdot)}$ is the mean of the quantity $(\cdot)$ and $(\cdot)'$ is the perturbation. Similarly, a quantity is related to the zonal mean and zonal perturbation by $(\cdot) = [\bar{\cdot}] + (\cdot)^*$, where $[\bar{\cdot}]$ is the mean of the quantity $(\cdot)$ and $(\cdot)^*$ is the perturbation. The decomposition of

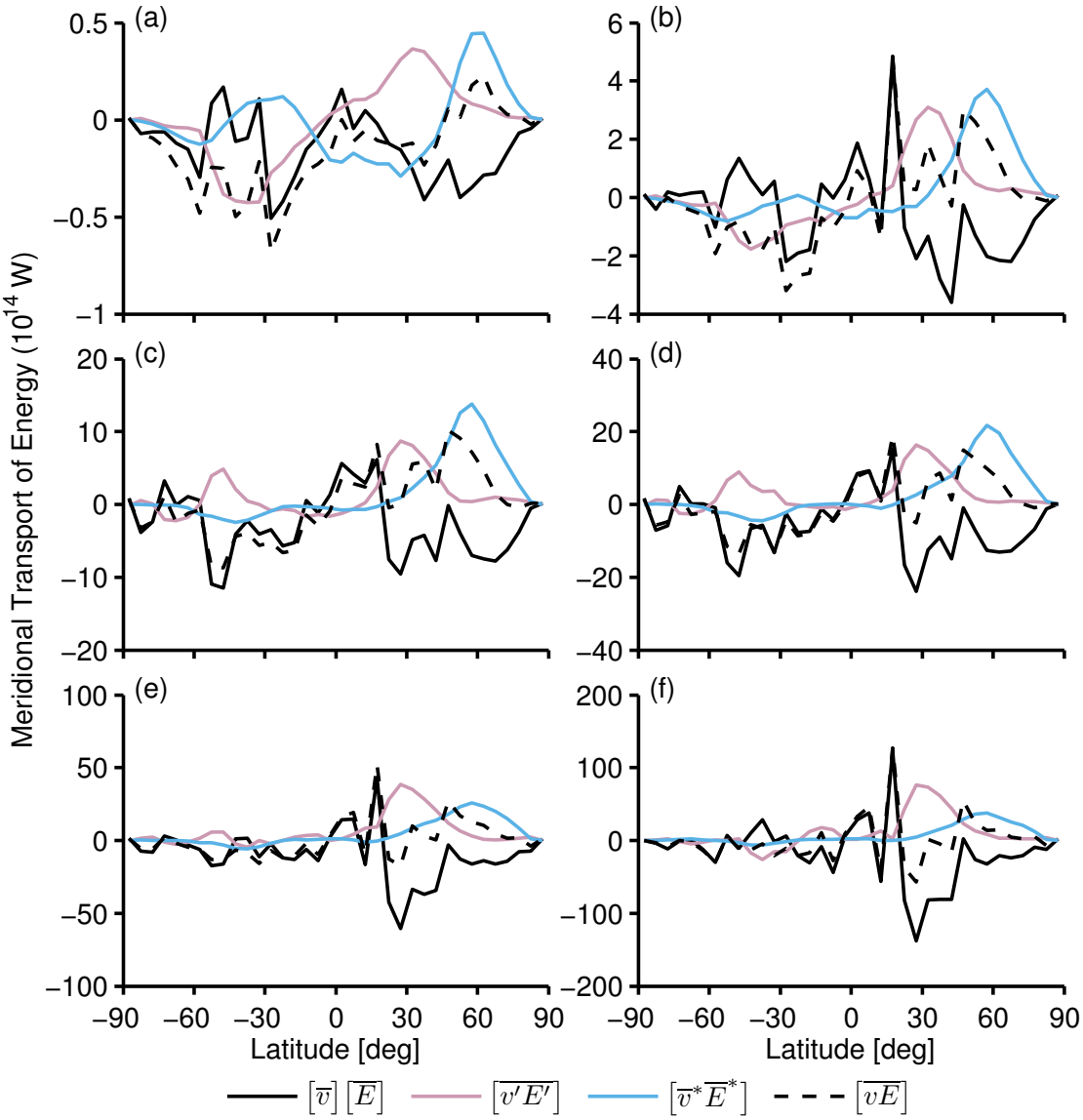

Figure 2.12: The meridional transport of dry static energy for $L_s = 345$ to $L_s = 45$ (northern spring) as a function of mean surface pressure. The figure shows mean surface pressures of (a) 6 mb, (b) 60 mb, (c) 300 mb, (d) 600 mb, and (f) 1200 mb. The solid black line is the mean circulation, $\left[\overline{v}\right]\left[\overline{E}\right]$, the light red line is the transient eddies, $\left[\overline{v'E'}\right]$, the blue line is the stationary eddies, $\left[\overline{v}^*\overline{E}^*\right]$, and the dashed black line is the total circulation, $\left[\overline{vE}\right]$.

the zonal and temporal mean of the total transport, $\left[\overline{vE}\right]$, is

$$\left[\overline{vE}\right] = \left[\overline{v}\right]\left[\overline{E}\right] + \left[\overline{v}^{*}\overline{E}^{*}\right] + \left[\overline{v'E'}\right] \tag{2.4}$$

where $\left[\overline{v}\right]\left[\overline{E}\right]$ is the mean circulation term, $\left[\overline{v}^{*}\overline{E}^{*}\right]$ is the stationary term, and $\left[\overline{v'E'}\right]$ is the transient term (*Peixoto and Oort*, 1992). With this decomposition we can determine whether a particular atmospheric phenomena is controlled by larger scale circulation as shown by the mean circulation term, $\left[\overline{v}\right]\left[\overline{E}\right]$, or by storm activity as shown by the stationary and eddy terms, $\left[\overline{v}^{*}\overline{E}^{*}\right]$ and $\left[\overline{v'E'}\right]$.

The northern spring meridional transport has strong stationary and transient eddies in the northern hemisphere at all atmospheric thicknesses. As seen in Figure 2.12, the northern transient eddy transport peaks at around 25° N to 30° N while the northern stationary eddy transport peaks at round 60° N. Both of these eddy transports are moving dry static energy northward. This northward flux of energy in the atmosphere is partially countered by a predominantly southward mean meridional transport in the northern hemisphere. The net result for all of the atmospheric thicknesses is northward transport in the extratropics.

In the thicker atmosphere simulations, the southern hemisphere transport becomes much smaller than the northern atmosphere transport. For the 1200 mb and 3000 mb simulations (Figures 2.12(e) and 2.12(f)), the southern hemisphere transport is over an order of magnitude weaker than the northern hemisphere transport. Additionally, the southern hemisphere transport shows no clear pattern in terms of mean nor eddy transport.

The northern summer meridional transport, show in Figure 2.13, has predominantly southward transport of energy. In the 6 mb simulation (Figure 2.13(a)), the transport is

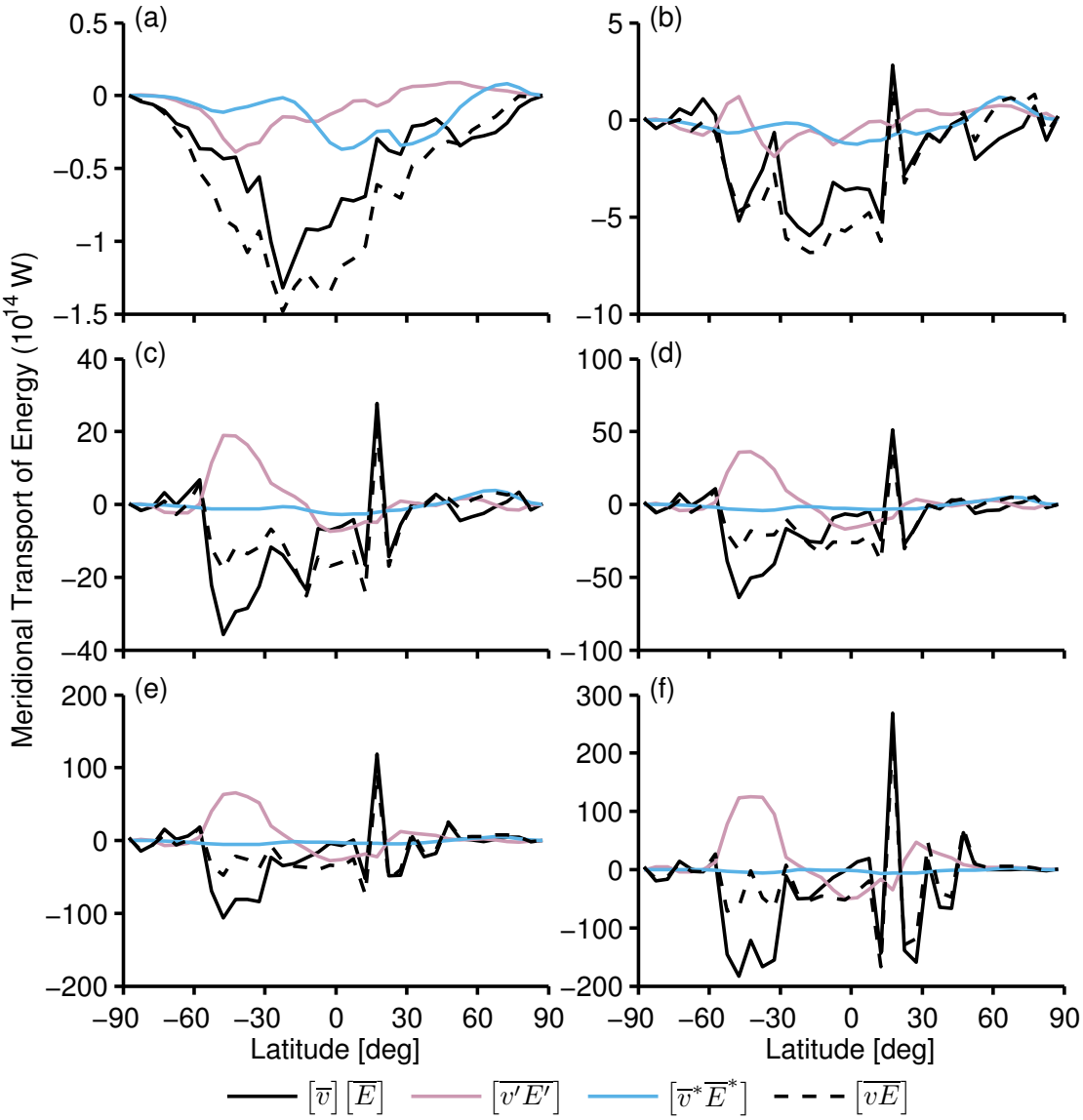

Figure 2.13: The meridional transport of dry static energy for $L_s = 75$ to $L_s = 135$ (northern summer) as a function of mean surface pressure. The figure shows mean surface pressures of (a) 6 mb, (b) 60 mb, (c) 300 mb, (d) 600 mb, and (f) 1200 mb. The solid black line is the mean circulation, $\left[\overline{v}\right]\left[\overline{E}\right]$, the light red line is the transient eddies, $\left[\overline{v'E'}\right]$, the blue line is the stationary eddies, $\left[\overline{v}^*\overline{E}^*\right]$, and the dashed black line is the total circulation, $\left[\overline{vE}\right]$.

dominated by a mean southward transport that exists pole-to-pole with a peak at $\sim 30^\circ$ S. Stationary eddies in the northern hemisphere contribute to this southward energy transport whereas southern hemisphere transient eddies continue the southward transport. For the 60 mb simulation, shown in Figure 2.13(b), the mean circulation continues to dominate the transport but some sharp interruptions in the southward transport begin to appear. At $\sim 20^\circ$ N there is a sharp spike of northward energy transport. This spike of northward transport appears in all of the thicker atmosphere simulations (60 mb to 3000 mb). At the thicker atmospheres the stationary eddies are almost completely negligible. The transient eddies are similarly swamped except in the southern midlatitudes where a large peak in the transient eddy transport appears. In the 300 mb, 600 mb, 1200 mb, and 3000 mb simulations the bulk of the southward energy transport is confined to latitudes between 30° S and 60° S. Overall, during the northern summer the thicker atmospheres have stronger mean circulations that dominate transport that is more narrowly confined than in the 6 mb simulation.

The northern fall meridional transport, shown in Figure 2.14, reverses the direction of transport from the previous season and begins to transport energy northward. These northern fall simulations show the same dominance of the mean circulation as the other seasons. In the 6 mb simulation, the total transport is northward, pole-to-pole, and primarily carried by the mean circulation. At high mean surface pressures, the transport regions are much stronger but latitudinally narrower. The largest northward transport is confined to the equatorial regions. The sharp spike in northward mean circulation transport that was seen in the northern summer diagnostics, in Figures 2.13(b) through 2.13(f), appears

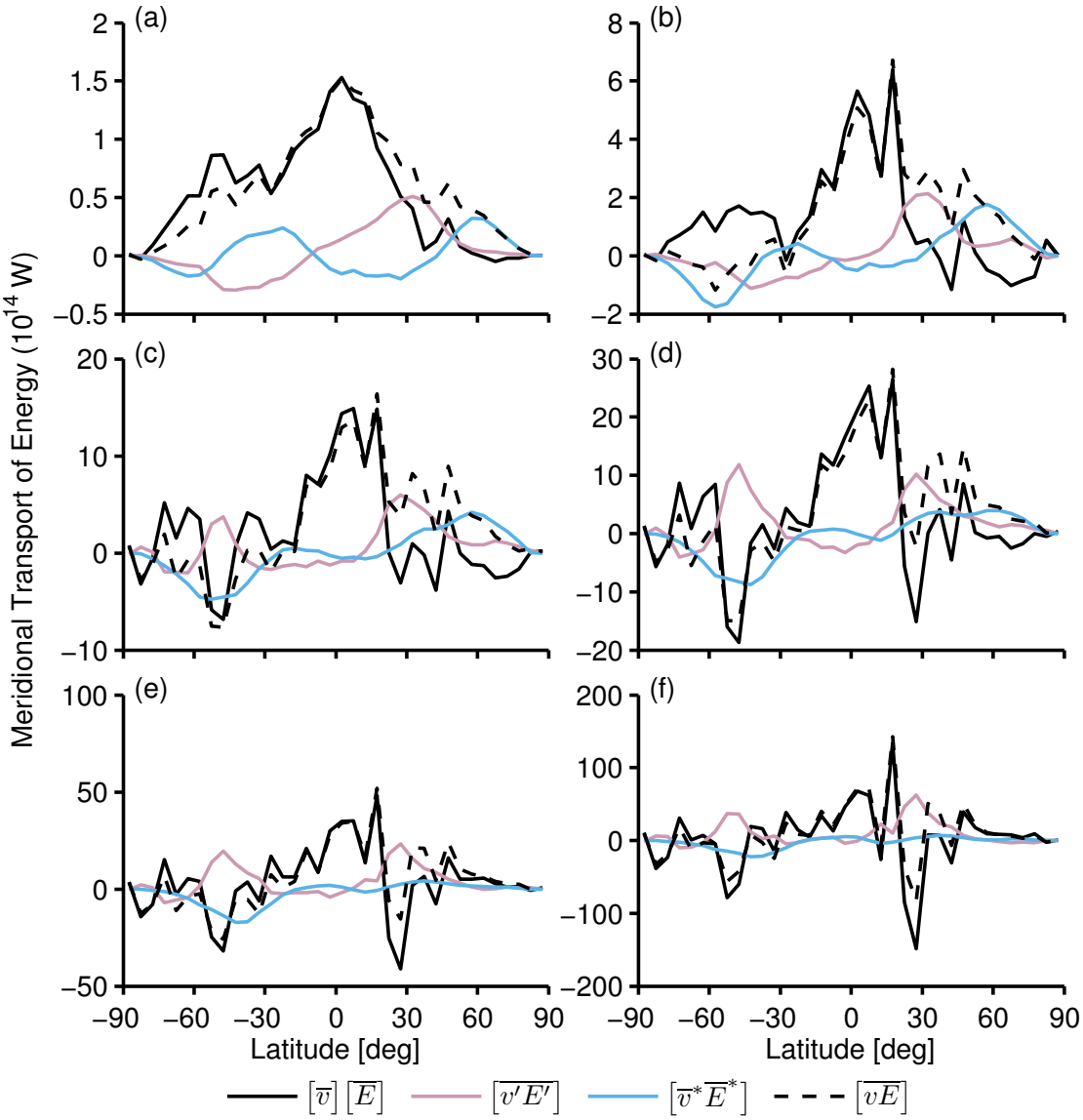

Figure 2.14: The meridional transport of dry static energy for $L_s = 165$ to $L_s = 225$ (northern fall) as a function of mean surface pressure. The figure shows mean surface pressures of (a) 6 mb, (b) 60 mb, (c) 300 mb, (d) 600 mb, and (f) 1200 mb. The solid black line is the mean circulation, $\left[\overline{v}\right]\left[\overline{E}\right]$, the light red line is the transient eddies, $\left[\overline{v'E'}\right]$, the blue line is the stationary eddies, $\left[\overline{v}^*\overline{E}^*\right]$, and the dashed black line is the total circulation, $\left[\overline{vE}\right]$.

in the thicker atmosphere simulations during the northern fall, as seen in Figures 2.14(b) through 2.14(f). This time, however, the northward spike at $\sim 20^\circ$ N of the mean circulation is accompanied by a southward spike in mean circulation energy transport at $\sim 30^\circ$ N for the 300 mb and thicker atmospheres. In the southern hemisphere for 300 mb and thicker atmosphere simulations, there is a total southward transport of energy between 30° S and 60° S which is driven by the mean circulation and only marginally balanced by transient eddies that transport the dry static energy northward.

Finally, for the northern winter, the dry static energy is transported northward across the tropics in all of the simulations, as seen in Figures 2.15(a) to 2.15(f). In the 6 mb simulations, Figure 2.15(a), there is no net transport of energy in the southern extratropics and southern polar regions, but starting around $\sim 45^\circ$ S and continuing to the north pole there is northward transport of the dry static energy, with a peak just north of the equator. This transport is primarily carried by the mean circulation throughout both the northern and southern tropics, but it is the stationary eddies that continue the northward transport in the northern extratropics and polar regions. This general pattern is continued in the 60 mb, 300 mb, and 600 mb simulations (Figures 2.15(b), 2.15(c), and 2.15(d), respectively). The two primary changes compared to the 6 mb simulation are: first, a spike in northward transport by the mean circulation at $\sim 20^\circ$ N, and second, an opposing pair of spikes in the mean circulation in the southern hemisphere between $\sim 50^\circ$ S and $\sim 60^\circ$ S. The spike in mean circulation at $\sim 20^\circ$ is similar to the one seen in all of the other seasons and is persistent in all of the thicker atmosphere simulations. This particular spike in northward transport by the mean circulation grows in strength as a function of increasing mean atmospheric

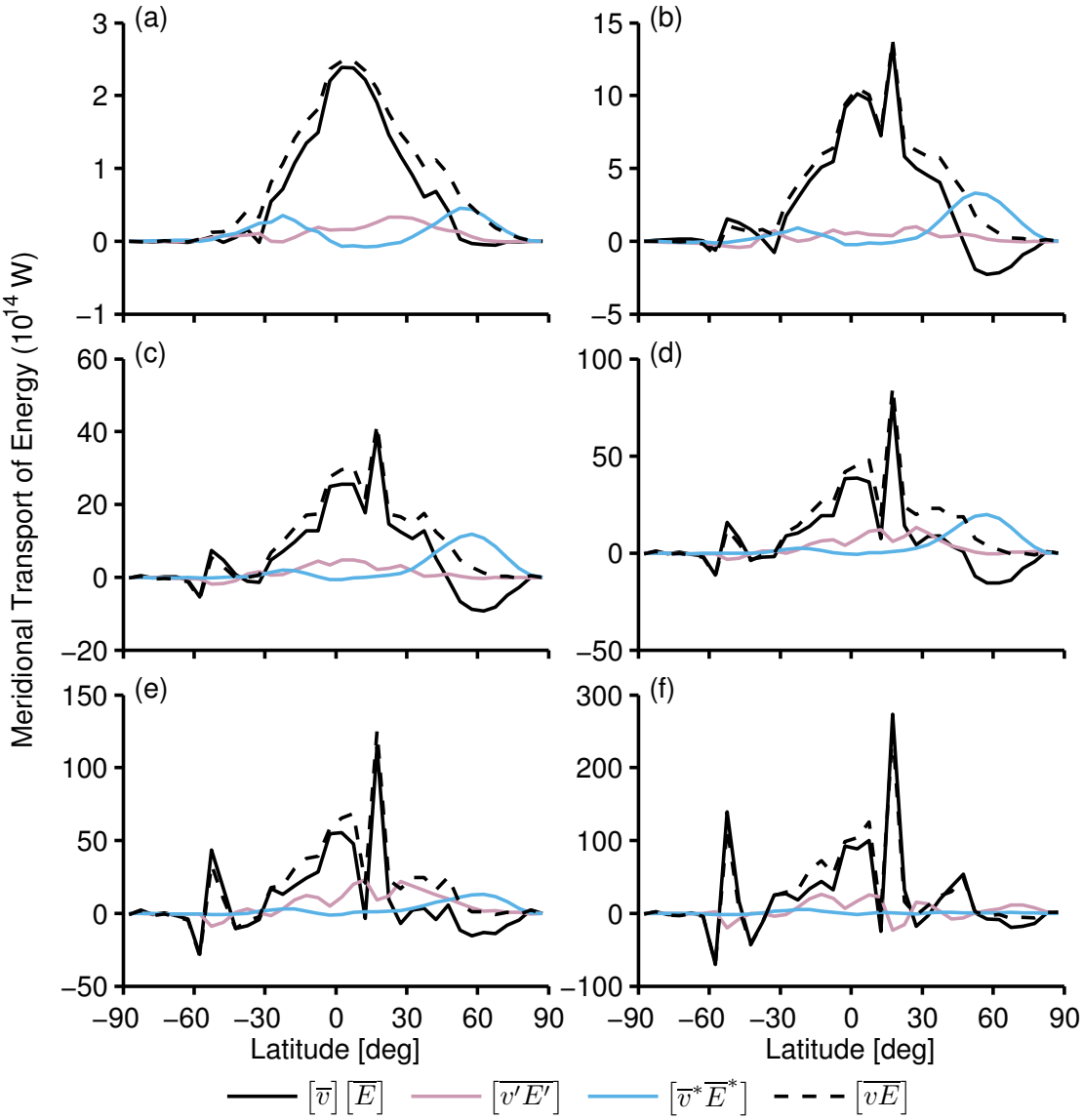

Figure 2.15: The meridional transport of dry static energy for $L_s = 255$ to $L_s = 315$ (northern winter) as a function of mean surface pressure. The figure shows mean surface pressures of (a) 6 mb, (b) 60 mb, (c) 300 mb, (d) 600 mb, and (f) 1200 mb. The solid black line is the mean circulation, $\left[\overline{v}\right]\left[\overline{E}\right]$, the light red line is the transient eddies, $\left[\overline{v'E'}\right]$, the blue line is the stationary eddies, $\left[\overline{v}^*\overline{E}^*\right]$, and the dashed black line is the total circulation, $\left[\overline{vE}\right]$.

pressure such that by 3000 mb the strength of the transport spike overwhelms the rest of the mean circulation transport. Similarly, the pair of spikes in the southern hemisphere grow in strength with increasing mean surface pressure and consists of southward transport by the mean circulation at $\sim 60^\circ$ S and northward transport by the mean circulation at $\sim 50^\circ$ S.

2.3.5 Condensational flow

As the atmosphere deposits CO_2 ice in the winter polar regions, the total mass of atmospheric CO_2 changes, which also changes the magnitude and distribution of the atmospheric surface pressure (*Tillman et al.*, 1993; *Hess et al.*, 1979). The atmosphere adjusts to these changes by shifting atmospheric mass into the winter polar region. Whereas the mass-weighted column average meridional velocity of a conserved atmospheric flow is zero, the meridional flow of atmospheric CO_2 due to polar CO_2 condensation is non-conserving and generates a non-zero mass-weighted column average meridional velocity (*Pollack et al.*, 1981, 1990). This condensation flow is calculated by taking the mass-weighted vertical average

$$\left\langle \left[\overline{v}_c\right] \right\rangle = \int_1^0 \left[\overline{(P_s - P_t)v}\right] \mathrm{d}\sigma \Big/ \left[\overline{P_s - P_t}\right] \tag{2.5}$$

where v is the total meridional velocity at each vertical level, σ is the vertical coordinate, $(P_s - P_t)/g$ is the column mass, with g being the Martian gravitational acceleration that subsequently cancels out of Equation (2.5), and $< \cdot >$ indicates a vertical mean (*Pollack et al.*, 1981). The condensation flow velocity, while a function of latitude, is a constant value at every vertical level, thus at each value of σ the condensation flow is defined as

$\left[\overline{v}_c\right] = \left\langle \left[\overline{v}_c\right] \right\rangle$. With this condensation flow velocity, $\left[\overline{v}_c\right]$, we decomposed the mean meridional velocity at each vertical level into

$$\left[\overline{v}\right] = \left[\overline{v}_o\right] + \left[\overline{v}_c\right] \tag{2.6}$$

where $\left[\overline{v}_c\right]$ is the condensation flow velocity and $\left[\overline{v}_o\right]$ is the velocity of the overturning cells, which is calculated by $\left[\overline{v}_o\right] = \left[\overline{v}\right] - \left[\overline{v}_c\right]$. The decomposition of the mean meridional wind into an overturning flow velocity and a condensation flow velocity allows us to determine how condensation of atmospheric CO_2 affects the mean meridional circulation.

Figures 2.16 through 2.19 show the mean meridional wind decomposed into a condensation flow and an overturning flow. In all of the simulations and all of the seasons, the condensation flow creates the high variability in energy transport seen in the total mean circulation. Wherever temperatures drop low enough for atmospheric CO_2 to condense, the atmosphere transports mass and energy to account for the change in column CO_2 mass. In Figures 2.16 through 2.19, the green line represents the transport of dry static energy by the condensation flow in the atmosphere. For all seasons and all atmospheric mean surface pressures, the Martian topography affects the condensation flow transport and thus the total mean transport of dry static energy. The effect is the smallest in the 6 mb simulations. During northern spring and summer, Figures 2.16(a) and 2.17(a), the condensation flow transports dry static energy southward at almost all latitudes. This condensation flow corresponds to the cold south polar temperatures that begin to develop in northern spring and reach a peak during northern summer, which counters the overturning flow during the spring but augments the overturning flow during the summer. During northern spring, the

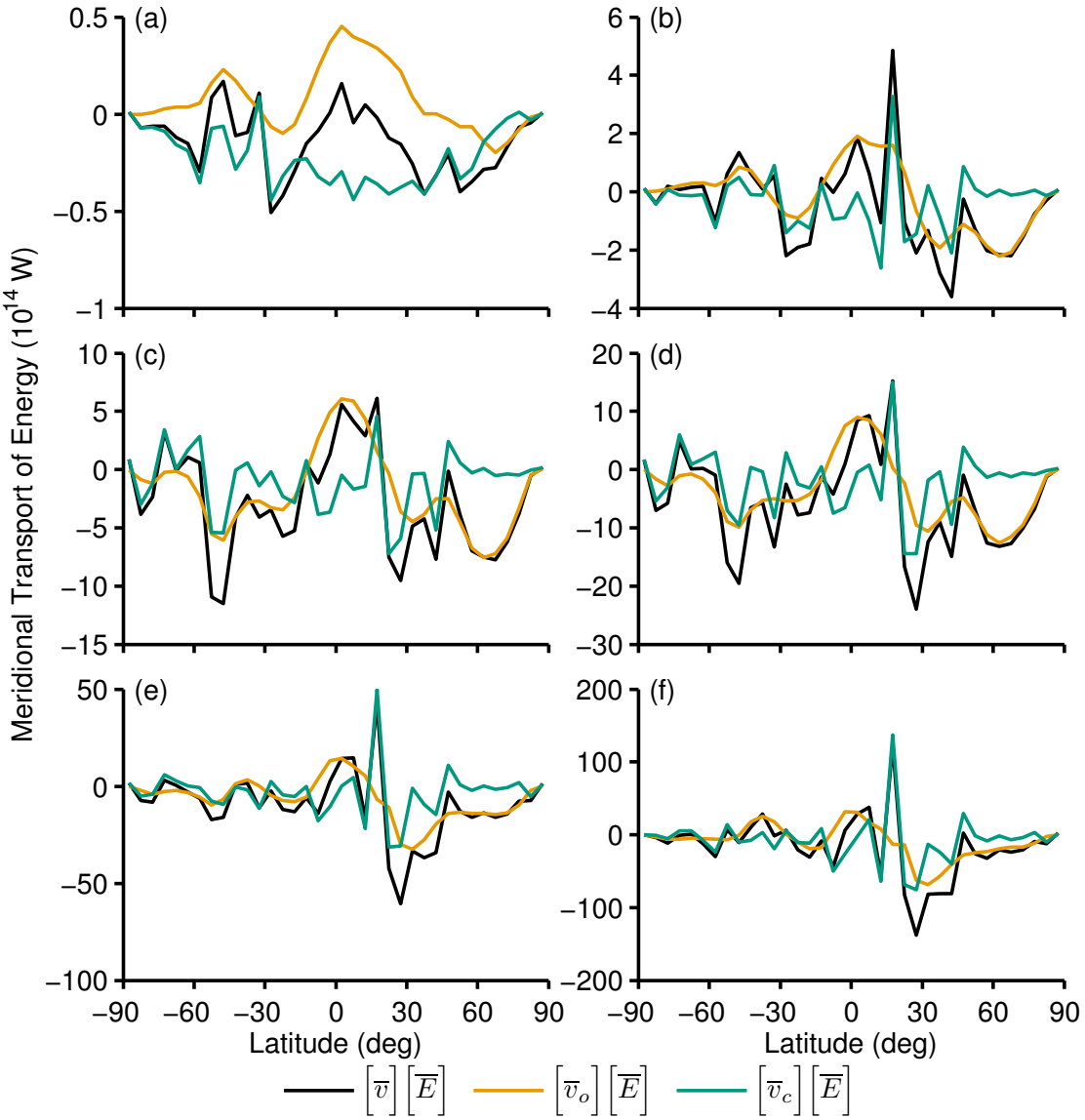

Figure 2.16: The mean meridional transport of dry static energy for $L_s = 345$ to $L_s = 45$ (northern spring) as a function of mean surface pressure. The mean transport is decomposed into the transport due to overturning cells and the transport due to condensation flow. The plots include the following initial surface pressures: (a) 6 mb, (b) 60 mb, (c) 300 mb, (d) 600 mb, (e) 1200 mb, and (f) 3000 mb. The solid black line is the total mean circulation, $\left[\overline{v}\right]\left[\overline{E}\right]$, the orange line is the overturning circulation, $\left[\overline{v}_o\right]\left[\overline{E}\right]$, and the green line is the condensation flow, $\left[\overline{v}_c\right]\left[\overline{E}\right]$.

6 mb simulation shows a reversal of the condensation flow between 30° S and 50° S which is associated with the Hellas and Argyre Basins. During northern summer, the transport by condensation flow dominates the transport outside of the tropics. Without the condensation flow, the southward flow of the overturning transport, $\left[\overline{v}_o\right]\left[\overline{E}\right]$, is limited to the tropics. The condensation flow expands the mean transport into the extratropics in both hemispheres. This expansion of the zone of transport occurs during the northern fall as well, although in the northward direction. At higher atmospheric pressures, the condensation flow overwhelms the overturning flow leading to a mean transport, $\left[\overline{v}\right]\left[\overline{E}\right]$, that has rapid changes in transport magnitude and direction as a function of latitude but shows little correlation with the streamlines seen in Figures 2.10 and 2.11.

The overturning circulation transport, represented by the orange line in the figures, represents the energy transport due to the traditional large-scale circulation, e.g., the thermally direct Hadley cell circulation or the thermally indirect Ferrell cell circulation. The northern spring overturning transport for the 1200 mb simulation, shown in Figure 2.16(e), has northward transport of dry static energy in the southern and northern tropics, especially close to the equator. This northward transport corresponds to the equatorially centered overturning cell seen in Figure 2.11(b). Figure 2.11(b) also shows a strong overturning cell that begins in the northern tropics and stretches to the northern polar region. This overturning cell results in net southward transport of dry static energy, which is clearly seen in the mean overturning transport shown in Figure 2.16(e). We see a similar pattern in the other seasons. During northern summer (Figure 2.17(e)), the overturning transport drives dry static energy into the midlatitudes of the winter hemisphere, consistent with the exten-

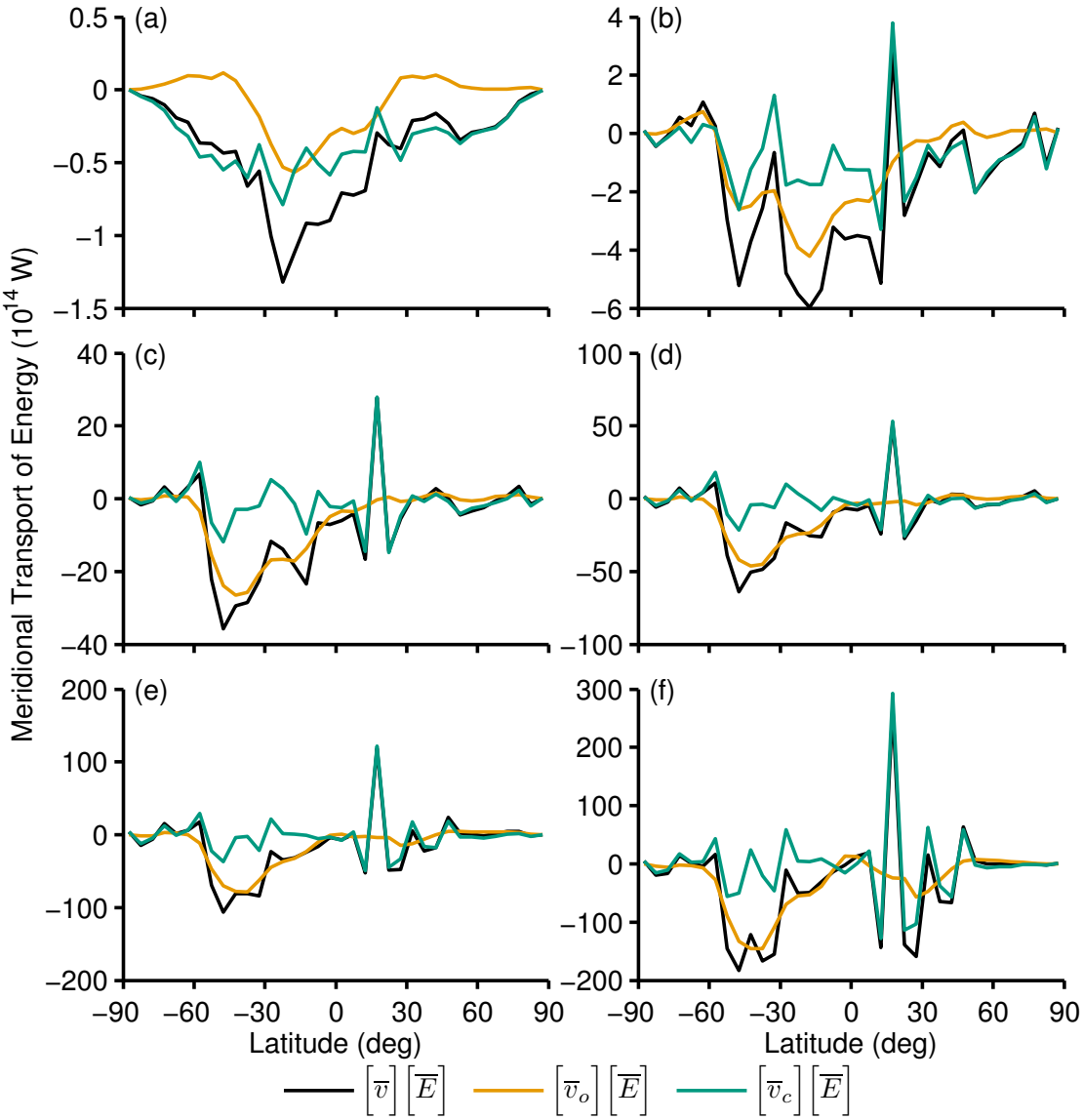

Figure 2.17: The mean meridional transport of dry static energy for $L_s = 75$ to $L_s = 135$ (northern summer) as a function of mean surface pressure. The mean transport is decomposed into the transport due to overturning cells and the transport due to condensation flow. The plots include the following initial surface pressures: (a) 6 mb, (b) 60 mb, (c) 300 mb, (d) 600 mb, (e) 1200 mb, and (f) 3000 mb. The solid black line is the total mean circulation, $\left[\overline{v}\right]\left[\overline{E}\right]$, the orange line is the mean meridional circulation, $\left[\overline{v}_o\right]\left[\overline{E}\right]$, and the green line is the condensation flow, $\left[\overline{v}_c\right]\left[\overline{E}\right]$.

sive cross-equatorial cell seen in Figure 2.11(c). The northern fall overturning transport, shown in Figure 2.18(e), shows that the transport has changed direction with the equatorial tropics dominated by northward transport due to a strong overturning cell centered on the equator (Figure 2.11(d)). Figure 2.18(e) also shows that both the northern and southern midlatitudes transport dry static energy southward, which corresponds to the opposing midlatitude overturning circulations that flank the equatorial circulation during northern fall, as seen in Figure 2.11(d). Finally, the northern winter analysis also shows the connection between the streamlines and the overturning circulation transport. Figure 2.19(e) shows overturning transport that moves dry static energy from the summer southern hemisphere northward into the winter northern hemisphere. This transport is accomplished by the large cross-equatorial cell seen in Figure 2.11(e).

As shown, the condensation of CO_2 has a significant impact on the meridional circulation. Even small amounts of CO_2 condensation generate a condensation flow that then affects the meridional transport of energy. Therefore, though the plot of zonal mean CO_2 ice in the 60 mb simulation shows no CO_2 ice accumulation above 1 cm depth at Olympus Mons (Figure 2.1(b)), there is a spike in the condensation flow transport at the same latitude. At 60 mb, Olympus Mons is only transiently at condensation temperature, but the CO_2 ice that condenses and sublimates transiently throughout the year is sufficient to drive a condensation flow that then affects the mean circulation transport, as seen in all seasons in Figures 2.16(b) through 2.19(b). This phenomena exists in the thicker atmospheres, where the CO_2 ice deposition on Olympus Mons is greater, and even dominates the global deposition above 1000 mb. As well, the thicker atmospheres have condensation

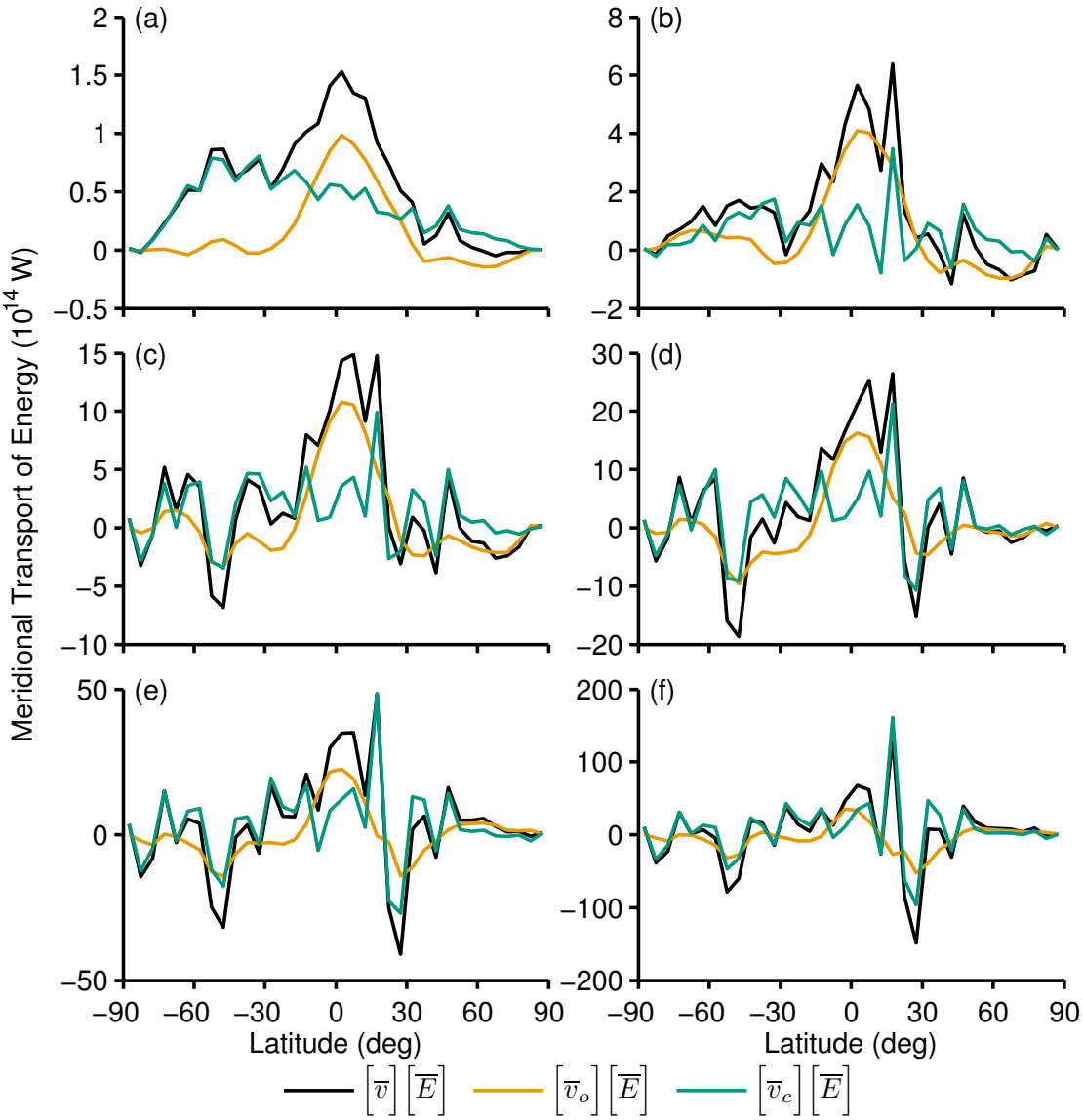

Figure 2.18: The mean meridional transport of dry static energy for $L_s = 165$ to $L_s = 225$ (northern fall) as a function of mean surface pressure. The mean transport is decomposed into the transport due to overturning cells and the transport due to condensation flow. The plots include the following initial surface pressures: (a) 6 mb, (b) 60 mb, (c) 300 mb, (d) 600 mb, (e) 1200 mb, and (f) 3000 mb. The solid black line is the total mean circulation, $\left[\overline{v}\right]\left[\overline{E}\right]$, the orange line is the mean meridional circulation, $\left[\overline{v}_o\right]\left[\overline{E}\right]$, and the green line is the condensation flow, $\left[\overline{v}_c\right]\left[\overline{E}\right]$.

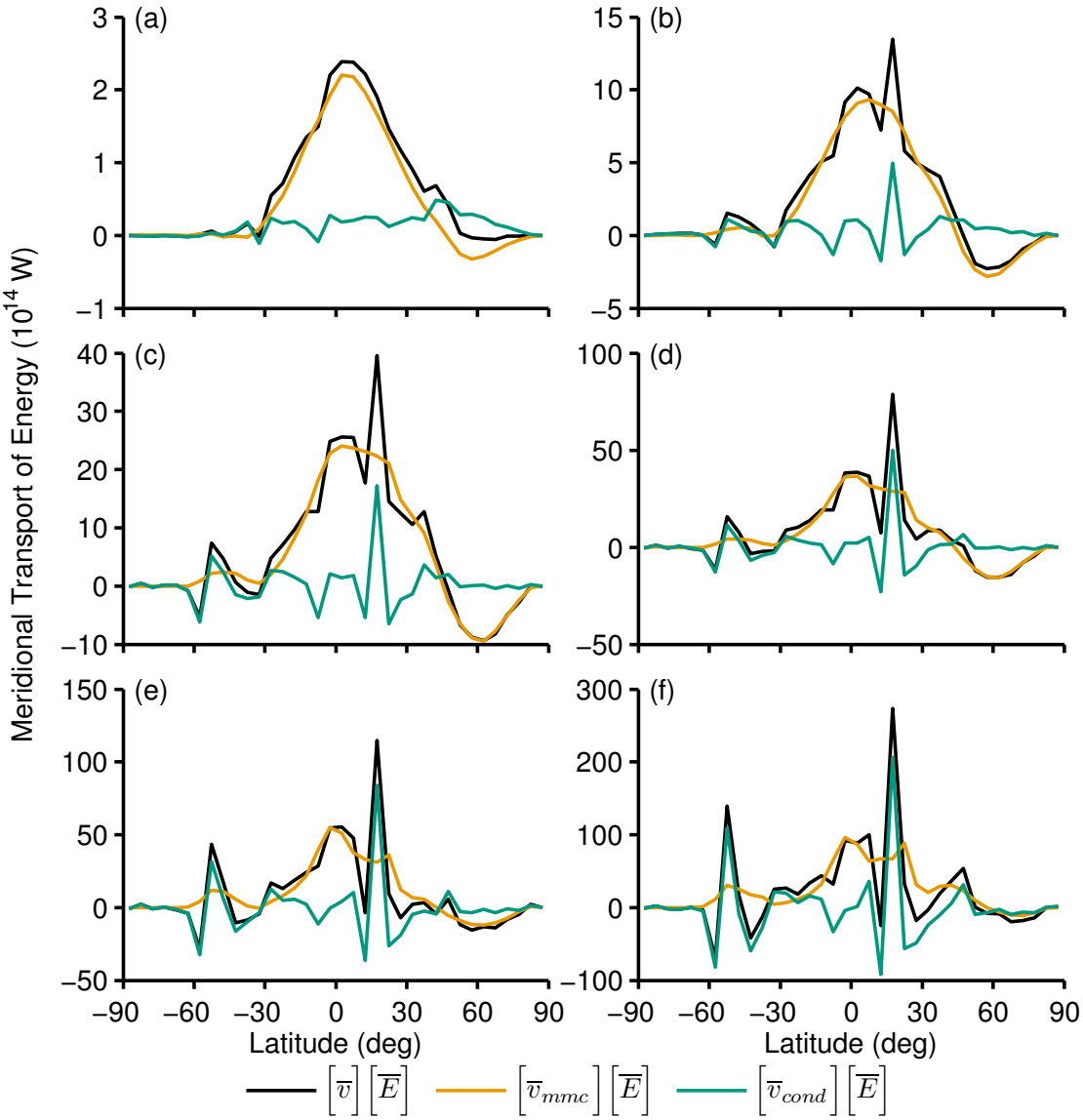

Figure 2.19: The mean meridional transport of dry static energy for $L_s = 255$ to $L_s = 315$ (northern winter) as a function of mean surface pressure. The mean transport is decomposed into the transport due to overturning cells and the transport due to condensation flow. The plots include the following initial surface pressures: (a) 6 mb, (b) 60 mb, (c) 300 mb, (d) 600 mb, (e) 1200 mb, and (f) 3000 mb. The solid black line is the total mean circulation, $\left[\overline{v}\right]\left[\overline{E}\right]$, the orange line is the mean meridional circulation, $\left[\overline{v}_o\right]\left[\overline{E}\right]$, and the green line is the condensation flow, $\left[\overline{v}_c\right]\left[\overline{E}\right]$.

flows associated with other mountain highs on the Martian surface. The combination of these elevation driven CO_2 condensation regions results in the highly variable mean circulation, including the anomalous transport spikes, seen in the meridional transport analysis shown in Figures 2.12 to 2.15.

2.4 Results from the faint young sun simulations

The luminosity of the Sun has slowly evolved over the history of the solar system, starting 4.7 billion years ago at 70% of current luminosity (*Gilliland*, 1989; *Gough*, 1981). Since solar luminosity is the primary force driving the climate dynamics of a terrestrial planetary atmosphere, this reduced luminosity, or "faint young Sun", may have affected the climate dynamics of ancient Mars. In order to investigate the impact of the faint young sun, we used a solar luminosity of 75% of current luminosity in some of the MarsWRF simulations. This 75% luminosity corresponds to roughly 4 billion years ago, which was the middle of the Noachian era on Mars, the primary epoch for which a thicker Martian atmosphere has been proposed. Thus, these simulations are appropriate for understanding a possible warmer Mars.

With the lower luminosity, the magnitude and extent of the condensation of CO_2 increases. As shown in Figure 2.20, all of the atmospheric thicknesses exhibit a perennial CO_2 ice cap in at least one of the geographic poles. At the higher mean atmospheric pressures, the perennial cap reaches down into the midlatitudes and thus a large portion of the Martian surface is covered by CO_2 ice. Seasonal ice continues to be deposited on top of the perennial ice, and for the 600 mb, 1200 mb, and 3000 mb simulations CO_2 ice condenses

onto the Olympus Mons region at a non-negligible rate. Unsurprisingly, at all atmospheric pressures the Martian climate under the faint young Sun is colder and icier than under current solar luminosity.

For both thin and thick atmospheres, the large-scale circulation under the faint young Sun is surprisingly similar to the current solar luminosity, despite the lower incoming insolation. The circulations in Figure 2.21, which shows the 6 mb simulation for the faint young Sun, and Figure 2.10, which shows the 6 mb simulation for the current luminosity, differ primarily in the extratropics. These extratropical circulations are usually thermally indirect and driven by midlatitude eddy activity. The differences in these circulations between Figure 2.10 and Figure 2.21 reflect the difference in the driving solar luminosity that reaches the Martian surface. The 1200 mb simulations show the same difference between faint young Sun and current solar luminosity. Though the circulations are more complicated, the primary differences, as seen in Figure 2.11 and Figure 2.22, are in the extratropical regions. The strength of the faint young Sun circulations are weaker, but generally within a factor of 2 of the current luminosity circulations.

The temperature and zonal wind fields also show similarities between the faint young Sun simulations and the current luminosity simulations. Figure 2.23 shows the northern spring air temperatures and zonal winds for the faint young Sun simulations. For the 6 mb simulation, the near surface temperature peaks at ~ 220 K while the polar regions cool down to ~ 150 K. The peak temperature is comparable to the current luminosity simulation (Figure 2.2(a)) but the latitudinal range of the warm temperatures is much smaller in the faint young Sun simulation. This latitudinal confinement of the warm regions in the atmosphere

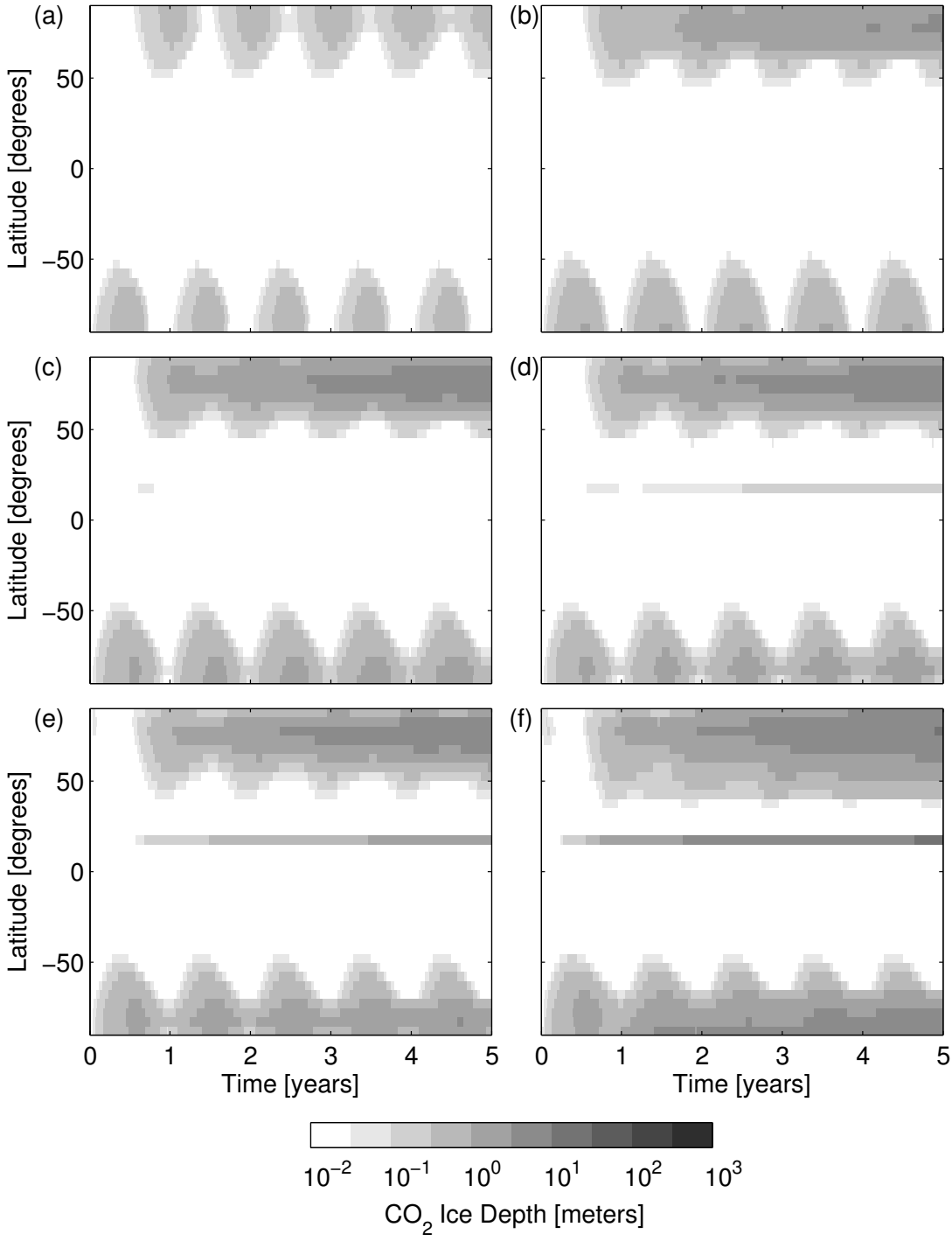

Figure 2.20: Zonal CO_2 ice versus time for 75% of the current luminosity. The plots include the following initial surface pressures: (a) 6 mb, (b) 60 mb, (c) 300 mb, (d) 600 mb, (e) 1200 mb, and (f) 3000 mb. The plots show the thickness of CO_2 ice assuming an ice density of 1600 kg/m^3.

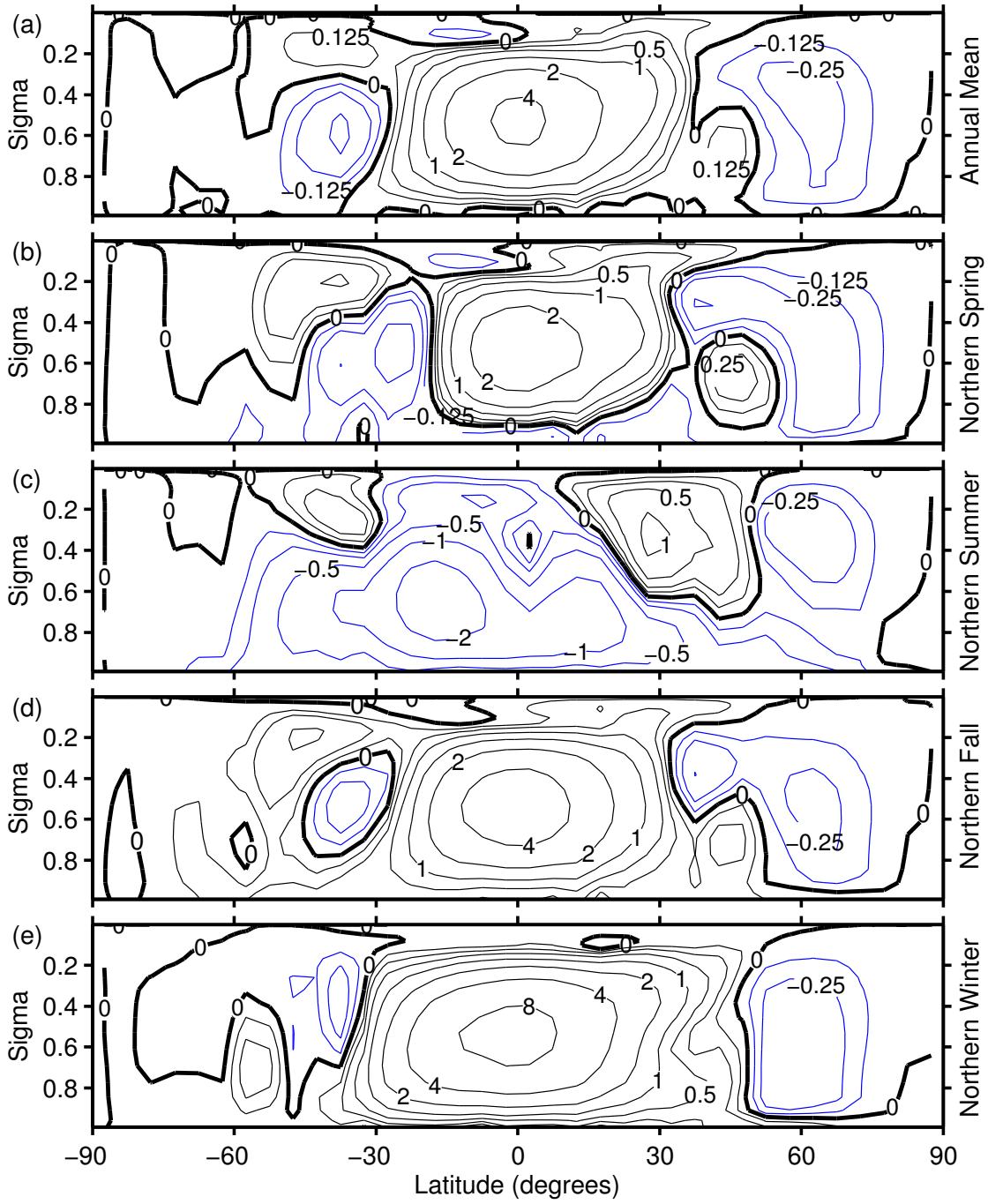

Figure 2.21: Annual and seasonal mean streamlines, in units of 10^9 kg/s, for the 6 mb atmosphere at 75% of current luminosity. Positive contours (black lines) correspond to clockwise rotation and use a geometric progression (0.125, 0.25, 0.5, 1, 2, 4, ...) for level spacings, while negative contours (blue lines) correspond to counter-clockwise rotation and also use a geometric progression (-0.125, -0.25, -0.5, -1, -2, -4, ...) for level spacings. The bolded solid black line is the zero streamline contour.

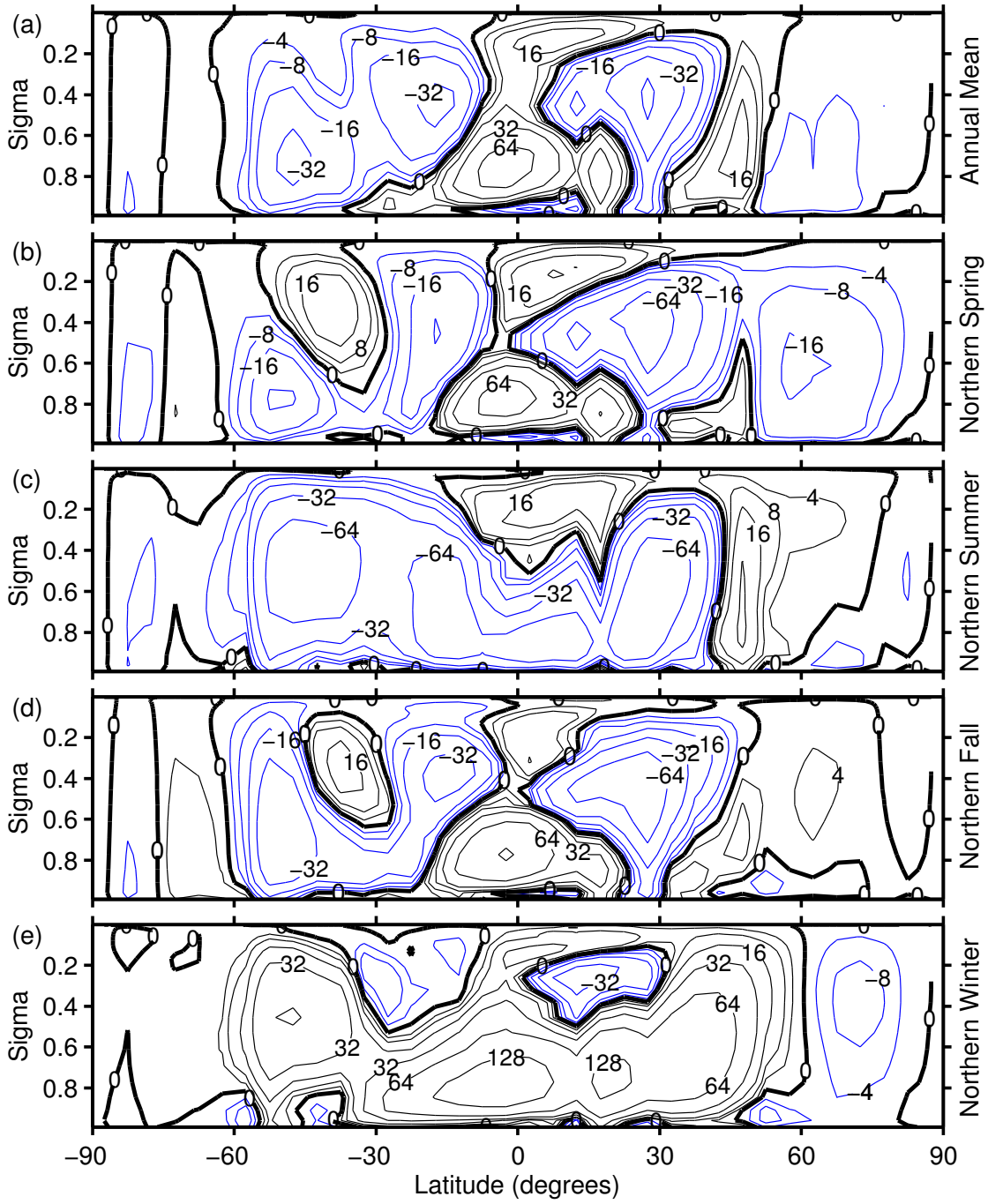

Figure 2.22: Annual and seasonal mean streamlines, in units of 10^9 kg/s, for the 1200 mb atmosphere at 75% of current luminosity. Positive contours (black lines) correspond to clockwise rotation and use a geometric progression (0.125, 0.25, 0.5, 1, 2, 4, ...) for level spacings, while negative contours (blue lines) correspond to counter-clockwise rotation and also use a geometric progression (-0.125, -0.25, -0.5, -1, -2, -4, ...) for level spacings. The bolded solid black line is the zero streamline contour.

is a consistent characteristic of the faint young Sun simulations. In the thicker atmospheres, the equatorial temperatures are not just more confined, but also cooler, and are accompanied by cooler temperatures in the polar regions (Figures 2.23(b) through 2.23(f)). The reduced temperatures in both equatorial and polar regions result in latitudinal temperature gradients that are similar to the current luminosity simulations. Thus, both the current luminosity and the faint young Sun simulations have zonal jets of similar strength and location.

In the northern summer simulations under the faint young Sun, the confinement of warm air leads to much colder temperatures at the north pole. For the 1200 mb simulation (Figure 2.24(e)), the north pole is 50 K to 60 K colder than the equivalent current luminosity simulation. The existence of this colder summer pole also changes the zonal wind structure. In the current luminosity simulations, the thicker atmospheres have smaller latitudinal temperature gradients at the north (summer) pole (Figures 2.3(b), 2.3(c), 2.3(d), 2.3(e)), and in the 3000 mb simulation the near surface latitudinal temperature gradient is essentially zero (Figure 2.3(f)). Thus, the thicker atmospheres have gradually weaker zonal winds, with no northern hemisphere midlatitude zonal jet in the 3000 mb case. The faint young Sum simulations, however, do not exhibit this change in zonal winds due to atmospheric thickness (Figure 2.24). The colder north (summer) pole air temperatures maintain a midlatitude north-south temperature gradient that sustains the zonal winds through thermal wind balance. The northern hemisphere zonal jet exists in all of the faint young Sum simulations during northern summer, in contrast to the current luminosity simulations.

The northern fall and northern winter seasonal means for the faint young Sun have similar features as the northern spring and northern summer. Compared to the current

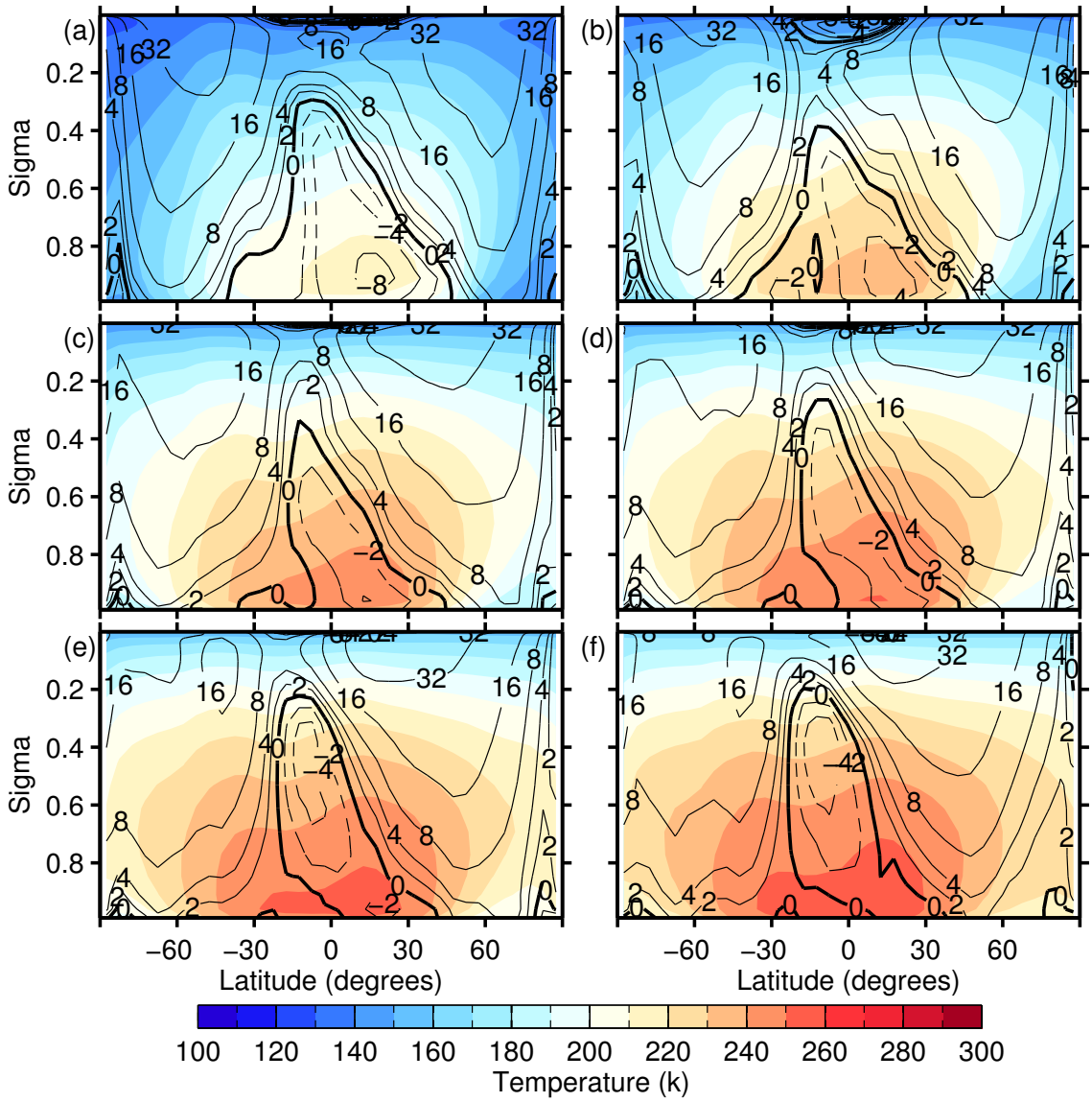

Figure 2.23: The seasonal mean of the zonal mean temperature (K) and zonal wind (m s^{-1}) for the northern spring ($L_s = 345$ to $L_s = 45$) as a function of mean surface pressure. The figure shows mean surface pressures of (a) 6 mb, (b) 60 mb, (c) 300 mb, (d) 600 mb, (e) 1200 mb, and (f) 3000 mb. The color contours represent air temperature, ranging from 100 K to 300 K. The solid black lines are contours of positive zonal wind with contour levels that uses a geometric progression (2, 4, 8, 16, ...) for level spacings. The bolded solid black line is the zero zonal wind contour. The dashed black lines are contours of negative zonal wind with contour levels that uses a geometric progression (-2, -4, -8, -16, ...) for level spacings.

luminosity simulations, the northern fall and northern winter air temperatures are more latitudinally confined with lower peak temperatures. Again, the polar temperatures are colder in the faint young Sun simulations than the current luminosity simulations and the summer pole zonal jet is much stronger in the faint young Sun simulations at higher atmospheric thickness.

In the surface wind maps for the faint young Sun simulations for northern spring and northern summer, as shown in Figures 2.25 and 2.26, the near surface winds are similar in magnitude and flow pattern to the current luminosity simulations. A close inspection of the wind maps shows regions where the wave activity and eddies differ from current luminosity, but the differences are small and may be due to the normal seasonal variation in the winds. The larger features exist in both faint young Sun and current luminosity equations, including planetary waves in the northern lowlands, the southern circumpolar circulation, stationary circulations around Hellas and Argyre Basins, and stationary eddies over the Tharsis Mons region. The histograms of the faint young Sun surface winds also tell a similar story to the current luminosity simulations: the thicker atmosphere leads to a narrower histogram with less extreme wind speeds and more moderate wind speeds. The lower insolation of the faint young Sun simulations does not seem to lead to lower wind speeds, neither in the peak wind speeds nor in the mean wind speeds. These results are also seen in the northern fall and northern winter simulations (not shown).

The trend of "similar but weaker" for the faint young Sun simulations continues with the meridional transport. The decomposition of the meridional transport of dry static energy for the faint young Sun simulations, shown in Figures 2.27 and 2.28, have a similar structure

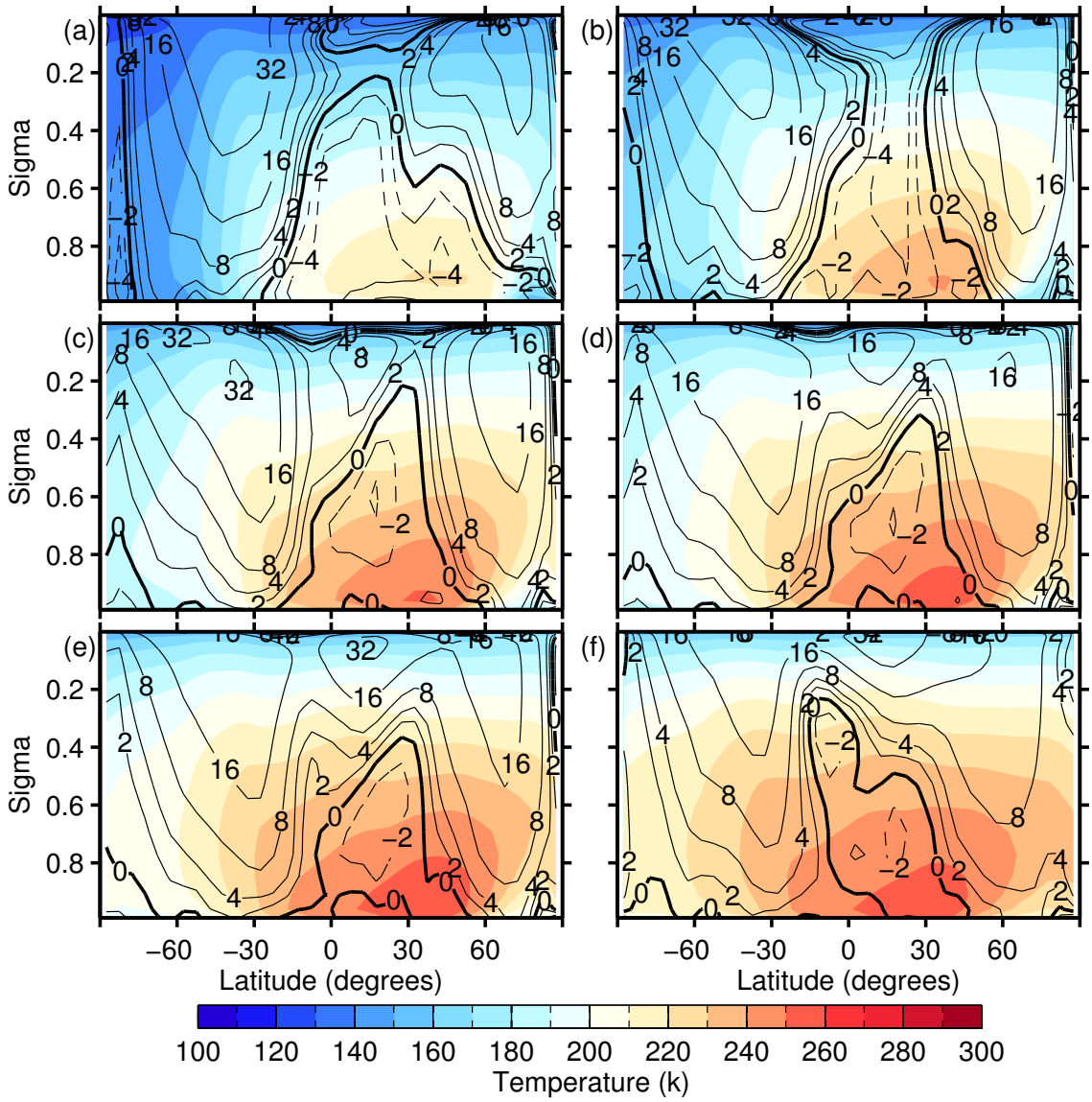

Figure 2.24: The seasonal mean of the zonal mean temperature (K) and zonal wind (m s^{-1}) for the northern summer ($L_s = 75$ to $L_s = 135$) as a function of mean surface pressure. The figure shows mean surface pressures of (a) 6 mb, (b) 60 mb, (c) 300 mb, (d) 600 mb, (e) 1200 mb, and (f) 3000 mb. The color contours represent air temperature, ranging from 100 K to 300 K. The solid black lines are contours of positive zonal wind with contour levels that use a geometric progression (2, 4, 8, 16, ...) for level spacings. The bolded solid black line is the zero zonal wind contour. The dashed black lines are contours of negative zonal wind with contour levels that use a geometric progression (-2, -4, -8, -16, ...) for level spacings.

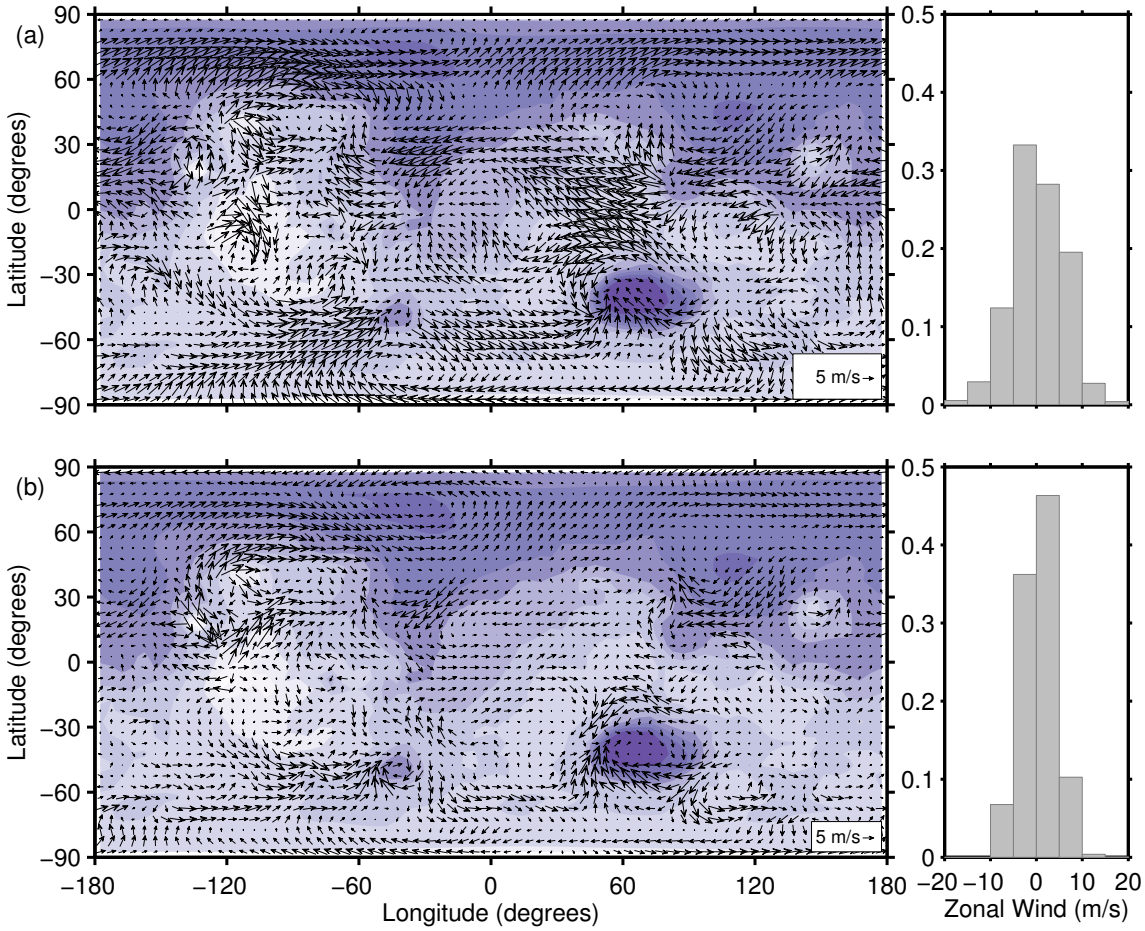

Figure 2.25: A map of surface winds and a histogram of the zonal wind speeds for (a) the 6 mb simulation and (b) the 1200 mb simulation. These results are for northern spring ($L_s = 345$ to $L_s = 45$). The vectors represent the resulting wind field due to the zonal and meridional winds. High elevation topography is shown as light purple contours and low elevation topography is shown as dark purple. The histogram shows the distribution of zonal wind speeds in 1 m s^{-1} bins. The 6 mb simulation has a mean zonal wind speed of 0.7 m s^{-1} and a standard deviation of zonal wind speeds of $\pm$ 6 m s^{-1}, while the 1200 mb simulation has a mean zonal wind speed of 0 m s^{-1} and a standard deviation of zonal wind speeds of $\pm$ 4 m s^{-1}.

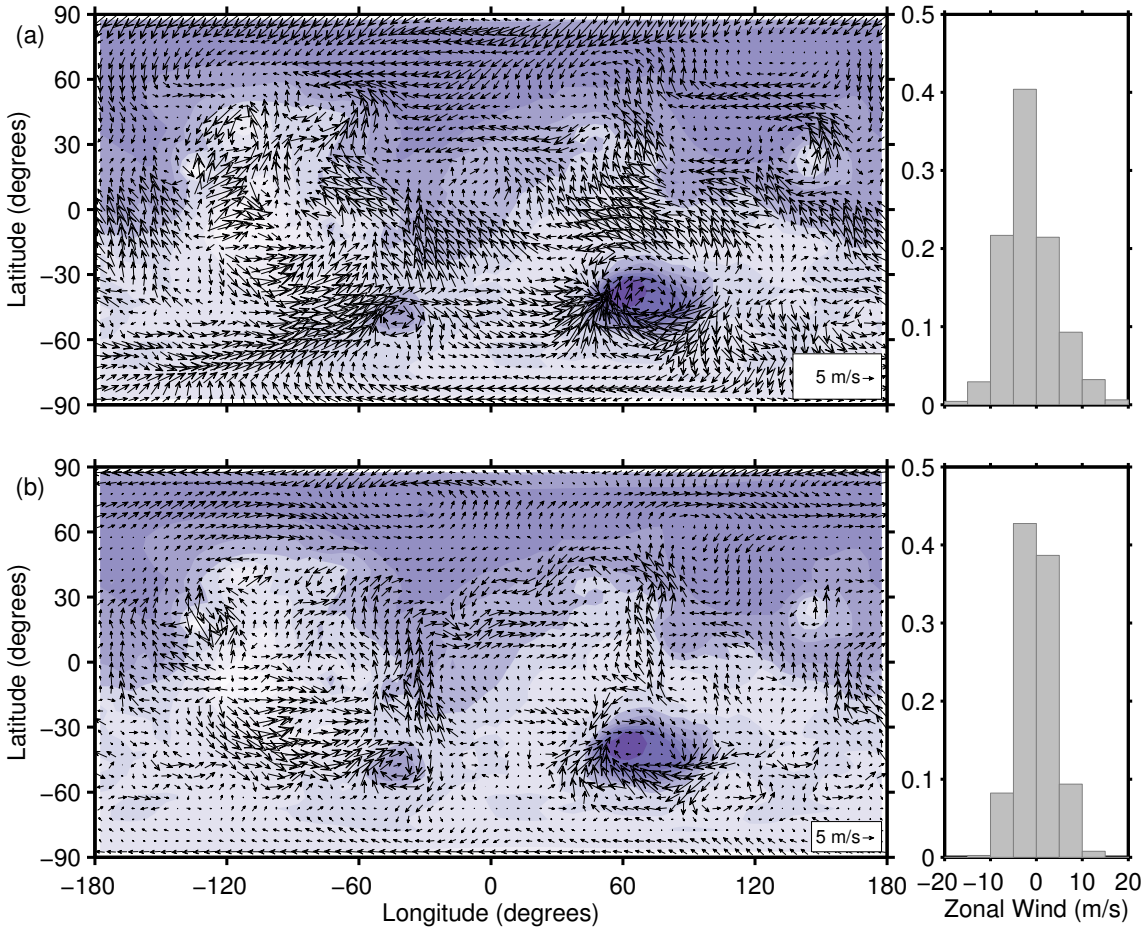

Figure 2.26: A map of surface winds and a histogram of the zonal wind speeds for (a) the 6 mb simulation and (b) the 1200 mb simulation. These results are for northern summer ($L_s = 75$ to $L_s = 135$). The vectors represent the resulting wind field due to the zonal and meridional winds. High elevation topography is shown as light purple contours and low elevation topography is shown as dark purple. The histogram shows the distribution of zonal wind speeds in 1 m s^{-1} bins. The 6 mb simulation has a mean zonal wind speed of 0.6 m s^{-1} and a standard deviation of zonal wind speeds of $\pm$ 6 m s^{-1}, while the 1200 mb simulation has a mean zonal wind speed of 0.4 m s^{-1} and a standard deviation of zonal wind speeds of $\pm$ 4 m s^{-1}.

to the current luminosity simulations. Again, the mean circulation dominates, especially at higher surface pressures. However, the magnitude of the transport is weaker in the faint young Sun simulations, by around 10% to 20% in most areas. The stationary eddies, in particular, are very suppressed. For example, in Figure 2.27(f) there are no stationary eddies in the northern hemisphere whereas in Figure 2.12, the current luminosity simulation, there is stationary activity throughout the northern midlatitudes. Other atmospheric thicknesses and seasons show this same phenomena in the faint young Sun simulations.

Breaking the mean circulation transport, $\left[\overline{v}\right]\left[\overline{E}\right]$, shown in Figures 2.29 and 2.30, into the overturning circulation transport, $\left[\overline{v}_o\right]\left[\overline{E}\right]$, and the condensation flow transport, $\left[\overline{v}_c\right]\left[\overline{E}\right]$, we see that the mean meridional transport of dry static energy in the faint young Sun simulations are similar to the current luminosity simulations in the tropics and differ in the extratropics, which is consistent with the differences seen in the streamfunction plots in Figures 2.21 and 2.22. When the mean meridional transports in Figures 2.29 and 2.30 are compared with the current luminosity mean meridional transports, shown in Figures 2.16 and 2.17, we see that the overturning circulation differs primarily in the extratropics, where the circulation is suppressed in the thicker atmosphere simulations. What is most surprising in the mean transport decomposition is that the condensation flow is not larger and more extensive, especially in the northern hemisphere. As seen in Figure 2.20, both polar regions are almost completely covered in at least 10s of centimeters of CO_2 ice. The condensation transport in these polar regions, however, show almost no difference between the faint young Sun and the current luminosity scenarios. One possibility is that the condensation flow towards Olympus Mons, which is the strongest feature in both scenarios, overwhelms

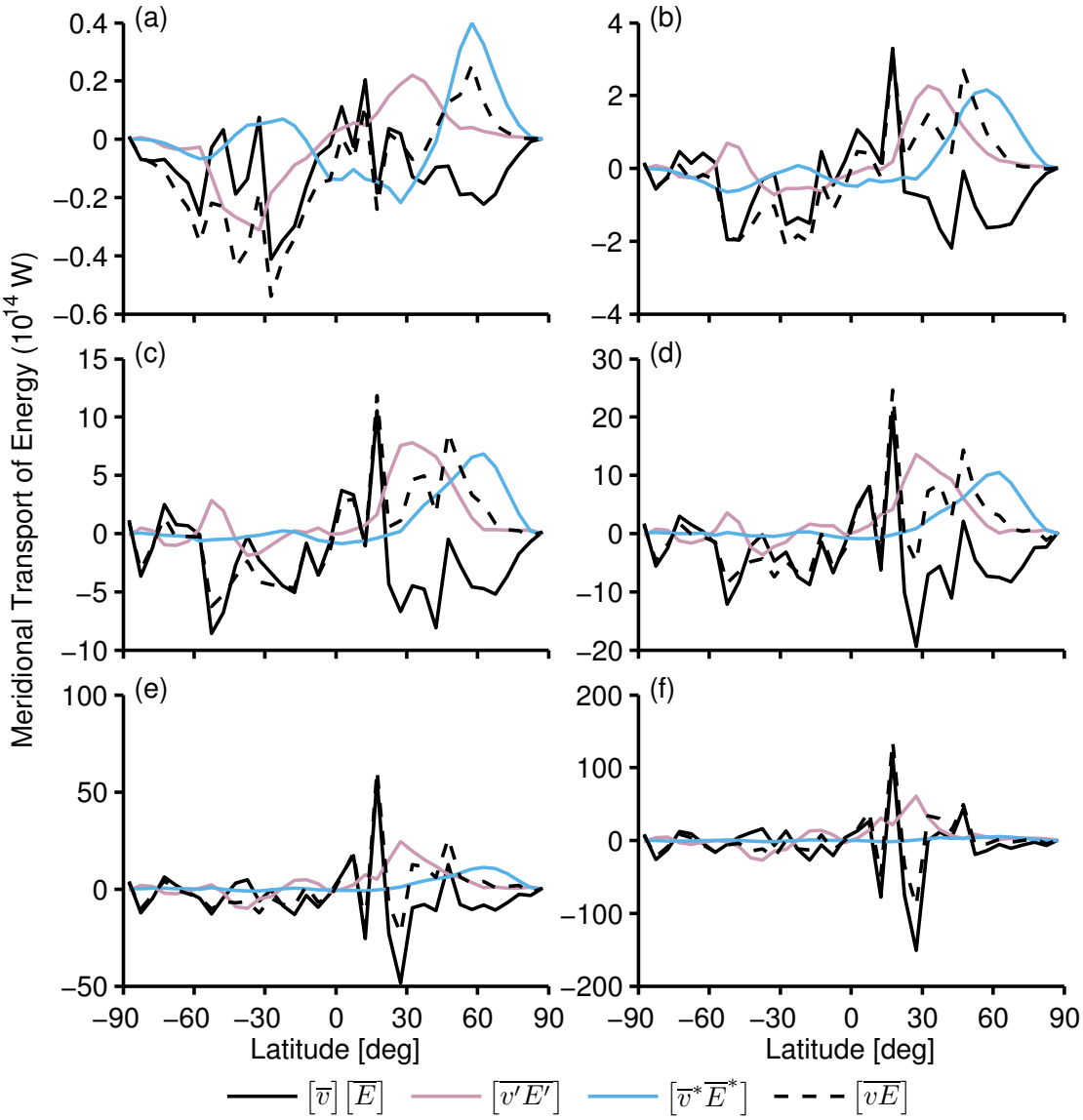

Figure 2.27: The meridional transport of dry static energy for $L_s = 345$ to $L_s = 45$ (northern spring) as a function of mean surface pressure. The figure shows mean surface pressures of (a) 6 mb, (b) 60 mb, (c) 300 mb, (d) 600 mb, and (f) 1200 mb. The solid black line is the mean circulation, $\left[\overline{v}\right]\left[\overline{E}\right]$, the light red line is the transient eddies, $\left[\overline{v'E'}\right]$, the blue line is the stationary eddies, $\left[\overline{v}^*\overline{E}^*\right]$, and the dashed black line is the total circulation, $\left[\overline{vE}\right]$.

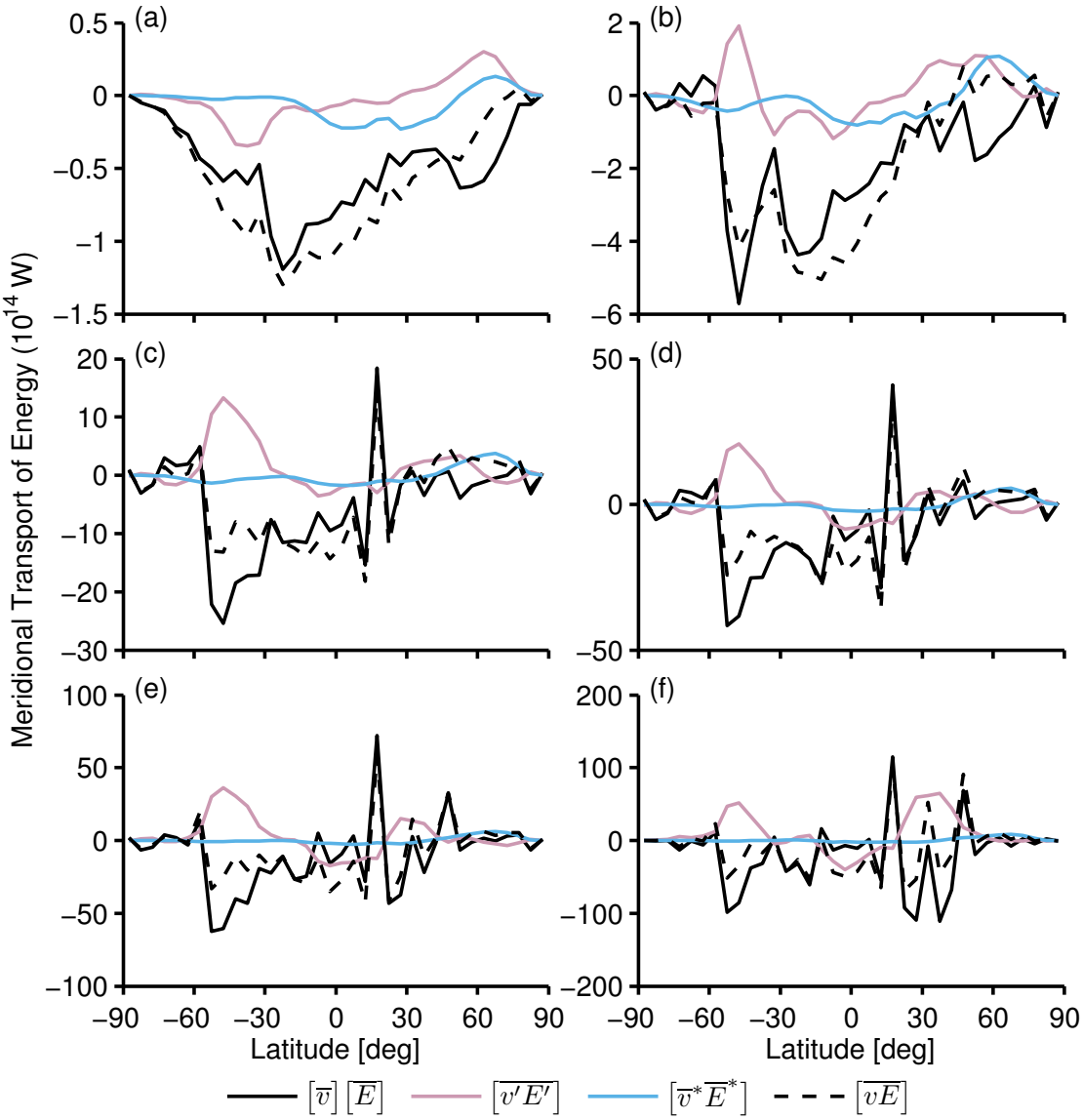

Figure 2.28: The meridional transport of dry static energy for $L_s = 75$ to $L_s = 135$ (northern summer) as a function of mean surface pressure. The figure shows mean surface pressures of (a) 6 mb, (b) 60 mb, (c) 300 mb, (d) 600 mb, and (f) 1200 mb. The solid black line is the mean circulation, $\left[\overline{v}\right]\left[\overline{E}\right]$, the light red line is the transient eddies, $\left[\overline{v'E'}\right]$, the blue line is the stationary eddies, $\left[\overline{v}^*\overline{E}^*\right]$, and the dashed black line is the total circulation, $\left[\overline{vE}\right]$.

the condensation flow towards the poles, but this explanation seems inadequate to explain the lack of increased condensation flow in the southern hemisphere. Again, like the other faint young Sun results, these results are similar in the two seasons not shown, i.e., northern fall and northern winter.

Overall, the faint young Sun simulations have a very similar dynamical appearance to the current luminosity simulations. The two exceptions are the colder air temperatures, especially in the polar regions at high latitudes, and the larger extent of CO_2 ice deposition. Differences in the mean atmospheric surface pressure have a larger effect on the climate dynamics than the changing luminosity.

2.5 Discussion

Our Martian paleoclimate simulations explored the consequences of changing two climate parameters: the mean atmospheric surface pressure and the solar luminosity. The sun very likely experienced a slow increase in solar luminosity over the lifetime of the solar system (*Gilliland*, 1989; *Gough*, 1981) so the Martian climate has spent the last 4 billion years responding to this change, regardless of the history of atmospheric thickness on Mars. Understanding the Martian climate's response to luminosity changes is therefore fundamental to understanding the Martian paleoclimate history. The mean atmospheric surface pressure is a much more speculative climate parameter. Despite the geologic evidence for a thicker ancient atmosphere, we still lack an understanding of how to create and sustain the required thicker atmosphere nor do we have a good estimate of how thick of an atmosphere is required. Still, we use how the climate would have changed under different mean thicknesses

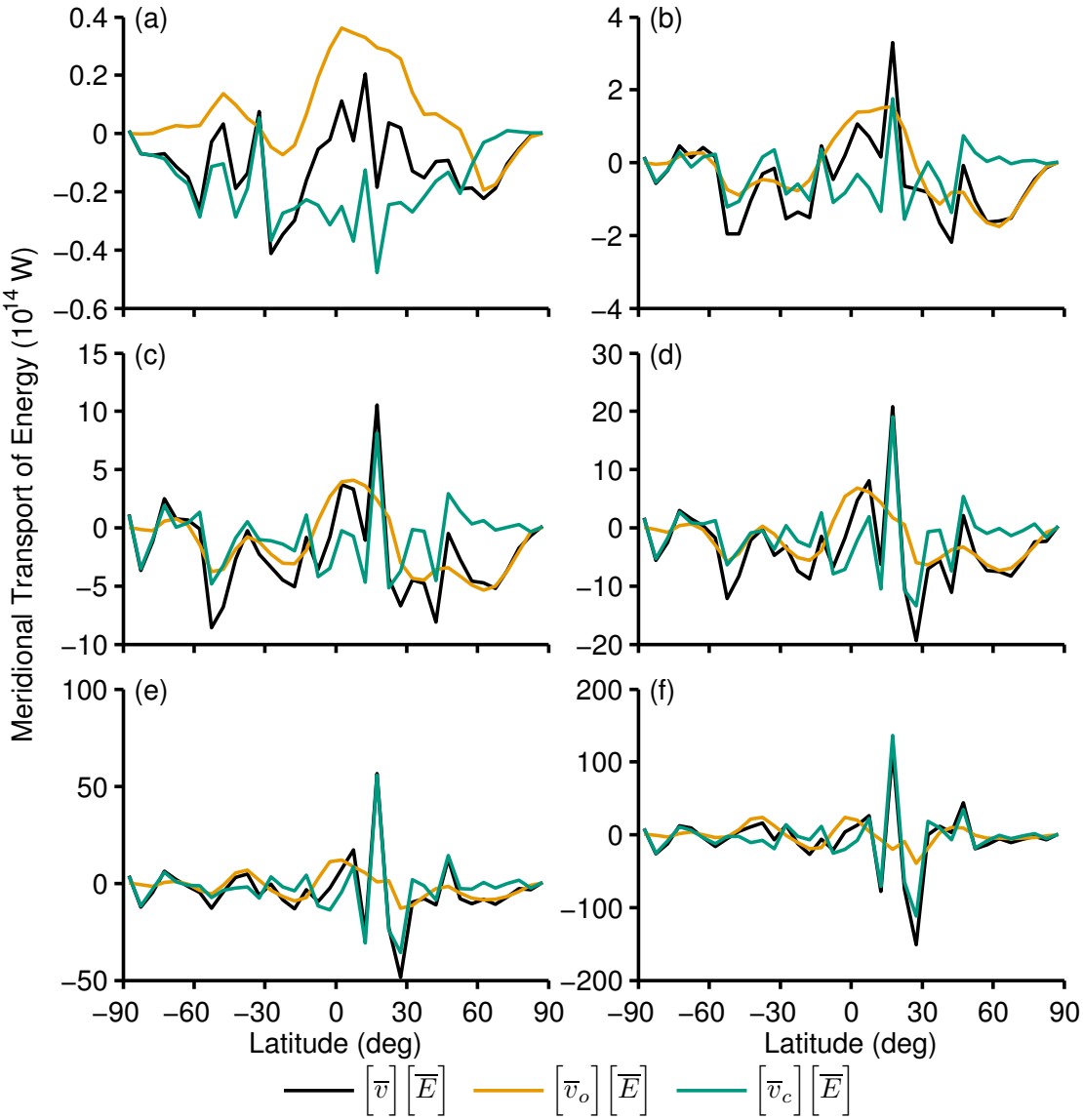

Figure 2.29: The mean meridional transport of dry static energy for $L_s = 345$ to $L_s = 45$ (northern spring) as a function of mean surface pressure. The mean transport is decomposed into the transport due to overturning cells and the transport due to condensation flow. The plots include the following initial surface pressures: (a) 6 mb, (b) 60 mb, (c) 300 mb, (d) 600 mb, (e) 1200 mb, and (f) 3000 mb. The solid black line is the total mean circulation, $\left[\overline{v}\right]\left[\overline{E}\right]$, the orange line is the overturning circulation, $\left[\overline{v}_o\right]\left[\overline{E}\right]$, and the green line is the condensation flow, $\left[\overline{v}_c\right]\left[\overline{E}\right]$.

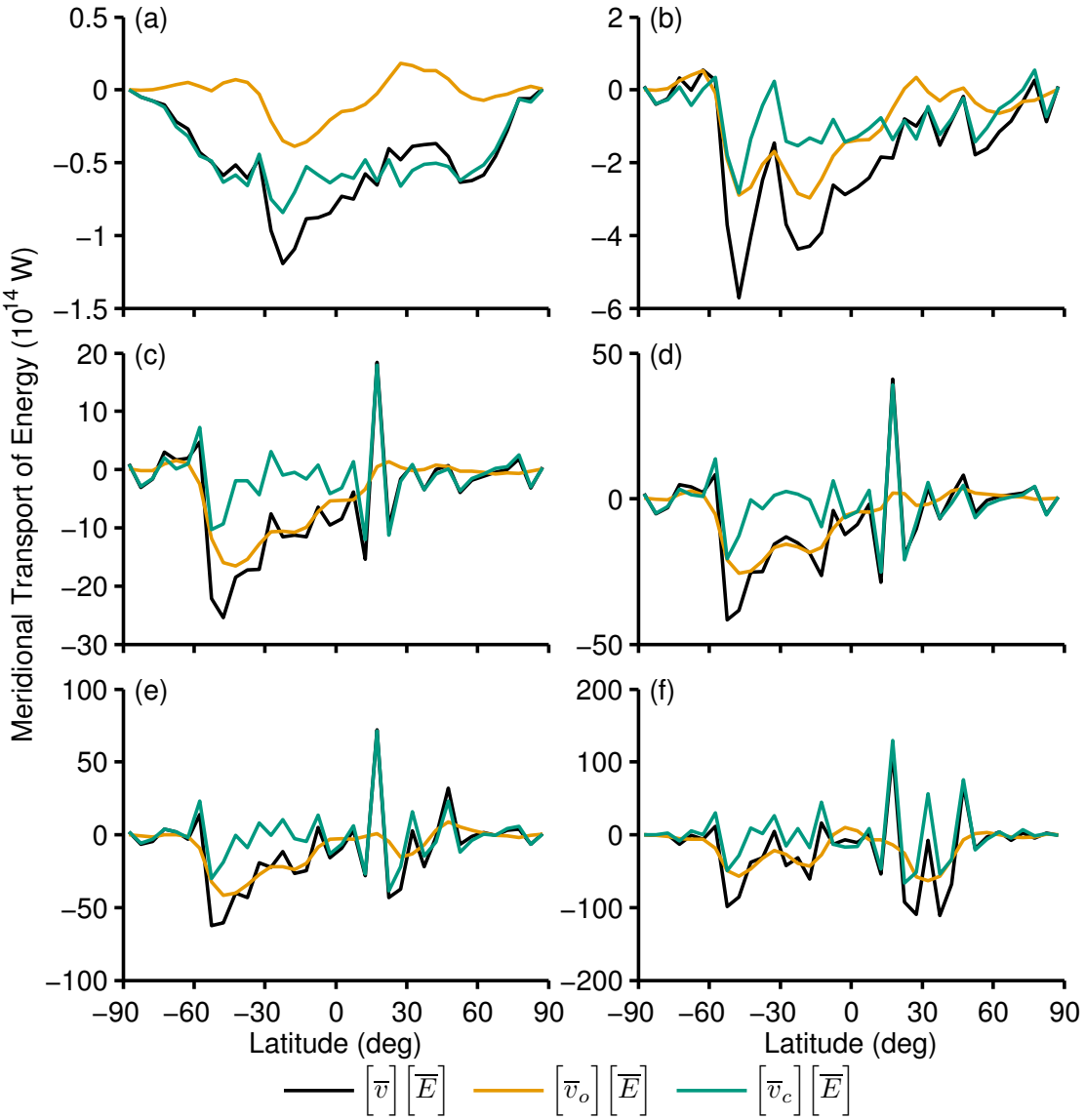

Figure 2.30: The mean meridional transport of dry static energy for $L_s = 75$ to $L_s = 135$ (northern summer) as a function of mean surface pressure. The mean transport is decomposed into the transport due to overturning cells and the transport due to condensation flow. The plots include the following initial surface pressures: (a) 6 mb, (b) 60 mb, (c) 300 mb, (d) 600 mb, (e) 1200 mb, and (f) 3000 mb. The solid black line is the total mean circulation, $\left[\overline{v}\right]\left[\overline{E}\right]$, the orange line is the mean meridional circulation, $\left[\overline{v}_o\right]\left[\overline{E}\right]$, and the green line is the condensation flow, $\left[\overline{v}_c\right]\left[\overline{E}\right]$.

as a constraint on possible paleoclimate states for the Martian climate.

The atmosphere interacts with the solid earth in numerous ways, but for our investigation two important interactions are erosion and deposition. Surface winds play a role in the mechanical erosion of surface materials as well as transport of other material, e.g., dust or water, that can also contribute to mechanical and chemical erosion. The large-scale circulation and its associated zonal and meridional winds are also important in the transport of eroding materials. The combined actions of the large-scale circulation and surface winds control the location and strength of erosion, and by a similar argument, the deposition of transported material.

Of the two climate parameters that we investigated, the mean atmospheric surface pressure has the largest impact on atmospheric winds and transport. As we previously showed, at all seasons the surface winds for the thicker atmospheres are confined to a narrower range of lower velocities. In the thicker atmosphere the number of peak winds in excess of ± 10 m s^{-1} are significantly less than in the thin atmosphere cases. But even in a weaker wind regime, the thicker atmospheres have the potential to lift greater amounts of dust due to the decreasing power law relationship between atmospheric density and the threshold velocity for dust lifting (*Armstrong and Leovy*, 2005). Thus, the threshold for dust lifting is lower in the thicker atmospheres and it is quite possible that even with the narrower range of wind speeds that the thicker atmosphere cases lead to a larger amount of dust lifting and thus erosion and deposition.

Once dust is lifted, where the dust is transported also has important consequences on the recorded surface geology. As we have seen, the general path of the winds does not

significantly change between different mean atmospheric surface pressures nor between different luminosities. Nor does change in the obliquity changed the path of the winds (*Fenton and Richardson*, 2001). The large-scale path of surface winds appears to be relatively constant throughout the Martian history. This increases the chance that source and sink regions have remained constant, which is consistent with recent observations of Mars (*Szwast et al.*, 2006). For example, aeolian deposits have been observed in the Arabia Terra region, including possible quasi-periodic bedding of aeolian deposits (*Lewis et al.*, 2008). Our simulations show consistently strong flows into the Arabia Terra region from both the south and north throughout much of the Martian year. This flow occurs in both thin and thick atmospheres and for both faint and current solar luminosity. But with its higher dusting lifting capacity, the thicker atmosphere conditions may have pumped in greater amount of dust in a limited time. The combination of increased dust lifting due to mean atmospheric surface pressure and changing atmospheric thickness due to obliquity cycling may be a possible mechanism for the creation of the quasi-periodic bedding at locations like Arabia Terra (*Haberle et al.*, 1994; *Kreslavsky and Head*, 2005; *Manning et al.*, 2006; *Lewis et al.*, 2008). Further work is required for a definitive assessment, but the possibility is intriguing.

The low solar luminosity generates much more surface CO_2 ice over a wider range of the planet, which is consistent with earlier work on the early Martian climate (*Haberle et al.*, 1994; *Haberle*, 1998). There is a positive feedback between the low solar luminosity and the mean atmospheric pressure since the colder surface temperatures drive increased CO_2 condensation which results in a thinner atmosphere and even colder surface tempera-

tures. Thus, the thick atmospheres during the era of the faint young Sun could have existed only transiently through the contribution of another heating source in the system, e.g. sulfates, water, etc (*Haberle*, 1998; *Johnson et al.*, 2008, 2009).

2.6 Conclusion

We have investigated the three dimensional climate dynamics of thin and thick atmospheres on Mars over the range of possible solar luminosities. We found that the difference in global mean atmospheric surface pressure has the largest impact on the structure of large-scale circulation, the strength of surface winds, and the meridional transport of energy. The different solar luminosities have the largest control on temperatures and CO_2 condensation. There is a clear feedback between the effects of surface pressure and solar luminosity, but the details of this feedback are not explored in this investigation. The wind velocity generated by the condensation of CO_2 , i.e., the condensation flow, strongly affects the mean meridional circulation. This effect grows more pronounced in the thicker atmosphere simulations. Unlike condensation flows on Earth, which are due to the condensation of water, the CO_2 driven condensation flow on Mars can be a significant part of the global circulation.

For this investigation, we used a CO_2 only atmosphere with no orbital eccentricity. Though these two assumptions simplified the simulation process, the effect of changes these assumptions must be addressed in future work. The inclusion of radiatively active dust would provide a source of internal heating to the Martian climate, which would be especially important during the faint young Sun era. In the current Martian climate, the ec-

centricity leads to an asymmetry in the annual distribution of insolation. This asymmetry is seen in the different strength of the two solstitial circulations. As the eccentricity changes and as the longitude of perihelion cycles around the Martian orbit, the impact of the insolation asymmetry will change. In this study, we have not investigated how the climate dynamics would respond to this changing insolation as a function of mean atmospheric pressure nor solar luminosity.

Acknowledgements

I would like to thank Mark Richardson and Christopher Lee of Ashima Research and Tapio Schneider of Caltech for helpful discussions about Reynolds analysis in mass divergent flows. I am also grateful for general advice on this research from Michael Mischna of JPL.

Chapter 3

Climate Dynamics of Atmospheric Collapse on Mars

Abstract

One- and two-dimensional global energy balance models of the Martian atmosphere have predicted that early in Martian history, for a range of initial total CO_2 inventories, the CO_2 atmosphere would precipitate and/or deposit CO_2 until it reached a vapor pressure, or cap-buffered, state. This is commonly referred to as atmospheric collapse. A collapsed state may limit the amount of time available for physical and chemical weathering. The global energy balance models that predict atmospheric collapse model the atmospheric heat transport, which controls atmosphere collapse, in terms of a single, globally uniform parameter. Proper representation of the atmospheric heat transport is critical when the atmosphere is near a significant transition, such as the threshold for collapse. The threshold for collapse may be controlled by the total CO_2 inventory, the orbital parameters, and the solar insolation. Using the Mars Weather Research and Forecasting (MarsWRF) general circulation model, we investigate the details of the three-dimensional, time-varying heat transport at the threshold for atmospheric collapse.

3.1 Introduction

The evolution of the Martian atmosphere is a fundamental problem in both atmospheric and geological science. Study of the Martian surface shows a rich history of chemical and physical modification, which suggests a more active and clement surface environment in the past (*Squyres et al.*, 2004; *Grotzinger et al.*, 2005; *Barnhart et al.*, 2009; *Fassett and Head*, 2008; *Hynek and Phillips*, 2003; *Craddock and Howard*, 2002). A long-standing problem has been reconciling the current thin and cold atmosphere with this presumably thicker and warmer environment (*Haberle*, 1998; *Forget and Pierrehumbert*, 1997; *Jakosky and Phillips*, 2001; *Kasting*, 1991; *Pollack et al.*, 1987). Atmospheric loss to space can erode only limited quantities of carbon dioxide (*Luhmann et al.*, 1992; *Kass and Yung*, 1995), while the absence of extensive carbonate deposits on the Martian surface has cast doubt on the role of chemical weathering as a primary loss mechanism (*Bandfield et al.*, 2000; *Bandfield et al.*, 2003; *Bibring et al.*, 2005). Impact erosion fluxes are still somewhat uncertain following the late heavy bombardment. Though some have argued for the importance of impact erosion, e.g., *Melosh and Vickery* (1989) and *Brain and Jakosky* (1998), the efficacy of impacts for removing a significant fraction of the atmosphere is still uncertain (cf. *Melosh and Vickery* (1989) and *Newman et al.* (1999)) and it is not the predominant sink of CO_2 after the first billion years (*Brain and Jakosky*, 1998). This problem has spawned efforts to track the evolution of the planetary CO_2 budget for a range of reservoirs and loss processes.

An important constraint on the evolution of the Martian atmosphere is the partitioning of the Martian CO_2 inventory into the atmosphere and surface. When the solar and thermal

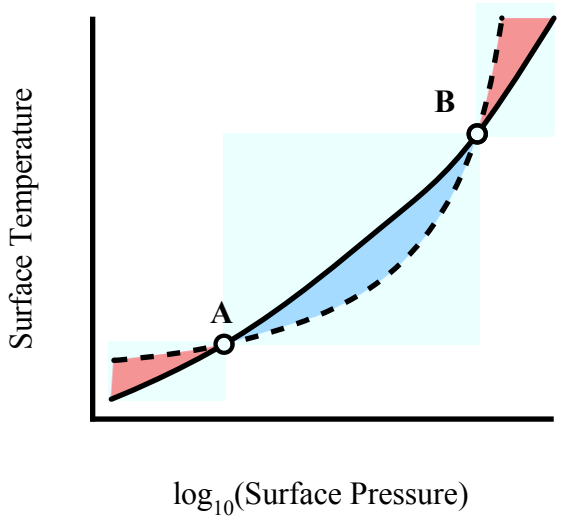

Figure 3.1: The model of the relationship between polar surface temperature and condensation temperature as developed by *Gierasch and Toon* (1973) and *McKay et al.* (1991). The solid black line represents a condensation curve for CO_2 . The dashed black line represents the modeled polar surface temperature assuming atmospheric heat transport and a greenhouse effect. Point A and B in Figure 3.1 are the transition points between a non-collapsed atmosphere (red region) and a collapsed atmosphere (blue region).

energy that arrives at the surface of Mars is low enough, the resulting surface temperature can be below the condensation temperature of CO_2 . The atmosphere either completely condenses on to the surface or achieves a thermodynamic balance between the atmosphere and surface reservoirs of CO_2 . Using a model that calculated the surface energy balance as a function of latitude, *Leighton and Murray* (1966) showed that for a given total inventory of CO_2 the martian atmosphere should achieve a thermodynamic balance where the CO_2 partitions between the atmosphere and the surface ice. The global mean atmosphere pressure is thus determined by this balance.

Gierasch and Toon (1973) expanded the work by *Leighton and Murray* (1966) by including the equator-to-pole heat transport in their energy balance model. Using an eddy heat flux parameterization developed by *Stone* (1972), which allowed *Gierasch and Toon*

(1973) to simulate the poleward transport of heat by baroclinic waves, they investigated how the CO_2 atmosphere-ice balance responds to changes in the total CO_2 inventory and changes in the poleward heat transport. When *Gierasch and Toon* (1973) compared the CO_2 vapor pressure curve to their polar surface temperatures calculated for various values of insolation and atmospheric pressure they found a range of stable solutions for the Martian atmosphere-ice system. Figure 3.1 conceptually shows the relationship between polar surface temperature and condensation temperature identified by *Gierasch and Toon* (1973). At high insolation the polar surface temperature would remain above the vapor pressure curve for almost the whole range of atmospheric pressures. From ~ 0.1 mb to ~ 1 bar the highest insolation calculations never produced any CO_2 ice caps. The lowest insolation calculations, however, crossed below the vapor pressure curve at around 1 mb and remained below the vapor pressure until very high pressures (~ 1 bar). Where the temperature curves intersected the vapor pressure curve this was a solution where the atmosphere was in vapor pressure balance with the polar surface ice (point A in Figure 3.1), just as predicted by *Leighton and Murray* (1966). When the polar surface temperature is below the vapor pressure curve, then runaway condensation of CO_2 will be triggered at the poles and the atmosphere will collapse[1] to point A in Figure 3.1. Thus, the Martian atmosphere can experience three types of climate: first, an inflated, ice-free climate that occurs above point B in Figure 3.1, second, a vapor pressure balance climate where atmospheric CO_2 and ice coexist at point A, and third, a collapsed climate where the only atmospheric constituents are the non-condensable gases, such as argon and nitrogen, and where the CO_2 consists of

[1] We define the term "collapse" or "collapsed atmospheric state" as the presence of at least one permanent CO_2 ice cap, and the secular growth of this permanent cap over multiple years.

surface ice sheets (*McKay et al.*, 1991; *Haberle et al.*, 1994; *Nakamura and Tajika*, 2002) . *Gierasch and Toon* (1973) found that occurrence of these three climate types is sensitive to the total CO_2 inventory, the insolation, the atmospheric emissivity, and the conductivity between the atmosphere and the surface.

Later research added to this early work on the stable states of the Martian climate by expanding the simple models to include more feedbacks and physics. *McKay et al.* (1991) extended the *Gierasch and Toon* (1973) model by adding the greenhouse effect, which is a positive feedback between atmospheric pressure and temperature and by defining the equator-to-pole temperature difference as an exponential function of pressure. By doing so, *McKay et al.* (1991) found that at both high atmospheric pressure (> 100 mb, i.e., above point B in the model shown in Figure 3.1) and low atmospheric pressure (a few millibar, i.e., below point A in the model shown in Figure 3.1) there was "runaway" inflation of the atmosphere such that all of the CO_2 was atmospheric. Between these two extremes (i.e., between points A and B), the Martian climate was in a collapsed state, bookended by two values of CO_2 pressure where the atmosphere and surface ice were in vapor pressure equilibrium (points A and B in Figure 3.1). *Haberle et al.* (1994) arrived at a similar result using a two different greenhouse models and accounting for the meridional heat transport into the polar region.

Nakamura and Tajika (2001) built upon this work by exploring how the latitude of the polar cap ice line is determined by insolation and mean atmospheric pressure. They again found multiple stable climates whose existence is determined by the balance of heat transport, greenhouse warming, and solar insolation. Later work with the same model

showed that when seasonal variations in insolation are included in the calculations the existence of multiple solutions to the climate becomes dependent on the total CO_2 inventory in the Martian climate system (*Nakamura and Tajika*, 2002).

Another constraint on the the evolution of the Martian climate is the gradual increase in the Sun's luminosity over the lifetime of the solar system. About 4.7 billion years ago the solar luminosity was 70% of current luminosity (*Gilliland*, 1989; *Gough*, 1981). Since luminosity drives the dynamics of a planetary atmosphere, this reduced luminosity, or "faint young Sun", must have impacted the ancient Martian climate. To investigate the climate consequences of the faint young sun, we used a solar luminosity of 75% of current luminosity for a set of the MarsWRF simulations. By using 75% of current luminosity we are essentially simulating the middle of the Noachian, which occurred 4 billion years ago and is an era during which Mars may have had a thick atmosphere (*Haberle*, 1998). As well, the 75% value is consistent with other paleoclimate studies, including *Mischna et al.* (2000), *Colaprete and Toon* (2003), and *Johnson et al.* (2008).

Cyclical variations in Mars' orbit also contributed to the overall long-term secular evolution of the Martian atmosphere. The obliquity ε, or spin axis tilt, of Mars varies throughout Martian history (*Ward*, 1974; *Laskar and Robutel*, 1993; *Laskar et al.*, 2004). The precession of the orbit plane of Mars generates the primary obliquity oscillation, with a period of ~ 120,000 years (*Ward*, 1974; *Laskar et al.*, 2002). The amplitude of this obliquity oscillation is then modulated by changes in orbital inclination, with a period of 1.2 million years (*Ward*, 1974), and by a secular resonance, with a period of 2.4 million years (*Laskar et al.*, 2002). Finally, the mean value of the obliquity changes chaotically over the lifetime

of Mars (*Ward and Rudy*, 1991; *Laskar et al.*, 2004). *Laskar et al.* (2002) showed that over 250 million years the obliquity ranges from $\varepsilon = 0.043°$ to $\varepsilon = 66.154°$ and that statistical models of the 5 billion year evolution of the Martian orbit shows an obliquity range of $\varepsilon = 0°$ to $\varepsilon = 82.035°$. Thus, it is possible that Mars spent some part of its history with an obliquity less than $20°$ and possibly as low as $0°$, which is important since variations in the Martian obliquity lead to changes in the latitudinal distribution of insolation at the Martian surface (*Ward*, 1974; *Laskar et al.*, 2002). This latitudinal distribution of insolation determines the global equator-to pole surface temperature gradient, the formation of polar CO_2 caps, and the global mean surface pressure of the atmosphere (*Leighton and Murray*, 1966; *Ward et al.*, 1974; *Toon et al.*, 1980; *Cutts and Lewis*, 1982; *Fanale et al.*, 1982; *Laskar et al.*, 2002).

Although the dynamics of CO_2 ice caps had already been extensively examined in terms of seasonal and orbital forcing (e.g., *Leighton and Murray* (1966), *Ward* (1974), *Ward et al.* (1974), and *Fanale et al.* (1982)), the timing of perennial CO_2 cap formation in Mars history had not been formally addressed before the Mars atmosphere evolution study of *Haberle et al.* (1994). A major finding of *Haberle et al.* (1994) was that surprisingly early in planetary history, and for a range of initial total CO_2 inventories, the atmosphere would be unable to transport enough heat to the poles to stave off year-round CO_2 polar caps. *Manning et al.* (2006) found that the obliquity cycles created cycles of atmospheric collapse and non-collapse throughout the Martian history. If Mars were trapped in a collapsed state for extended periods of its planetary history, the amount of time available for physical and chemical weathering would, as a result, be greatly limited.

A standard geological paradigm for the history of Mars requires a thick atmosphere, of a few hundred millibars global mean surface pressure or greater, to create periods of warm and wet near surface conditions through much of the Noachian, and at least episodic periods of warmth since that time to form valley systems that are a geomorphic hallmark of surface water flow (*Andrews-Hanna and Lewis*, 2011; *Carr and Head III*, 2010; *Fassett and Head*, 2011; *Grotzinger et al.*, 2005). Observations of olivine and hydrothermal clay mineral deposits suggest that the surface of Mars that could have been largely cold and dry throughout its history (*Hurowitz and McLennan*, 2007; *Ehlmann et al.*, 2011), while geomorphological features like valley networks, sedimentary deposits, and lake basins bolster the argument that early Mars was warm and wet (*Malin and Edgett*, 2003; *Fassett and Head*, 2008; *Metz et al.*, 2009; *Hynek et al.*, 2010). If collapse indeed occurs, it is important for understanding the geological history of Mars and needs to be considered as part of the geological paradigm that already includes water ice ages on Mars (*Head et al.*, 2003). As well, if collapse did occur, previous paleoclimate evolution models are possibly missing important physics and presumably incorrectly predicting the history of volatile abundance as a result.

The prediction of collapse in the extant global-mean climate models (e.g., *Haberle et al.* (1994) and *Manning et al.* (2006)) involves representation of an inherently three-dimensional, time-varying process, heat transport, in terms of a single, globally uniform 'constant'. This constant is unavoidably the weakest link in any low-order (zero-dimensional and one-dimensional) atmospheric evolution model, since the proper representation of heat transport is of critical importance when the atmosphere is near a significant transi-

tion, such as the threshold for collapse. The latitudinal dependence of ice cap formation and of the thermal forcing of the surface also suggest the need for a higher-dimensional study (*Haberle et al.*, 1994). Here we report the first application of a sophisticated, three-dimensional global climate model to access the formation of massive early caps. Our first step focuses on the most extreme possible condition for atmospheric collapse, which would occur whenever Mars reaches extremely low to zero obliquity. Then, treating the zero obliquity results as a control, we explore the relationships between atmospheric collapse, obliquity, and heat transport. In particular, we investigated the validity of the Gierasch-Toon-McKay model for polar surface temperatures (*Gierasch and Toon*, 1973; *McKay et al.*, 1991).

3.2 Methodology

The response of a climate system to a climate perturbation falls into one of two categories: slow response and fast response (*Saltzman*, 2002). A slow response in a climate system requires a significant amount of time to adjust to perturbations (*Saltzman*, 2002). For a climate system like Mars, perturbation response timescales of 10s of years or longer are considered slow response. Alternatively, a fast response in a climate system reacts quickly to perturbations from equilibrium (*Saltzman*, 2002), usually with a timescale of a few years or less. The long term evolution of a climate incorporates both of these response regimes. Unfortunately, studying both slow and fast responses with a single model is usually computationally difficult and impractical. Instead, separate models can be used to study the two types of responses, individually.

The work of *Haberle et al.* (1994) and *Manning et al.* (2006) investigated the slow response of the Martian paleoclimate CO_2 cycle to perturbations of the planetary energy balance due to orbital variations. These studies were specifically looking at long term secular and periodic changes in a variety of CO_2 reservoirs and sinks (atmosphere, surface, regolith, space). Since both the adsorption of CO_2 into the regolith reservoir and the loss of CO_2 to space are slow processes, their models were appropriate for investigating such a slow response system. However, the exchange of CO_2 between the atmospheric and surface reservoirs is rapid and, in order to accurately capture the relevant physics, must be simulated by a model that resolves fast responses. This is especially true when the climate undergoes geologically rapid transitions (see various results in *Haberle et al.* (1994) and *Manning et al.* (2006)).

By using a three-dimensional general circulation model (GCM), which calculates the dynamical equations in latitude, longitude, and height, we are able to study the fast response of the Martian paleoclimate CO_2 cycle to perturbations in the planetary energy balance. Whereas *Haberle et al.* (1994) and *Manning et al.* (2006) focused on the slow exchange of CO_2 between reservoirs while simply parameterizing the atmosphere transport of energy, we, essentially, did the opposite. We focused on the relationship between atmospheric energy transport and planetary energy balance in controlling the distribution of CO_2 between the atmosphere and the surface. In fact, the regolith and atmospheric loss reservoirs are omitted from our model. Any changes to the CO_2 concentration in the regolith or the CO_2 loss rate to space are negligible on the time scale of our simulations. By focusing on the fast response of the Martian paleoclimate we complement the previous

work of *Haberle et al.* (1994) and *Manning et al.* (2006).

For our study, we used the Mars Weather Research and Forecasting (MarsWRF) GCM, developed by *Richardson et al.* (2007). *Richardson et al.* (2007) created MarsWRF by generalizing and globalizing the NCAR Weather Research and Forecasting model (*Skamarock et al.*, 2005). The model compares well to other leading Martian GCMs (see, e.g., section 4 in *Richardson et al.* (2007) and Figure 1 in *Johnson et al.* (2008)). MarsWRF solves the primitive equations on a finite difference mesh using an Arakawa C-grid. MarsWRF includes a full CO_2 cycle, current Mars topography, and current surface albedo and thermal properties that are used to drive a subsurface heat diffusion and surface energy balance scheme. As described in *Richardson et al.* (2007), the model calculates CO_2 sublimation and condensation and adjusts the CO_2 ice and atmosphere inventories, along with the column mass and pressure, accordingly. Although dust and water vapor would affect the heating and temperature profile in our model, we do not include dust nor water vapor in our simulations Since our focus is on how climate dynamics are affected by CO_2. For radiation calculations, we use a two-stream radiation code that implements a k-distribution radiative transfer scheme. This method for calculating the radiative transfer preserves much of the accuracy of line-by-line calculations while remaining computationally fast enough for use in a three-dimensional GCM. A general description of the k-distribution scheme can be found in *Lacis and Oinas* (1991) and *Fu and Liou* (1992), among other references, while details of the MarsWRF implementation of the k-distribution scheme are given by *Johnson et al.* (2008). Simulations are run with a latitude and longitude resolution of $5^\circ \times 5^\circ$ and with 40 vertical levels provided by a terrain-following modified sigma vertical coordinate.

We do not include a CO_2 cloud scheme that would be required at the higher atmospheric pressures (*Forget and Pierrehumbert*, 1997; *Mischna et al.*, 2000; *Colaprete and Toon*, 2003). For our work this is a reasonable choice since it is not clear whether CO_2 clouds would warm or cool the atmosphere (*Forget and Pierrehumbert*, 1997; *Mischna et al.*, 2000; *Colaprete and Toon*, 2003). For surface temperature calculations, a multilayer subsurface thermal diffusion and surface energy balance model uses surface albedo and thermal inertia maps derived from orbital observations of the Martian surface (*Christensen et al.*, 2001; *Putzig et al.*, 2005). The MarsWRF model uses the high resolution MOLA topography maps downsampled to the $5^\circ \times 5^\circ$ horizontal resolution of our simulations (*Smith et al.*, 2001). The current polar basal units are included for the current solar luminosity simulations. At locations where surface CO_2 ice is present, the model sets the surface albedo to 0.6 and the surface emissivity to 0.8. No subsurface (i.e., regolith) storage of CO_2 is considered, making our total CO_2 budget equal to the atmosphere plus cap amounts. Given that the regolith operates on a much slower timescale than the GCM, it is not an important part of the active climate system for our purposes and its role is implicitly accounted for in the total CO_2 inventory.

The total available CO_2 budget is a model input parameter. Each simulation has a total CO_2 inventory that corresponds to the equivalent mean surface pressure that the simulation would have if all of the CO_2 was atmospheric. We chose the range of CO_2 inventories (6 mb, 60 mb, 300 mb, 600 mb, 1200 mb, and 3000 mb) to sample the range of possible paleoclimate CO_2 inventories.

To definitively address whether poleward atmospheric heat transport can, alone, stave-

off collapse, the 0° obliquity simulations are the most illuminating. In this situation, solar heating near the poles tends to zero, and condensation cannot be prevented in the absence of transport, regardless of the atmospheric thickness and greenhouse effect. Under the constraints of this experiment, we want to answer the questions: Does the tendency for the atmosphere to collapse change as a function of atmospheric mass?

The obliquity influences the collapse criteria for the atmosphere (*Haberle et al.*, 1994; *Manning et al.*, 2006) by changing the distribution of incident solar radiation. For the zero obliquity simulations, the absence of obliquity simplified the system to one in which the only independent variable was initial atmospheric mass. With obliquity added as an independent variable, however, we specifically, we ask: How important is obliquity in the development and maintenance of permanent CO_2 ice caps?

3.3 Results for the current solar luminosity

The rate and location of CO_2 ice deposition are diagnostic of the polar energy balance that controls atmospheric collapse. Figures 3.2 and 3.3 show the evolution of various atmospheres with different initial total CO_2 and the indicated obliquity, ε, and eccentricity, e. The simulations include total CO_2 inventories of 6 mbar, 60 mbar, 300 mbar, 600 mbar, 1200 mbar, and 3000 mbar. These simulations were run with the current solar luminosity. The fraction of global CO_2 ice to the total global CO_2 in the simulation is plotted as a function of time. As CO_2 ice is deposited in the polar regions, the CO_2 ice fraction increases.

In all scenarios there is an initial period of rapid deposition of CO_2 ice as the surface

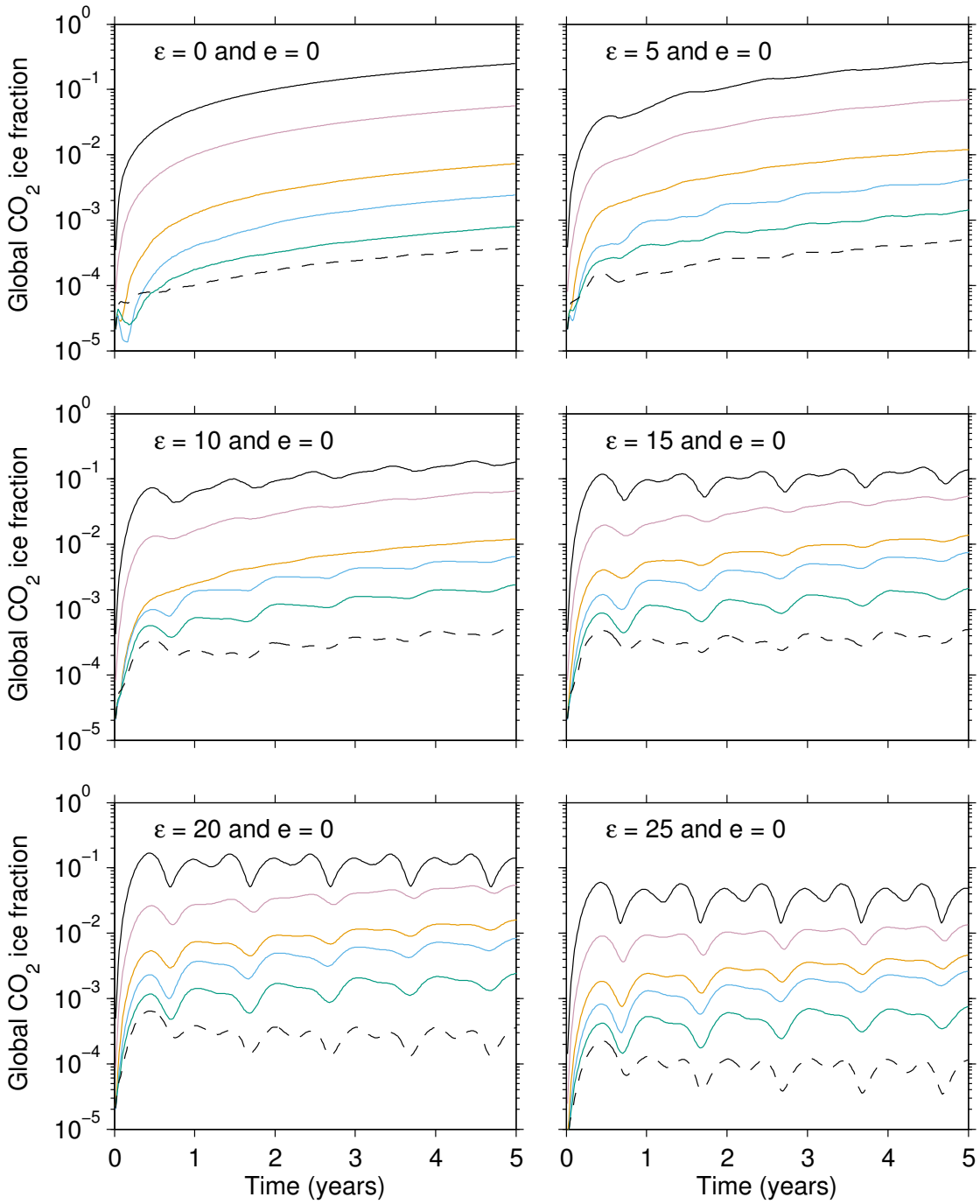

Figure 3.2: Global accumulation of CO_2 ice for the various pressures at the indicated obliquity and eccentricity for current solar luminosity. The global CO_2 ice fraction is calculated as the ratio of the global sum of CO_2 surface ice to the total available CO_2. In all figures, each line represents a different initial CO_2 inventory, as follows: solid black = 6 mbar, light red = 60 mbar, orange = 300 mbar, blue = 600 mbar, green = 1200 mbar, and dashed black = 3000 mbar.

energy balance equilibrates with the atmosphere, as seen Figures 3.2 and 3.3. After the initial half a year, all of the simulations appear to settle into a steady pattern of either continuous collapse or seasonal exchange between the atmosphere and surface. In the zero obliquity ($\varepsilon = 0°$) simulations, all of the simulations are collapsing. There are no seasons in these simulations since obliquity and eccentricity are zero. As the obliquity increases in each successive plot in Figure 3.2 a seasonal CO_2 ice cycle is convolved with the secular trend due to collapse. By $\varepsilon = 15°$ the seasonal cycle shows the semi-annual asymmetry that is due to the Martian dichotomy and similar to pressure changes measured by the Viking landers (*Hess et al.*, 1980). Note that the seasonal cycle in these simulations do not match the cycle seen in the Viking pressure curves, see for example *Hess et al.* (1980), since we have set eccentricity to zero.

Even at current solar luminosity and even for thick atmospheres, meridional heat transport is insufficient to completely stop atmosphere collapse for obliquities less than and equal to $\varepsilon = 15°$, as shown in Figure 3.2. Instead, collapse is merely slowed. Although the 6 mb and 3 bar simulations at $\varepsilon = 15°$ appear to have stopped collapsing, they still have a shallow slope commensurate with collapse (see Figure 3.21 in Appendix 3.A). In each of these twenty-four simulations global CO_2 ice accumulation continues to grow with time, as the atmosphere slowly condenses onto the polar surface. At $\varepsilon = 20°$, however, two of the simulations cease to collapse: the 6 mb simulation and the 3000 mbar simulation. In both of these $20°$ obliquity simulations, the atmosphere quickly achieves a state in which a fraction of the atmosphere exists as CO_2 ice on the surface, but there is no net annual increase in the accumulation of CO_2 ice. For the 6 mb simulation, the ice fraction

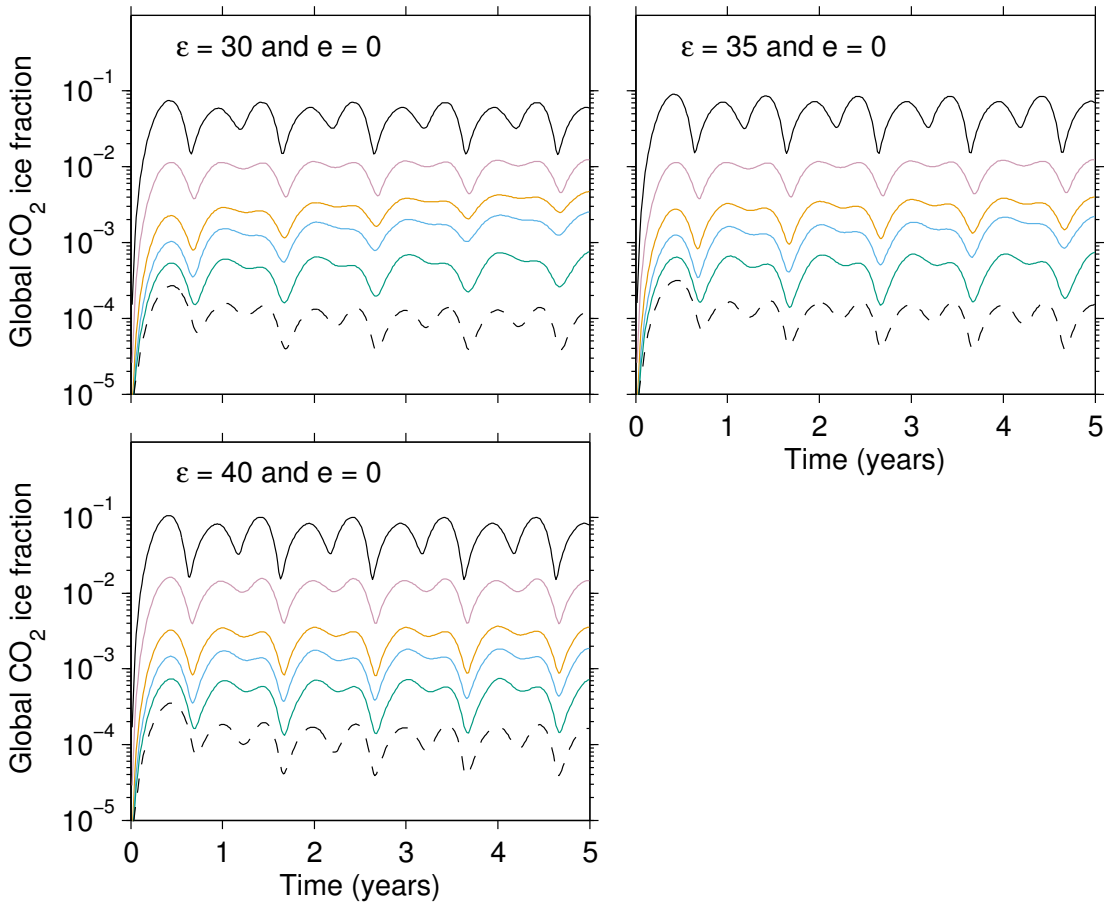

Figure 3.3: Global accumulation of CO_2 ice for the various pressures at the indicated obliquity and eccentricity for current solar luminosity. The global CO_2 ice fraction is calculated as the ratio of the global sum of CO_2 surface ice to the total available CO_2. In all figures, each line represents a different initial CO_2 inventory, as follows: solid black = 6 mbar, light red = 60 mbar, orange = 300 mbar, blue = 600 mbar, green = 1200 mbar, and dashed black = 3000 mbar.

stabilizes to around $\sim 10^{-1}$, and for the 3000 mbar simulation the ice fraction stabilizes to $\sim 10^{-4}$, while the rest of the 20° obliquity simulations are still slowly collapsing. At higher obliquities, the mid-range atmospheric thicknesses continue to collapse while the thickest and thinnest atmosphere nor longer increase in ice fraction (Figure 3.3). Finally, all of the 40° obliquity simulations are not collapsing, but instead display seasonal ice caps. By this obliquity, there is enough insolation and heat transport to stave off the collapse of the atmosphere.

The zonal mean of surface CO_2 ice as a function of time shows the evolution of the CO_2 ice on the surface of Mars, as seen in Figures 3.4 through 3.11. In each figure, the zonal mean of the CO_2 ice is plotted against time for a total of five years. The plots capture both the seasonal surface deposition of CO_2 ice and the secular growth in CO_2 ice depth. As well, the influence of topography on the CO_2 ice deposition is apparent in Figures 3.4 through 3.11.

In Figure 3.4, which shows the zonal CO_2 ice versus time for $\varepsilon = 0^{\circ}$, the CO_2 ice deposits preferentially on the north pole (although at low CO_2 inventories CO_2 ice deposits at both poles). This occurs because the topographically lower north pole has a higher surface pressure than the south pole which leads to a higher condensation temperature at the north pole. Generally, the north polar region of Mars should be more favorable to CO_2 condensation due to the relationship between pressure and condensation temperature (i.e., the Clausius-Clapeyron relation for CO_2 (*Glasser*, 2002)). The current Martian atmosphere, however, has a perennial CO_2 polar cap at the south pole and only a seasonal CO_2 cap at the north pole (*Kieffer et al.*, 1977; *Kieffer*, 1979). Various mechanisms have been pro-

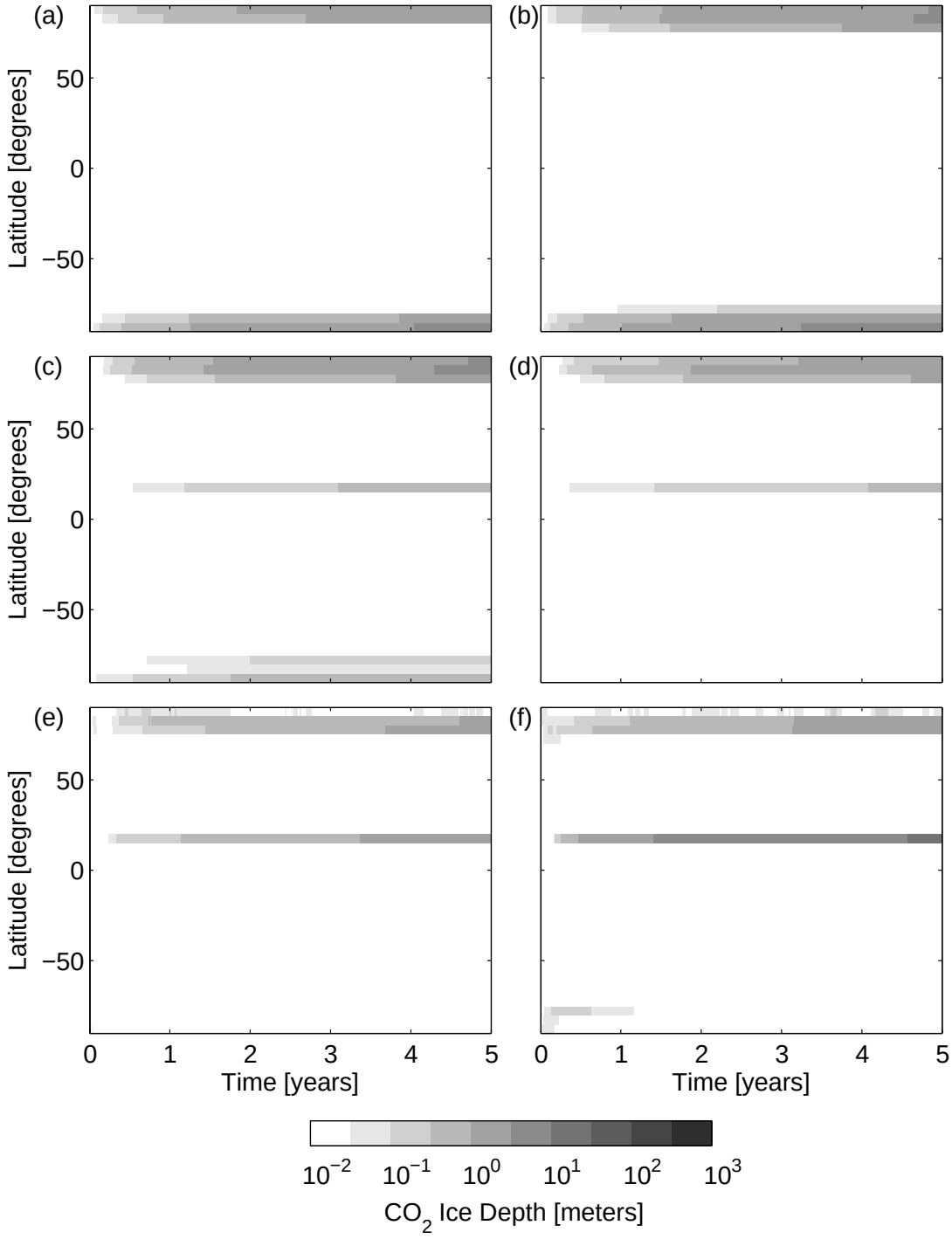

Figure 3.4: Zonal CO_2 ice versus time for the current luminosity and the 0° obliquity. The plots include the following initial surface pressures: (a) 6 mb, (b) 60 mb, (c) 300 mb, (d) 600 mb, (e) 1200 mb, and (f) 3000 mb. The plots show the thickness of CO_2 ice assuming an ice density of 1600 kg/m^3.

posed to explain this unexpected south polar preference for perennial CO_2 ice, including dust mixing with ice (*Toon et al.*, 1980) and insolation dependent ice albedo changes (*Wood and Paige*, 1992). We are neglecting dust in our model and since our CO_2 ice albedo value is constant with respect to insolation our simulations will not correctly capture this south polar phenomena. Since this phenomena is not well understood, nor normally included in Martian GCMs (*Guo et al.*, 2010), we believe that our no dust and constant albedo assumptions are justified for a first look at the climate dynamics of a collapsing CO_2 atmosphere.

As the $\varepsilon = 0^\circ$ simulations in Figure 3.4 increase in inventory, from 6 mb to 3000 mb, there are two obvious shifts in the distribution of surface CO_2 ice. First, as mean global surface pressure increases, the south polar CO_2 ice cap disappears. By the 600 mb simulation, shown in Figure 3.4(d), the southern perennial CO_2 ice cap no longer forms. For this larger CO_2 inventories, the increased greenhouse warming due to the increased CO_2 column mass and/or increased atmospheric transport outstrips the increasing condensation temperature due to increasing surface surface pressure. Essentially, the temperature set by surface pressure dependent greenhouse/advective heating is greater than the condensation temperature provided by the Clausius-Clapeyron relation[2]. The second shift in CO_2 ice distribution is the deposition of CO_2 ice on the slopes of Olympus Mons, which is captured in the MarsWRF model by a single horizontal grid point. As seen in Figures 3.4(c) to 3.4(f), CO_2 ice forms on this high elevation region at higher surface pressure. We do not include this CO_2 ice deposition on Olympus Mons in the collapse curves in Figure 3.2 nor in the

[2]The Clausius-Clapeyron relation describes the phase boundary on a phase diagram for a single component system, and thus for our specific application, the Clausius-Clapeyron relation describes the pressure dependence of the condensation (sublimation) temperature(*Bohren and Albrecht*, 1998). For CO_2 pressures that may have occurred on Mars, the Clausius-Clapeyron relation can be used to calculate a condensation (sublimation) curve on the CO_2 pressure-temperature phase diagram.

collapse timescales shown in Table 3.1 since the entire atmosphere can not be sustainably collapsed onto this single grid point in the model. Basal melting and ice flow would deliver the CO_2 ice on Olympus Mons to lower elevations where the CO_2 ice is not stable and therefore would sublimate back into the atmosphere.

Figures 3.4(e) and 3.4(f) show another change in CO_2 ice deposition as the CO_2 inventory increases: the northernmost latitude bins of the simulation are not accumulating CO_2 ice, unlike the few latitude bins immediately adjacent to the south. The difference in topography between the northernmost latitudes and the adjacent latitudes is large enough to create this difference in CO_2 ice deposition. At the $5^\circ \times 5^\circ$ resolution of the model, the north polar basal unit is roughly 2000 meters higher in elevation, on average, than the lowest points in the northern lowlands (in the model the northernmost latitude bin is centered at 87.5° North and the lowest points of the lowlands are generally along the 77.5° latitudinal circle). At the higher CO_2 inventories, i.e., 1200 mb and 3000 mb, this difference in elevation is sufficient to change the stable phase of CO_2 ice from solid to gas when going from low elevation to high elevation.

As the obliquity of the simulations is increased, a few features of the CO_2 ice deposition change. First, the ice-line of the perennial caps moves equatorward. In Figure 3.5(a) the zonal mean ice line of the north pole reaches 75° N after five Mars years whereas in Figure 3.4(a) the zonal mean ice line of the south pole extends southward only to 80°. The extended ice line occurs in all of the $\varepsilon = 5^\circ$ simulations. The second feature is the appearance of a seasonal deposition of CO_2 ice. Due to the increasing obliquity, the latitudinal extent of the polar winter increases, which leads to a larger region of CO_2 ice deposition

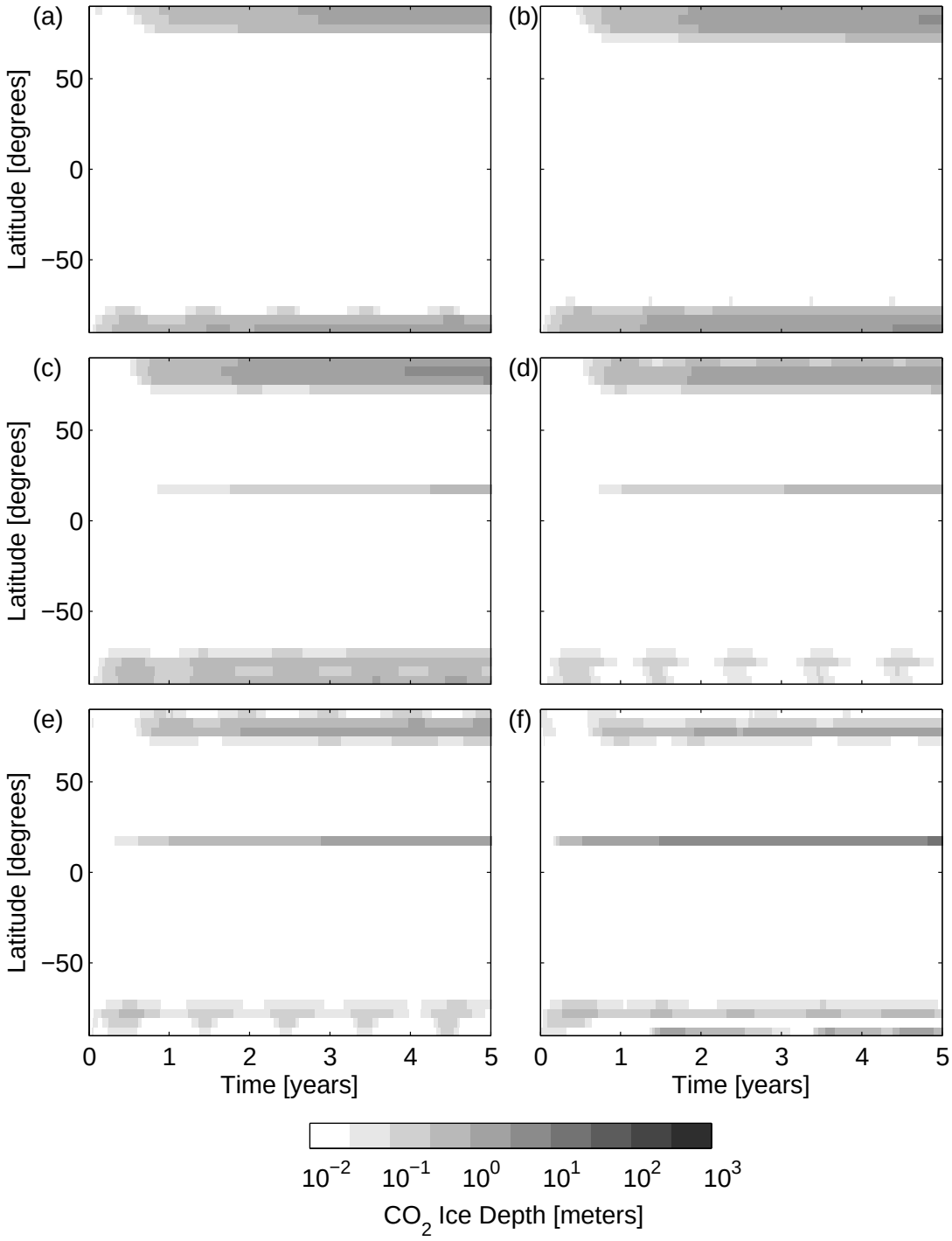

Figure 3.5: Same as Figure 3.4 but for 5° obliquity at the current luminosity.

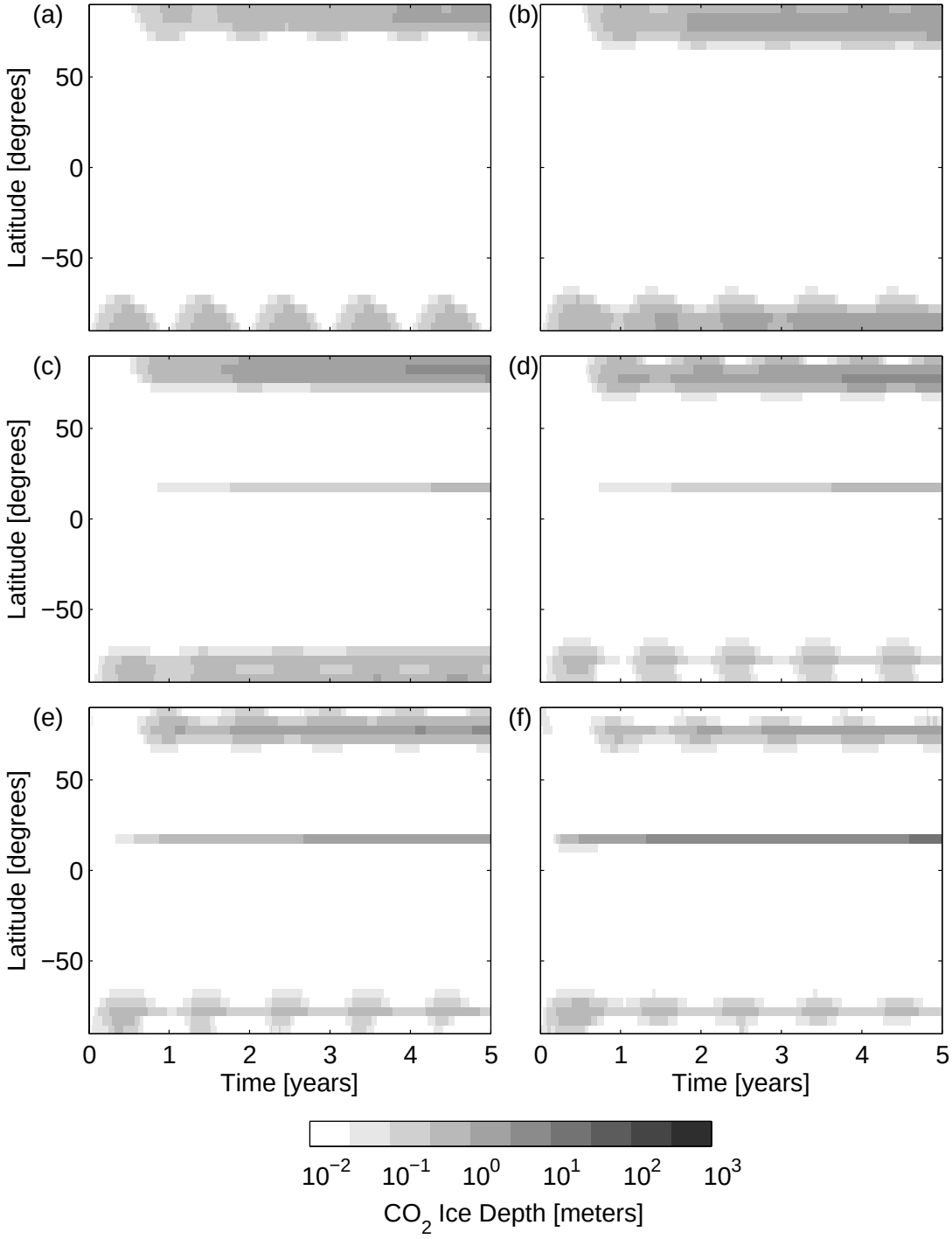

Figure 3.6: Same as Figure 3.4 but for 10° obliquity at the current luminosity.

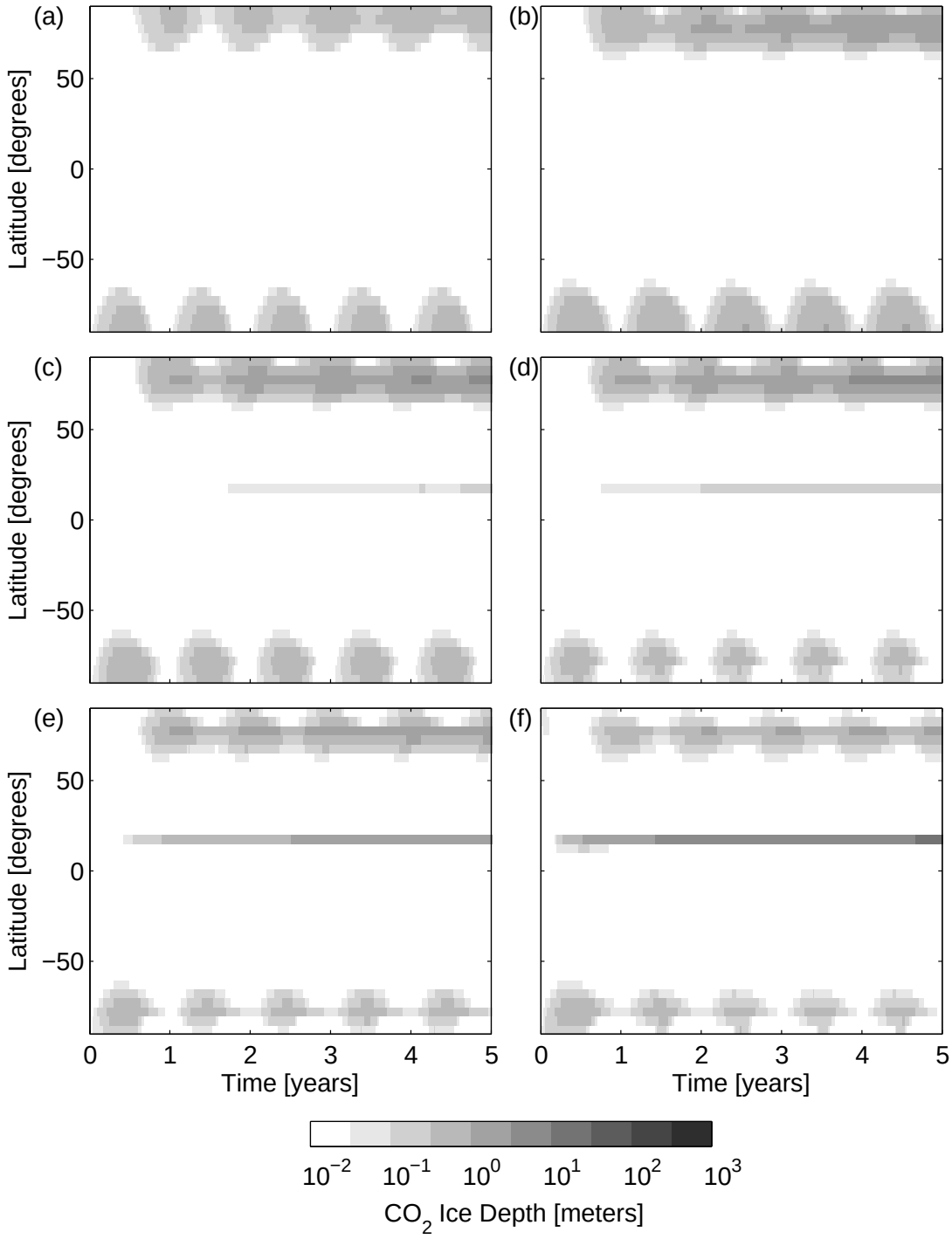

Figure 3.7: Same as Figure 3.4 but for 15° obliquity at the current luminosity.

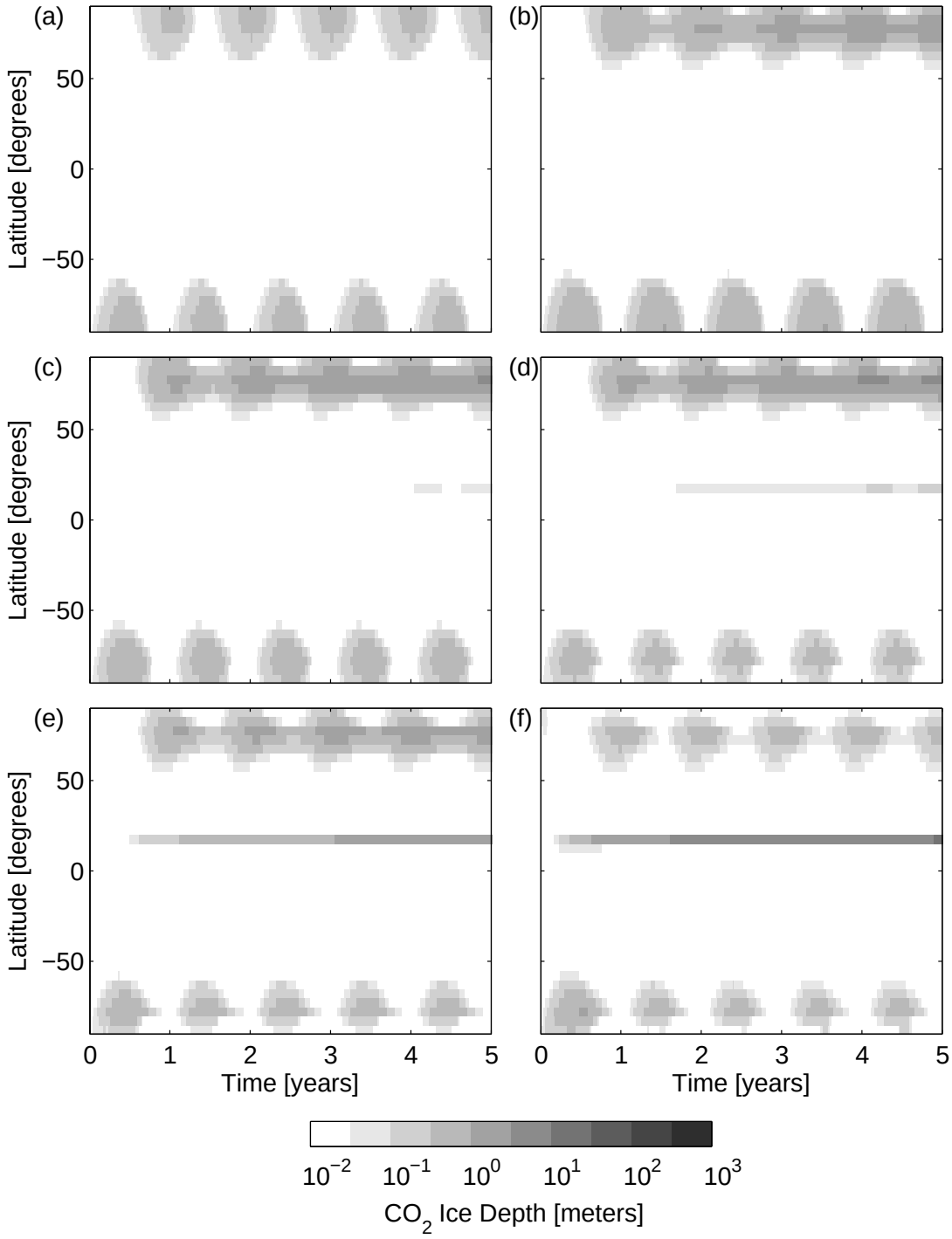

Figure 3.8: Same as Figure 3.4 but for 20° obliquity at the current luminosity.

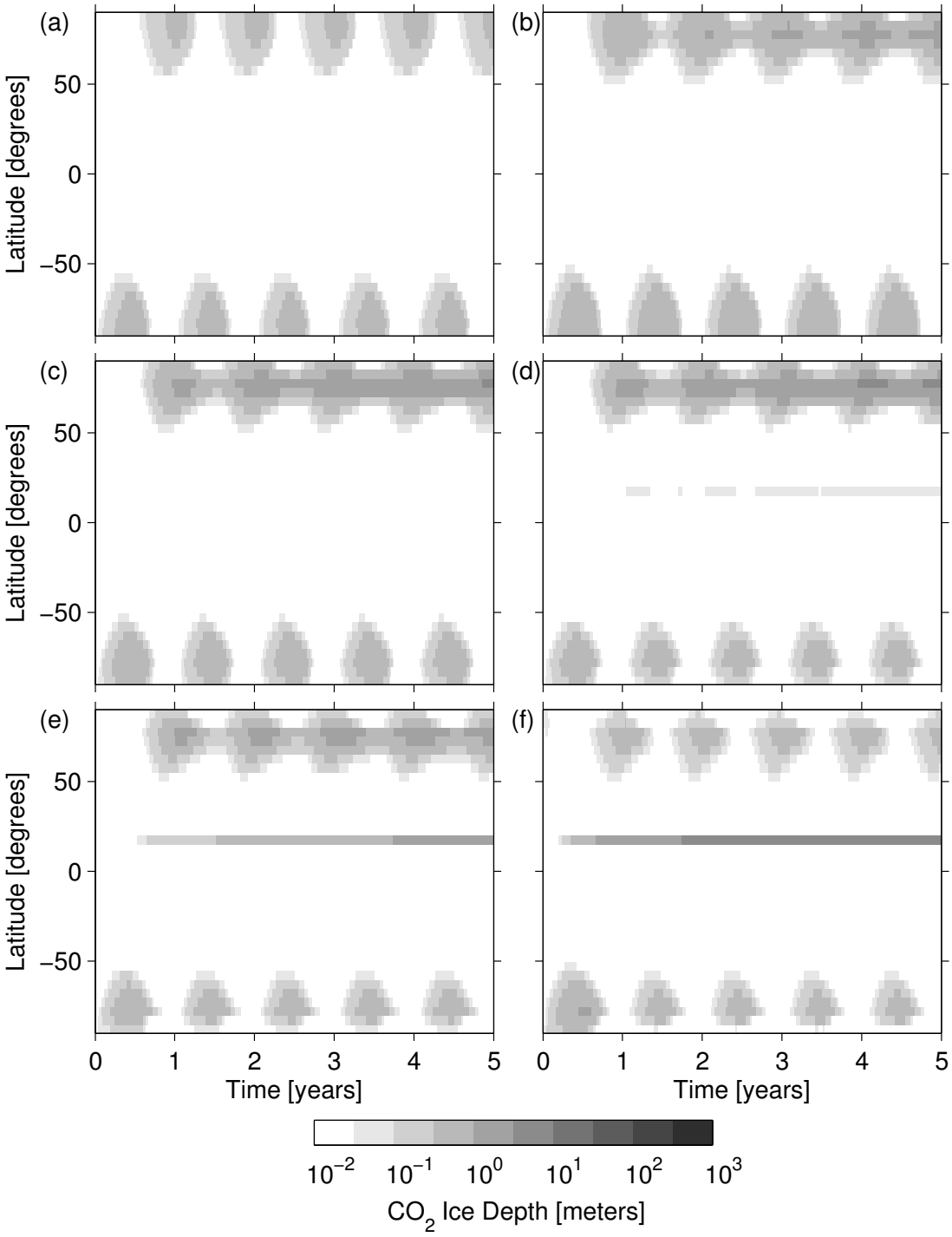

Figure 3.9: Same as Figure 3.4 but for 25° obliquity at the current luminosity.

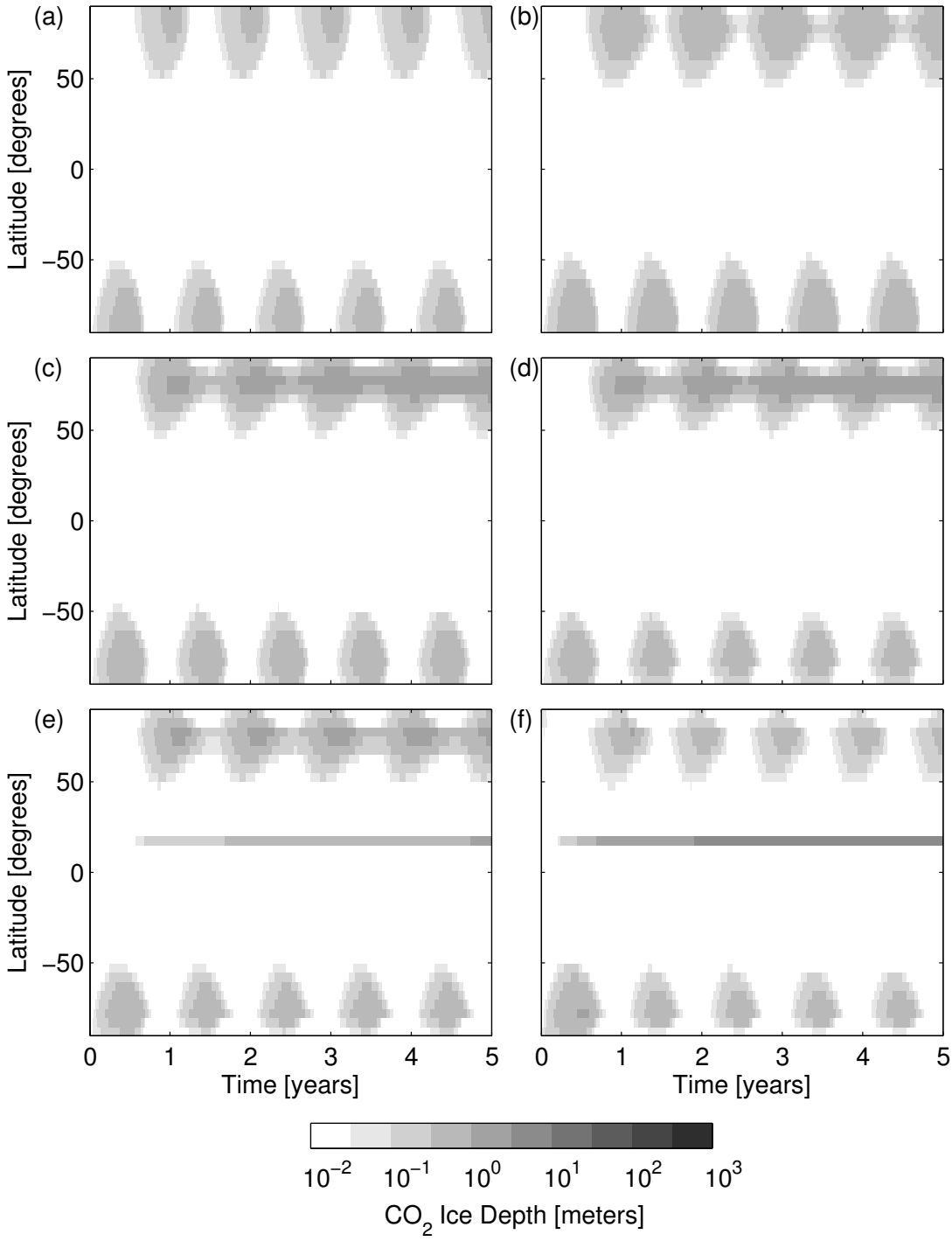

Figure 3.10: Same as Figure 3.4 but for 30° obliquity at the current luminosity.

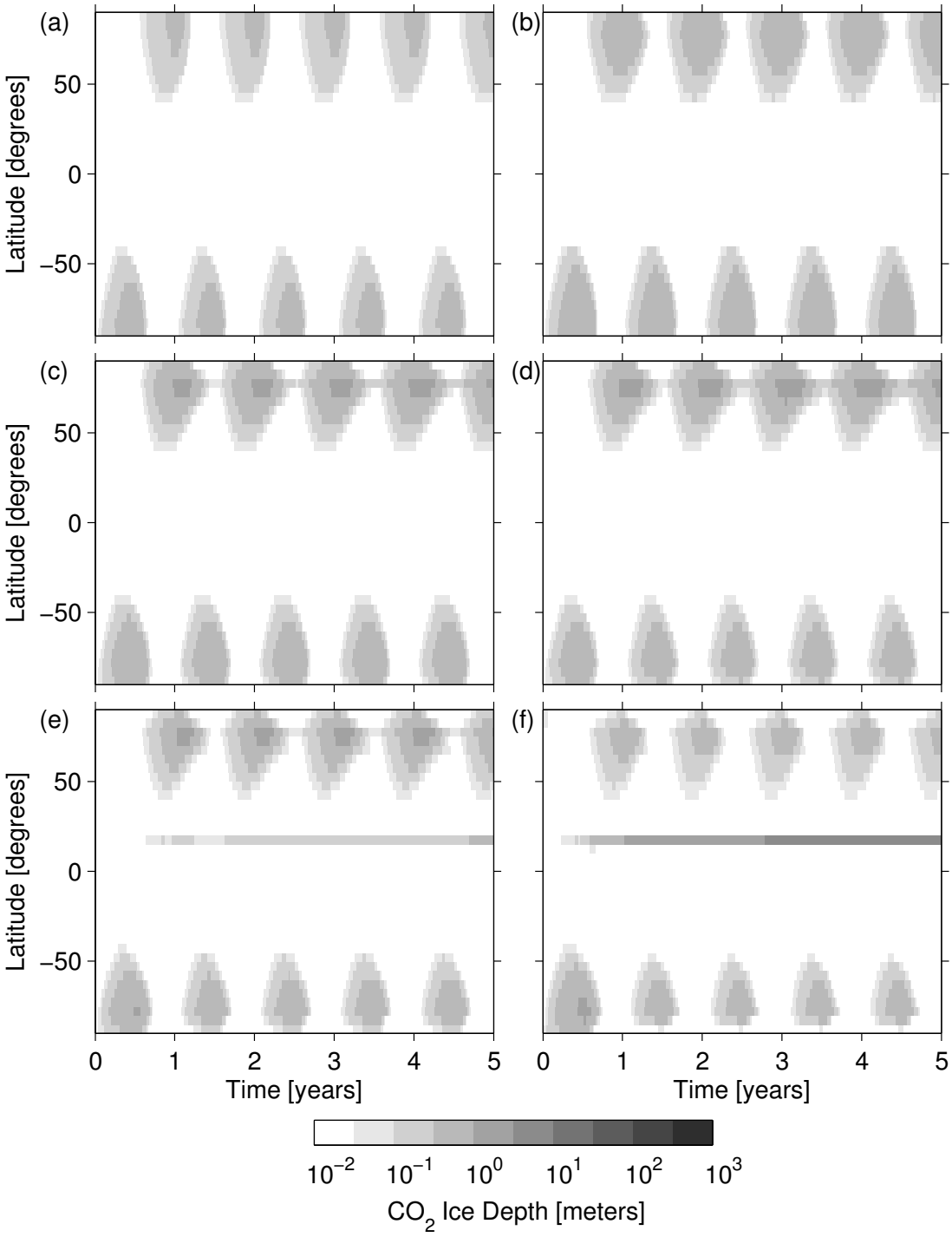

Figure 3.11: Same as Figure 3.4 but for 40° obliquity at the current luminosity.

during the winter season. The seasonal CO_2 ice extends only a small additional amount in the $\varepsilon = 5^\circ$ simulations but becomes a much stronger signal at higher obliquities, as seen in Figures 3.5 to 3.11. This seasonal CO_2 ice leads to the third feature in the higher obliquity simulations: at higher obliquity the higher CO_2 inventory simulations accumulate CO_2 ice at the south polar region. Figures 3.5(d), 3.5(e), and 3.5(f) show seasonal and perennial ice in the southern regions, whereas in Figure 3.4 there was no south polar CO_2 ice at these CO_2 inventories. These southern ice deposits are largely seasonal, with a tenuous southern perennial cap in Figure 3.5(f). For all inventories in Figure 3.5, the energy balance in the north polar region controls the atmospheric collapse. Both Figure 3.6 and Figure 3.7 show a continuation of these trends. The seasonal CO_2 ice cycle continues to dominate the ice deposition locations while the equatorward extent of the seasonal CO_2 ice increases.

The 20° obliquity simulations show a significant transition in the CO_2 ice deposition, as shown in Figure 3.8. First, the 6 mb and 3000 mb simulations are no longer collapsing. These two simulations have seasonal CO_2 caps at both poles, but no ice remains during the summer months. This is consistent with the collapse curves show in Figure 3.2. Second, none of the collapsing simulations, shown in Figures 3.8(b) through 3.8(e), have perennial CO_2 ice in the southern hemisphere. Instead, the south pole only experiences a seasonal CO_2 ice cap. Again, deposition of CO_2 ice on the north pole controls the collapse of the atmosphere.

The higher obliquities continue the pattern established in the 20° obliquity. The thinnest and thickest atmosphere are stable with respect to CO_2 condensation, with only seasonal CO_2 ice caps appearing in the 6 mb and 3000 mb simulations in Figures 3.9 to 3.10. The

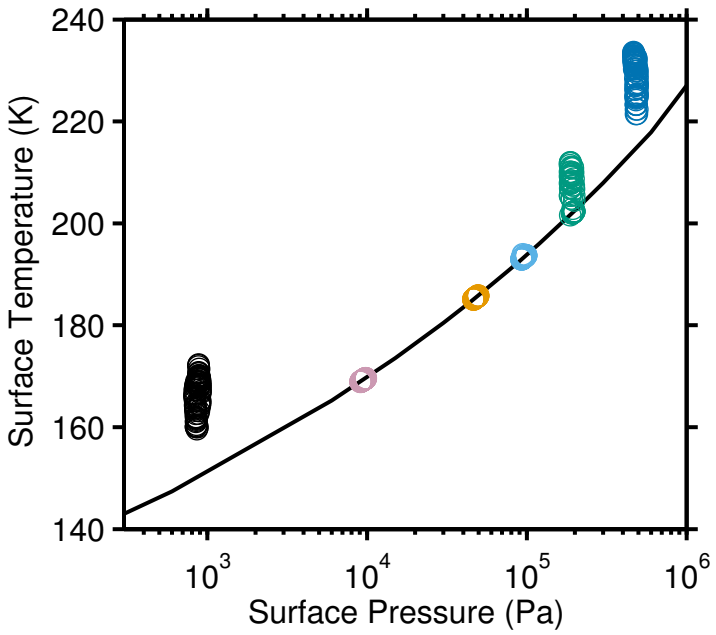

Figure 3.12: Annual mean surface temperature versus annual mean surface pressure for each longitude point along the 77.5° N latitude for $\varepsilon = 25°$. The black circles are for the 6 mb simulation, the light red circles are for the 60 mb simulation, the orange circles are for the 300 mb simulation, the light blue circles are for the 600 mb simulation, the green circles are for the 1200 mb simulation, and the dark blue circles are for the 3000 mb simulation. The solid black line is the condensation curve for CO_2 .

collapsing atmospheres (60 mb, 300 mb, 600 mb, and 1200 mb) are increasingly dominated by their seasonal cycles, and their collapse rate becomes slower with increasing obliquity (Table 3.1). The slower collapse rates, however, are still sufficiently fast that these atmospheres would completely collapse within a 120,000 year obliquity cycle.

We can understand the response of CO_2 condensation to the various global mean surface pressures in Figure 3.9 by comparing our results to the Gierasch-Toon-McKay model (hereafter GTM) for the balance between condensation and sublimation (*Gierasch and Toon*, 1973; *McKay et al.*, 1991). Should the relationship between the condensation curve and the atmospheric heating by advection and greenhouse warming be as predicted by the GTM

model, the annual mean polar temperatures in our simulations should lie on the sublimation curve for collapsing simulations and lie above the sublimation curve for non-collapsing simulations. The $\varepsilon = 25^\circ$ simulations provided the perfect case to test this hypothesis, since both ends of the simulated pressure range involved non-collapsing simulations (see Figure 3.9). The northern hemisphere of the $\varepsilon = 25^\circ$ simulations have permanent CO_2 ice caps for the 60 mb, 300 mb, 600 mb, and 1200 mb simulations. The 6 mb and 3000 mb simulations have only seasonal CO_2 ice caps in the northern hemisphere. Therefore, we plotted the annual mean surface temperature at each longitude along the 77.5° N latitude for each simulation on a surface pressure vs. surface temperature space, as shown in Figure 3.12. We used the last year of the five year simulations shown in Figure 3.9. The polar temperatures follow the condensation curve in exactly the manner predicted by *McKay et al.* (1991) and *Haberle et al.* (1994). The collapsing simulations lie on the condensation curve, as they are constrained by the condensation temperature, and are unable to cool nor are they being warmed by advective and greenhouse heating. On the other hand, the non-collapsing simulations, i.e., the 6 mb and 3000 mb simulations, follow the advective and greenhouse heating to temperatures higher than the condensation temperature. The 1200 mb simulation, shown as green circles in Figure 3.12 represents a simulation in transition. Some longitudes of the 1200 mb simulation no longer have permanent CO_2 ice, and thus these longitudes appear in Figure 3.12 as green circles that lie above the CO_2 condensation curve. For other longitudes, perennial CO_2 ice still remains at the surface. These longitude then appear in Figure 3.12 as green circles lying on top of the condensation curve. Wherever there is perennial CO_2 ice, the temperature of the ice covered surface is fixed to the

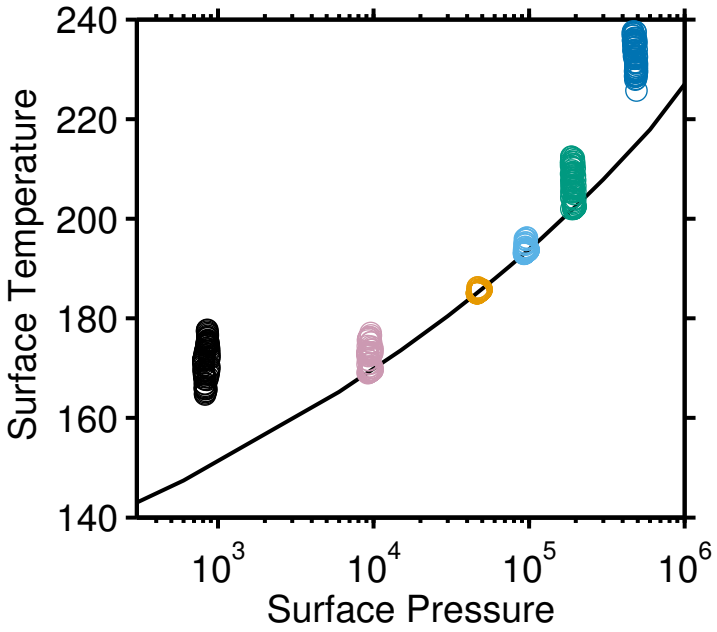

Figure 3.13: Annual mean surface temperature versus annual mean surface pressure for each longitude point along the 77.5° N latitude for $\varepsilon = 30°$. The black circles are for the 6 mb simulation, the light red circles are for the 60 mb simulation, the orange circles are for the 300 mb simulation, the light blue circles are for the 600 mb simulation, the green circles are for the 1200 mb simulation, and the dark blue circles are for the 3000 mb simulation. The solid black line is the condensation curve for CO_2 .

condensation temperature.

For the $\varepsilon = 30°$ simulations, the 60 mb simulation begins to 'move' off the condensation curve, as seen in Figure 3.13. This change corresponds to the thinning of the northern perennial cap seen in Figure 3.10. Collapse is still occurring in the 60 mb simulation, but the surface area that controls the collapse is smaller in this higher obliquity. At each successively higher obliquity, the same process is seen: the non-collapsing simulations have warm polar temperatures that lie above the condensation curve because the higher obliquity delivers a higher annual mean insolation at the poles. For the collapsing simulations, with each successively higher obliquity the polar area that accumulates CO_2 ice becomes

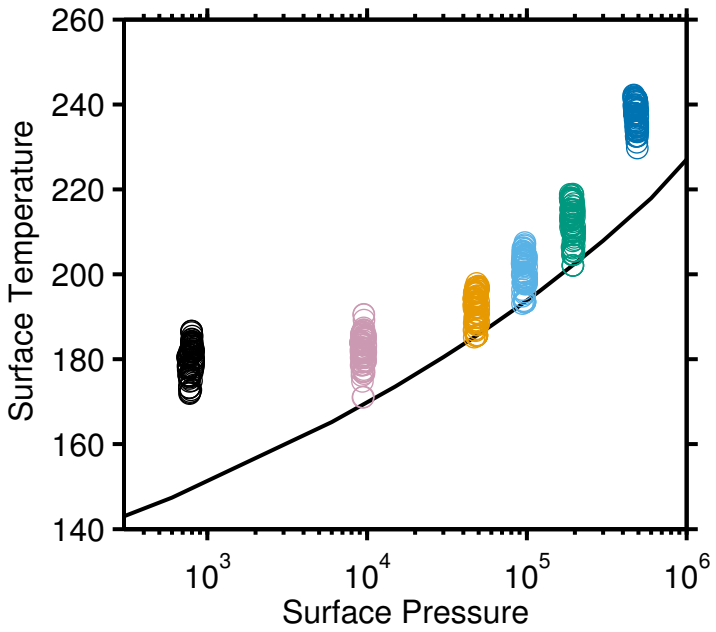

Figure 3.14: Annual mean surface temperature versus annual mean surface pressure for each longitude point along the 77.5° N latitude for $\varepsilon = 40°$. The black circles are for the 6 mb simulation, the light red circles are for the 60 mb simulation, the orange circles are for the 300 mb simulation, the light blue circles are for the 600 mb simulation, the green circles are for the 1200 mb simulation, and the dark blue circles are for the 3000 mb simulation. The solid black line is the condensation curve for CO_2 .

smaller, thus restricting the rate of atmospheric collapse. By $\varepsilon = 40°$, almost all of the simulations have stopped collapsing and thus the polar surface temperatures have almost entirely moved off the condensation curve. In Figure 3.14 only one or two locations along the 77.5° N latitude ring, in the 300 mb, 600 mb, and 1200 mb simulations, still lie on the condensation curve. Very little polar area is covered in CO_2 ice and the atmospheric collapse is almost completely stifled, which is consistent with the zonal mean accumulation of CO_2 ice shown in Figure 3.11. The 60 mb simulation is completely CO_2 ice free and the polar surface temperatures for the 60 mb simulation lie above the condensation curve.

If we look at the lower obliquity simulations, the process is reversed. More of the

simulations lie closer or on the condensation curve. The lower the obliquity, the closer to the condensation curve are the surface temperatures in the north polar area. For the zero obliquity simulations, all of the polar surface temperatures lie on the condensation curve, as shown in Figure 3.15. (Note that since the CO_2 deposits are more latitudinally confined in the lower obliquity simulations, as previously mentioned, the data in Figure 3.15 are from the 82.5° N latitudinal ring.) It is not clear from this figure if there still exist either extremely low or extremely high surface pressures for which the polar surface temperature is greater than the local condensation temperature. This becomes important at the low pressure range, particularly in regards to the end stages of atmospheric collapse. When the climates simulated in the zero obliquity case reach CO_2 ice fractions approaching 1, i.e., when the majority of the CO_2 in the system is on the surface of Mars, the Martian atmosphere will become very thin. Will the atmosphere stop collapsing at some small pressure? Or will the collapse continue until the only atmospheric constituents are the non-condensable gases, argon and nitrogen? Our results imply that there should be a non-zero low atmospheric pressure for which atmospheric collapse stops, but such a state is not directly visible in the data from our simulations.

At the higher obliquities, the energy balance in the Olympus Mons region is also changing. Starting with the 0° obliquity simulations (Figure 3.4), CO_2 ice accumulates on the Olympus Mons slopes for global mean surface pressures of 300 mb and higher. This continues until $\varepsilon = 20°$, beyond which CO_2 no longer deposits onto Oympus Mons at 300 mb, though it continues to do so for 600 mb, 1200 mb, and 3000 mb (Figure 3.8). By $\varepsilon = 30°$, the CO_2 ice stops condensing onto Olympus Mons in the 600 mb simulation (Figure 3.10),

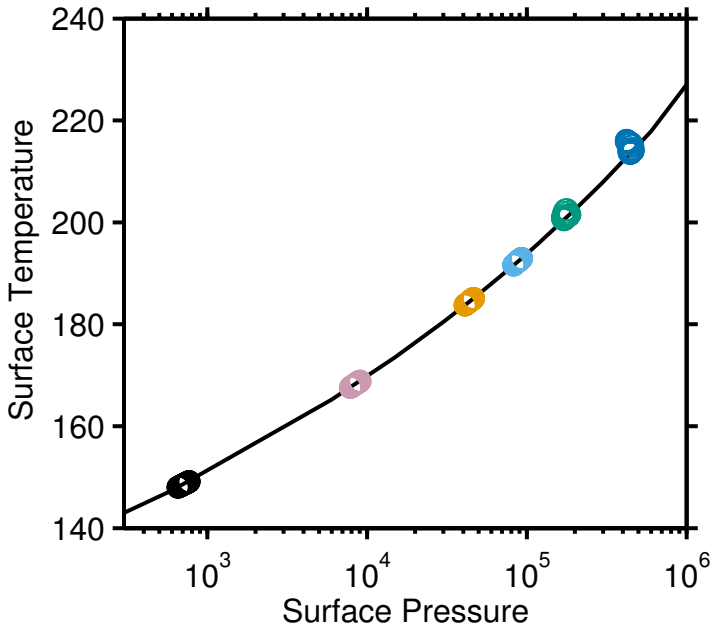

Figure 3.15: Annual mean surface temperature versus annual mean surface pressure for each longitude point along the 82.5° N latitude for $\varepsilon = 0°$. The black circles are for the 6 mb simulation, the light red circles are for the 60 mb simulation, the orange circles are for the 300 mb simulation, the light blue circles are for the 600 mb simulation, the green circles are for the 1200 mb simulation, and the dark blue circles are for the 3000 mb simulation. The solid black line is the condensation curve for CO_2 .

and only the 1200 mb and 3000 mb simulations still have CO_2 snows on Olympus Mons at $\varepsilon = 45°$. This change as a function of obliquity of the CO_2 ice on Olympus Mons is due to the competition of increasing insolation at the latitude of Olympus Mons and the surface pressure at Olympus Mons. Although the increased surface pressure of the thicker atmospheres leads to a higher condensation temperature of CO_2 , for the 300 mb and 600 mb simulations, this increased condensation temperature is eventually overwhelmed by the increased insolation at the Olympus Mons latitude. For the 1200 mb and 3000 mb simulations, the CO_2 condensation temperature at Olympus Mons has become so high that even the higher insolations of $\varepsilon = 40°$ and $\varepsilon = 45°$ are insufficient to prevent condensation of CO_2 .

To understand how the Martian climate history is affected by atmospheric collapse and orbital variations, we look at the time required for all of the atmospheric CO_2 to condense onto the surface, i.e., the time to completely collapse the CO_2 atmospheres. Timescales for complete collapse, i.e., collapse timescale, were calculated for all of the simulations (for details on the calculations, see Section 3.A). Table 3.1 lists the collapse timescale, in years, for the $\varepsilon = 0°$ to $\varepsilon = 35°$ simulations. There are no timescales for the 6 mb and 3000 mb simulations for $\varepsilon = 20°$ through $\varepsilon = 40°$ and the 60 mb simulation for $\varepsilon = 40°$, since those simulations are not collapsing. The 300 mb, 600 mb, and 1200 mb simulations for $\varepsilon = 40°$ are labeled marginal in Table 3.1. For these three simulations, the calculated timescale is negative (see Appendix 3.A) implying non-collapse, but Figure 3.11 shows that a small amount of perennial ice exists at around 77.5° N latitude. This is consistent with the distribution of polar surface temperature in Figure 3.14. For these three simulations,

	Obliquity								
$\bar{P}_s$	0°	5°	10°	15°	20°	25°	30°	35°	40°
6	20	20	30	100	NC	NC	NC	NC	NC
60	90	70	80	120	150	300	5,000		NC
300	700	400	400	500	500	500	700	2,200	marginal
600	1,900	1,200	900	900	900	900	1,300	2,100	marginal
1200	6,500	4,100	2,500	4,300	4,700	6,500	13,000	NC	marginal
3000	14,500	12,300	13,800	36,300	NC	NC	NC	NC	NC

Table 3.1: Collapse timescales, in years, for $\varepsilon = 0°$ to $\varepsilon = 40°$ for the current solar luminosity. NC = not collapsing.

the majority of longitudes in the polar region have no perennial ice, but a small number of locations have accumulated a few centimeters of CO_2 after five simulation years.

Within each group of similar initial surface pressures (6 mb to 3000 mb) the collapse timescales vary by less than an order of magnitude for the range of obliquities. For example, the 6 mb simulations have a collapse timescale ranging from 20 years to 100 years for $\varepsilon = 0°$ to $\varepsilon = 15°$. Within each obliquity, the various initial surface pressures have a similar collapse rate, as shown in Table 3.1. In fact, the rate of collapse for all of the collapsing simulations is within an order of magnitude of each other. A good approximation for the collapse rate, based on the fitted slopes in Table 3.1, is $\sim 10^{15}\ \mathrm{kg\,yr^{-1}}$. The collapse rate is controlled by the CO_2 ice surface area, which is similar to an order of magnitude between the various simulations. Neither the atmospheric thickness nor the planetary obliquity exert control on the collapse rate. Once collapse begins, CO_2 will condense at a rate of $\sim 10^{15}\ \mathrm{kg\,yr^{-1}}$ until either all of the atmospheric CO_2 has condensed or until the global mean surface pressure is low enough that the polar surface temperatures are higher than the condensation temperature. This latter lower limit on the collapse is determined by the obliquity of Mars.

All of the collapse timescales are significantly shorter than the 120,000 year period of the obliquity oscillations (*Ward*, 1974). Thus, for obliquity oscillations that dip significantly below $\varepsilon = 20°$, the Martian atmosphere would completely collapse. Such conditions occur in many of *Laskar et al.* (2004)'s obliquity calculations. Interestingly, for the middle range of global mean surface pressures, i.e., from $\sim$60 mb to $\sim$1200 mb, the Martian atmosphere would completely collapse up to $\varepsilon = 40°$, which includes a much larger portion of the likely obliquity values for Mars (*Laskar et al.*, 2004). *Laskar et al.* (2004) calculated that over 4 billion years, the mean expected obliquity is $\overline{\varepsilon} = 37.62°$ with a standard deviation of $\sigma_\varepsilon = 13.814°$. Within this range, the most probable obliquity for Mars over 4 billion years is $\varepsilon = 41.80°$ (*Laskar et al.*, 2004). Therefore, for a decent fraction of the probable range of obliquities, the atmospheres with a midrange thickness, $\sim$100 mb to $\sim$1000 mb, would have undergone collapse.

3.4 Limits on the height of CO_2 ice caps

Ultimately there is a limit to the amount of carbon dioxide ice that can be deposited at a particular point on the Martian surface. The height of an ice cap is limited by at least two processes: first, the mechanical failure of ice under its own weight, which leads to horizontal flow of the ice, and second, the basal melting due to geothermal heating and overburden pressure, which can lead to horizontal transport of CO_2 liquid. For the current Martian atmosphere, a polar cap of carbon dioxide ice can maintain a thickness of around 1800 meter for around 10^7 years before the ice mechanically fails under its own weight (*Nye et al.*, 2000). Additionally, as the CO_2 ice piles up, the base of the ice cap heats up until

the ice is converted into liquid, a process called basal melting (*Mellon*, 1996). Once basal melting begins, liquid CO_2 can flow into the subsurface thus limiting the accumulation of CO_2 ice to ~ 1200 km in the current Martian atmosphere (*Mellon*, 1996).

In order to determine order of magnitude constraints on CO_2 ice deposition, we extended the *Mellon* (1996) calculations on basal melting of CO_2 ice sheets to the range of atmospheric pressures that we have investigated. The thermal limits on polar cap height involve a balance between the increasing pressure at depth within the cap and the increasing temperature at depth within the cap. Similar to *Mellon* (1996) we calculated the pressure within the cap using the following relation:

$$P(z) = P_s + \rho g z \tag{3.1}$$

where P_s is the surface pressure at the top of the cap, ρ is the density of the CO_2 ice, g is the gravity on Mars, and z is the depth in the ice. The equilibrium temperature at depth within the polar cap is calculated using:

$$T(z) = T_s + \frac{H}{k} z \tag{3.2}$$

where T_s is the surface temperature at the top of the ice cap, H is the geothermal heat flux from below the ice cap, and k is the effective thermal conductivity of the carbon dioxide ice (*Mellon*, 1996). Like *Mellon* (1996), we use a CO_2 effective thermal conductivity of 0.5 $\mathrm{W\,m^{-1}\,K^{-1}}$ and a geothermal heat flux of 0.03 $\mathrm{W\,m^{-2}}$. For this calculation, the CO_2 ice density is $1600\,\mathrm{kg\,m^{-3}}$ (*Kieffer*, 2007). The ice cap surface temperature is the

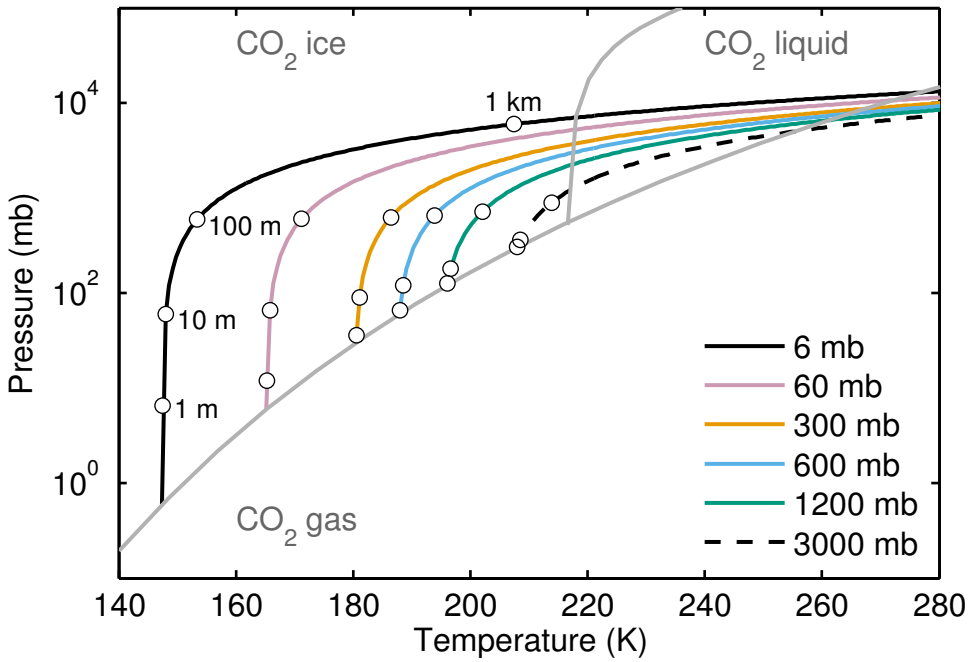

Figure 3.16: Temperature-pressure profile of a polar CO_2 ice cap compared to the CO_2 phase diagram. The grey lines are the phase boundaries for CO_2 in a single-component system. The regions of CO_2 gas, CO_2 liquid, and CO_2 ice are identified. The profiles correspond to the six different CO_2 inventories of this investigation. Each profile is marked by four depth levels: 1 meter, 10 meters, 100 meters, and 1 kilometer.

condensation temperature for the given global mean surface pressure of a simulation. For a 6 mb atmosphere the condensation temperature is $\sim$148 K; for a 3000 mb atmosphere the condensation temperature is $\sim$208 K. Figure 3.16 shows the the polar cap thickness temperature-pressure profiles for the atmospheric thicknesses of our simulations.

The results of this simple model provide some constraints to our simulation results. As seen in Figure 3.16, a cap thickness of 100s of meters is achievable for all CO_2 inventories. Thicker CO_2 ice caps are possible for the thin atmospheres, but for the thick atmospheres, particularly the 3000 mb simulation, cap thickness much greater than 100 meter quickly cross the ice-liquid phase boundary and thus CO_2 ice will begin melting at the base of the

ice deposit. Unable to sustain further CO_2 ice, the CO_2 liquid may be squeezed out of the base. As well, for CO_2 ice lying on slopes, the basal melting may facilitate flow of the CO_2 ice sheets. If the CO_2 ice does start flowing, the flow itself could double the heating at the base of the CO_2 ice sheet and accelerate the basal melting (*Mellon*, 1996). At complete collapse, the thinnest atmosphere would have ice sheet thicknesses on the order of meters to tens of meters at each polar cap. For the 600 mb simulation, the CO_2 ice sheets would be on the order of 100s of meters thick, which puts those deposits near the height associated with basal melting. The thickest atmospheres would not be able to completely collapse before basal melting occurred. Since these thick atmosphere simulations take the longest time to completely collapse, it is possible that these climate systems possess further CO_2 stability regimes where CO_2 basal melting limits further collapse and the CO_2 gas, liquid, and ice inventories achieve a sustainable balance. Determining such possible regimes is beyond the scope of this investigation and is left for future work.

Our simple replication of the work of *Mellon* (1996) omitted many complexities, including the different densities for different types of CO_2 ice, like pure CO_2 ice or CO_2 firn, the range of possible geothermal heat fluxes, and the range of possible thermal conductivity for both pure ice and ice mixtures. Our simulations using MarsWRF explored the atmospheric physics involved in the collapse of the Martian atmosphere, but further work on the physics of CO_2 ice will be required to understand the limits of atmospheric collapse.

3.5 Condensation vs. atmospheric heating

The Martian polar climate is subject to four feedbacks that affect the energy balance in the atmosphere (*McKay et al.*, 1991; *Nakamura and Tajika*, 2002). The ice-albedo feedback is a positive feedback where the deposition of ice decreases the surface temperature which leads to more ice deposition. Another positive feedback is the greenhouse effect, where the generation of additional atmospheric CO_2 , usually by subliming CO_2 ice, warms the atmosphere which leads to the generation of more atmospheric CO_2 . A third positive feedback in the polar regions is the heat transport feedback. An increase in global atmospheric mass leads to an increase in equator to pole atmospheric heat transport which sublimes surface CO_2 ice which increases the global atmospheric mass. These positive feedbacks are tempered by the condensation temperature feedback, which is a negative feedback. As atmospheric pressure increases, the condensation temperature of CO_2 increases which leads to increased CO_2 condensation that results in a reduction of the atmospheric pressure. The heat transport feedback and the greenhouse feedback work to increase the atmospheric pressure and decrease the CO_2 ice inventory while the ice-albedo feedback and the condensation temperature feedback both promote the deposition of CO_2 ice.

In the energy balance of the polar regions, these feedbacks are competing to determine the surface temperature and state. Whether an energy balance model is used or a general circulation model, correctly capturing this feedback competition is important for correctly determining the polar surface temperature and climate state. In previous work, the heat transport feedback was calculated using a diffusive term based on radiative-convective calculations (*Gierasch and Toon*, 1973; *Haberle et al.*, 1994; *Nakamura and Tajika*, 2002).

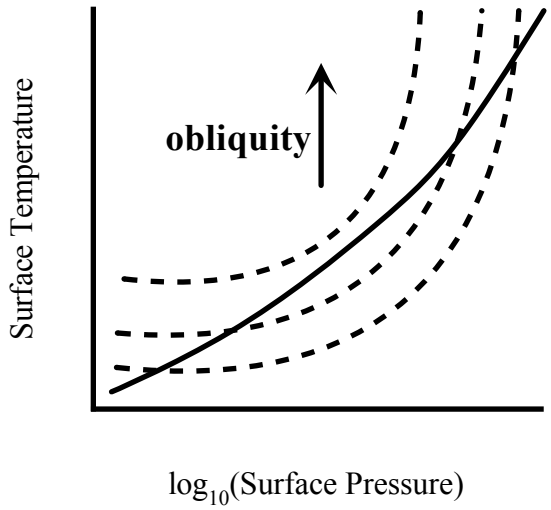

Figure 3.17: The interaction between obliquity, polar surface temperature due to atmospheric heating, and the condensation curve. The solid black line represents a condensation curve for CO_2 . The dashed black lines represent polar surface temperature due to atmospheric heating. Each dashed line represents the polar surface temperature at a given obliquity. The obliquity increases towards the top of the figure.

Our investigation leveraged the numerical solution of the primitive equations for atmospheric dynamics to more accurately simulate the heat transport into the polar regions. This has allowed us to more closely investigate the competition between the atmospheric heating feedbacks, which include the greenhouse feedback and the heat transport feedback, and the condensation temperature feedback.

The competing relationship between the condensation temperature feedback and the atmospheric heating feedback explains why the midrange global mean surface pressure simulations continue to collapse at $\varepsilon = 25°$, while the thinnest and thickest atmospheres have ceased collapsing. The two nonlinear effects swap dominance more than once over the range of atmospheric pressures that we explored. The range of surface pressures that experience collapse is larger in our simulations than in the work of *McKay et al.* (1991) and

Haberle et al. (1994). Whereas *McKay et al.* (1991) and *Haberle et al.* (1994) found the range of global mean surface pressures that lead to atmospheric collapse to be ~5 mb to ~50 mb, our simulations have atmospheric collapse occurring between ~6 mb and ~1200 mb. Greenhouse and advective heating are actually less efficient in the GCM simulations than in the energy balance models for the middle range of global mean surface pressures. Some of this difference between our results and previous results is due to topography, which our models capture but is often left out of the energy balance models. In particular, the permanent CO_2 ice caps are primarily in the northern hemisphere due to the higher surface pressure in the northern lowlands which leads to higher condensation temperatures. When the southern hemisphere annual mean surface temperatures for -77.5° S latitude were plotted similarly to Figure 3.12, all of the southern hemisphere points lied above the condensation curves in temperature and at lower surface pressures than the northern hemisphere.

The different obliquities shift the polar surface temperature curve with respect to the condensation curve, which is shown conceptually in Figure 3.17. Higher obliquity delivers more insolation to the polar region for all surface pressures (i.e., CO_2 inventories) and thus shifts the polar temperature curve to higher temperatures. Similarly, lower obliquity shifts the curve to lower temperatures. For most of the obliquities we simulated, the position of the of the polar surface temperature curve leads to intersections with the condensation temperature curve and leads to the condensation of CO_2 as previously described. When the obliquity increases sufficiently, to $\varepsilon = 40^\circ$ in our simulations, the polar temperature curve lies completely above the condensation curve and atmospheres will not collapse at any CO_2

inventory. This transition to no collapsing atmospheres occurs because there is enough insolation in the polar region to allow the atmospheric heating feedbacks to overwhelm the condensation temperature feedback.

3.6 Conclusions

We have shown that for obliquities less than 20° perennial CO_2 ice will form for all inventories, up to 3000 mb. Even thick atmospheres are insufficient to stave off the collapse of the atmosphere. The distribution of the perennial ice is dependent on both the condensation temperature of CO_2 at the surface and the combination of the greenhouse effect of the atmosphere and the meridional advection of heat in the atmosphere. In fact, these processes compete to determine where and at what elevation the CO_2 ice accumulates. Regardless of the distribution of the CO_2 ice, the timescale for deposition is much longer than that produced by a 1-D model.

For the lower obliquities, the tendency for the atmosphere to collapse is not a function of the atmospheric mass. At all CO_2 inventories at least one polar cap is collapsing. What is controlled by the atmospheric mass in the lower obliquity simulation is the condensation of CO_2 in the southern hemisphere, i.e., higher elevations. At the low obliquities, the thicker atmospheres provide enough heating to prevent perennial ice from forming in the southern hemisphere. However, for the higher obliquity simulations, the collapse tendency varies with atmospheric mass. The lowest mass atmospheres and the the highest mass atmospheres do not collapse. The midrange atmospheric masses continue to experience collapse and deposition of polar CO_2 ice up to an obliquity of 40°.

A much stronger control on the tendency to collapse is the obliquity. The interaction of the polar surface temperature with the condensation temperature is strongly controlled by the distribution of insolation, which in turn is controlled by the obliquity of the planet. For low obliquities, the polar temperature due to the atmosphere is less than the condensation temperature for all CO_2 inventories simulated. The increasing obliquity increases the polar temperature. Due to the pressure-temperature nature of the polar temperature, the low and high atmospheric thickness simulations are the first to warm enough to have polar surface temperatures greater than the condensation temperature. Higher obliquities continue to control the relationship between the polar surface temperature and the condensation temperature, and therefore the tendency of the atmosphere to collapse.

The results of our simulations match the polar surface temperature and surface pressure relationship developed by Gierasch and Toon and McKay (*Gierasch and Toon*, 1973; *McKay et al.*, 1991; *Haberle et al.*, 1994). We find, however, the middle range of atmospheric thicknesses that are collapsing is larger than seen in the previous energy balance models. Our more accurate representation of heat transport shifts the balance between competing polar feedbacks, particularly the balance between atmospheric heating and the condensation temperature. By more accurately capturing the polar energy balance we hopefully have fully captured the planetary response to atmospheric collapse conditions.

Future work will require adding to the model some important parameters that could affect our results, including atmospheric dust and orbital eccentricity. Atmospheric dust generally heats an atmosphere and thus could possibly help stave off the onset of collapse. The orbital eccentricity affects the annual cycle of insolation, and therefore could influence

the onset of collapse as well as the overprinting of the seasonal cycle of CO_2 .

3.A Collapse timescale estimates

The CO_2 ice fraction curves shown in Figures 3.2 and 3.3 were fit by linear regression with the goal of calculating a collapse timescale for each simulation. The linear equation of the fit can be written as $f(t) = r_c t + f_0$ where f is the CO_2 ice fraction at time t, f_0 is the 'initial' CO_2 ice fraction, and r_c is the rate of collapse. Since we apply the linear fit starting with the second year of each simulation, the intercept f_0 does not actually capture the initial CO_2 ice fraction. The the simulations begin with an initial ice fraction of zero and spend the first six months of the simulation numerically spinning up. During this period of spin up the CO_2 system is neither linearly growing nor following a seasonal cycle. Therefore we omit this phase from our fit. The fitted value of r_c provides us the timescale, τ, since $\tau = 1/r_c$.

The results of our analysis are shown Tables 3.2 and 3.3. Each table provides the calculated value of the collapse rate and its associated 3-sigma standard deviation, the calculated intercept and its associated 3-sigma standard deviation, and the derived collapse timescale. Figures 3.18 through 3.18 show the fits and the CO_2 ice accumulation curves.

Acknowledgements

This research was originally developed in collaboration with Mark Richardson of Ashima Research and Michael Mischna of JPL. I have benefited from numerous conversations with

Obliquity (degrees)	Initial $\bar{P}_s$ (mb)	Collapse Rate (kg yr^{-1})	$\pm 3\sigma$ (kg yr^{-1})	Intercept (kg)	$\pm 3\sigma$ (kg)	Timescale (yr)
0	6	1.4 $\times 10^{15}$	2.0 $\times 10^{12}$	3.3 $\times 10^{13}$	6.6 $\times 10^{12}$	20
0	60	3.3 $\times 10^{15}$	2.0 $\times 10^{12}$	-5.4 $\times 10^{14}$	6.5 $\times 10^{12}$	86
0	300	2.1 $\times 10^{15}$	2.9 $\times 10^{12}$	-4.2 $\times 10^{14}$	9.4 $\times 10^{12}$	659
0	600	1.5 $\times 10^{15}$	4.6 $\times 10^{12}$	-3.9 $\times 10^{14}$	1.5 $\times 10^{13}$	1940
0	1200	8.7 $\times 10^{14}$	3.3 $\times 10^{12}$	7.6 $\times 10^{13}$	1.1 $\times 10^{13}$	6472
0	3000	9.7 $\times 10^{14}$	5.4 $\times 10^{12}$	4.8 $\times 10^{14}$	1.7 $\times 10^{13}$	14589
5	6	1.5 $\times 10^{15}$	1.3 $\times 10^{13}$	1.4 $\times 10^{14}$	4.1 $\times 10^{13}$	19
5	60	4.1 $\times 10^{15}$	1.8 $\times 10^{13}$	-2.9 $\times 10^{14}$	5.8 $\times 10^{13}$	69
5	300	3.4 $\times 10^{15}$	1.5 $\times 10^{13}$	3.4 $\times 10^{14}$	4.9 $\times 10^{13}$	420
5	600	2.3 $\times 10^{15}$	3.4 $\times 10^{13}$	-1.9 $\times 10^{13}$	1.1 $\times 10^{14}$	1246
5	1200	1.4 $\times 10^{15}$	1.8 $\times 10^{13}$	6.6 $\times 10^{14}$	5.9 $\times 10^{13}$	4086
5	3000	1.2 $\times 10^{15}$	2.1 $\times 10^{13}$	1.0 $\times 10^{15}$	6.9 $\times 10^{13}$	12284
10	6	8.0 $\times 10^{14}$	3.1 $\times 10^{13}$	1.2 $\times 10^{15}$	1.0 $\times 10^{14}$	34
10	60	3.4 $\times 10^{15}$	3.7 $\times 10^{13}$	1.4 $\times 10^{15}$	1.2 $\times 10^{14}$	82
10	300	3.4 $\times 10^{15}$	1.5 $\times 10^{13}$	3.4 $\times 10^{14}$	4.9 $\times 10^{13}$	420
10	600	3.1 $\times 10^{15}$	7.9 $\times 10^{13}$	1.5 $\times 10^{15}$	2.6 $\times 10^{14}$	901
10	1200	2.3 $\times 10^{15}$	7.5 $\times 10^{13}$	1.2 $\times 10^{15}$	2.4 $\times 10^{14}$	2508
10	3000	1.0 $\times 10^{15}$	5.0 $\times 10^{13}$	1.6 $\times 10^{15}$	1.6 $\times 10^{14}$	13755
15	6	2.4 $\times 10^{14}$	5.7 $\times 10^{13}$	2.3 $\times 10^{15}$	1.8 $\times 10^{14}$	108
15	60	2.3 $\times 10^{15}$	7.2 $\times 10^{13}$	3.6 $\times 10^{15}$	2.3 $\times 10^{14}$	121
15	300	2.9 $\times 10^{15}$	1.0 $\times 10^{14}$	3.8 $\times 10^{15}$	3.3 $\times 10^{14}$	493
15	600	3.2 $\times 10^{15}$	1.6 $\times 10^{14}$	2.9 $\times 10^{15}$	5.0 $\times 10^{14}$	889
15	1200	1.3 $\times 10^{15}$	1.3 $\times 10^{14}$	3.8 $\times 10^{15}$	4.2 $\times 10^{14}$	4346
15	3000	3.9 $\times 10^{14}$	7.5 $\times 10^{13}$	3.7 $\times 10^{15}$	2.4 $\times 10^{14}$	36326

Table 3.2: Collapse timescales and related linear regression fit parameters, including slope and intercept.

Obliquity (degrees)	Initial $\bar{P}_s$ (mb)	Collapse Rate (kg yr^{-1})	$\pm 3\sigma$ (kg yr^{-1})	Intercept (kg)	$\pm 3\sigma$ (kg)	Timescale (yr)
20	6	-2.5 $\times 10^{13}$	8.6 $\times 10^{13}$	3.4 $\times 10^{15}$	2.8 $\times 10^{14}$	-980
20	60	1.8 $\times 10^{15}$	1.2 $\times 10^{14}$	5.6 $\times 10^{15}$	4.0 $\times 10^{14}$	156
20	300	2.9 $\times 10^{15}$	1.9 $\times 10^{14}$	5.4 $\times 10^{15}$	6.1 $\times 10^{14}$	484
20	600	3.0 $\times 10^{15}$	2.4 $\times 10^{14}$	5.0 $\times 10^{15}$	7.8 $\times 10^{14}$	931
20	1200	1.2 $\times 10^{15}$	1.9 $\times 10^{14}$	5.0 $\times 10^{15}$	6.2 $\times 10^{14}$	4669
20	3000	-1.3 $\times 10^{14}$	9.7 $\times 10^{13}$	4.2 $\times 10^{15}$	3.1 $\times 10^{14}$	-106853
25	6	-1.7 $\times 10^{13}$	1.3 $\times 10^{14}$	4.1 $\times 10^{15}$	4.0$\times 10^{14}$	-1380
25	60	8.7 $\times 10^{14}$	1.9 $\times 10^{14}$	7.7 $\times 10^{15}$	6.0 $\times 10^{14}$	316
25	300	2.7 $\times 10^{15}$	2.6 $\times 10^{14}$	7.5 $\times 10^{15}$	8.3 $\times 10^{14}$	530
25	600	3.3 $\times 10^{15}$	3.2 $\times 10^{14}$	6.8 $\times 10^{15}$	1.0 $\times 10^{15}$	865
25	1200	8.7 $\times 10^{14}$	2.7 $\times 10^{14}$	7.6 $\times 10^{15}$	8.8 $\times 10^{14}$	6491
25	3000	-2.2 $\times 10^{14}$	1.3 $\times 10^{14}$	5.3 $\times 10^{15}$	4.3 $\times 10^{14}$	-63237
40	6	3.9 $\times 10^{13}$	1.3 $\times 10^{14}$	6.4 $\times 10^{15}$	8.4$\times 10^{14}$	556
40	60	-1.7 $\times 10^{14}$	1.9 $\times 10^{14}$	1.2 $\times 10^{16}$	1.1 $\times 10^{15}$	-1553
40	300	-1.6 $\times 10^{14}$	2.7 $\times 10^{14}$	1.4 $\times 10^{16}$	1.4 $\times 10^{15}$	-8918
40	600	-8.0 $\times 10^{13}$	2.6 $\times 10^{14}$	1.3 $\times 10^{16}$	1.4 $\times 10^{15}$	-35106
40	1200	-2.5 $\times 10^{14}$	3.2 $\times 10^{14}$	1.1 $\times 10^{16}$	1.2$\times 10^{15}$	-22893
40	3000	-2.0 $\times 10^{14}$	1.3 $\times 10^{14}$	7.6 $\times 10^{15}$	7.6 $\times 10^{14}$	-70945

Table 3.3: Collapse timescales and related linear regression fit parameters, including slope and intercept.

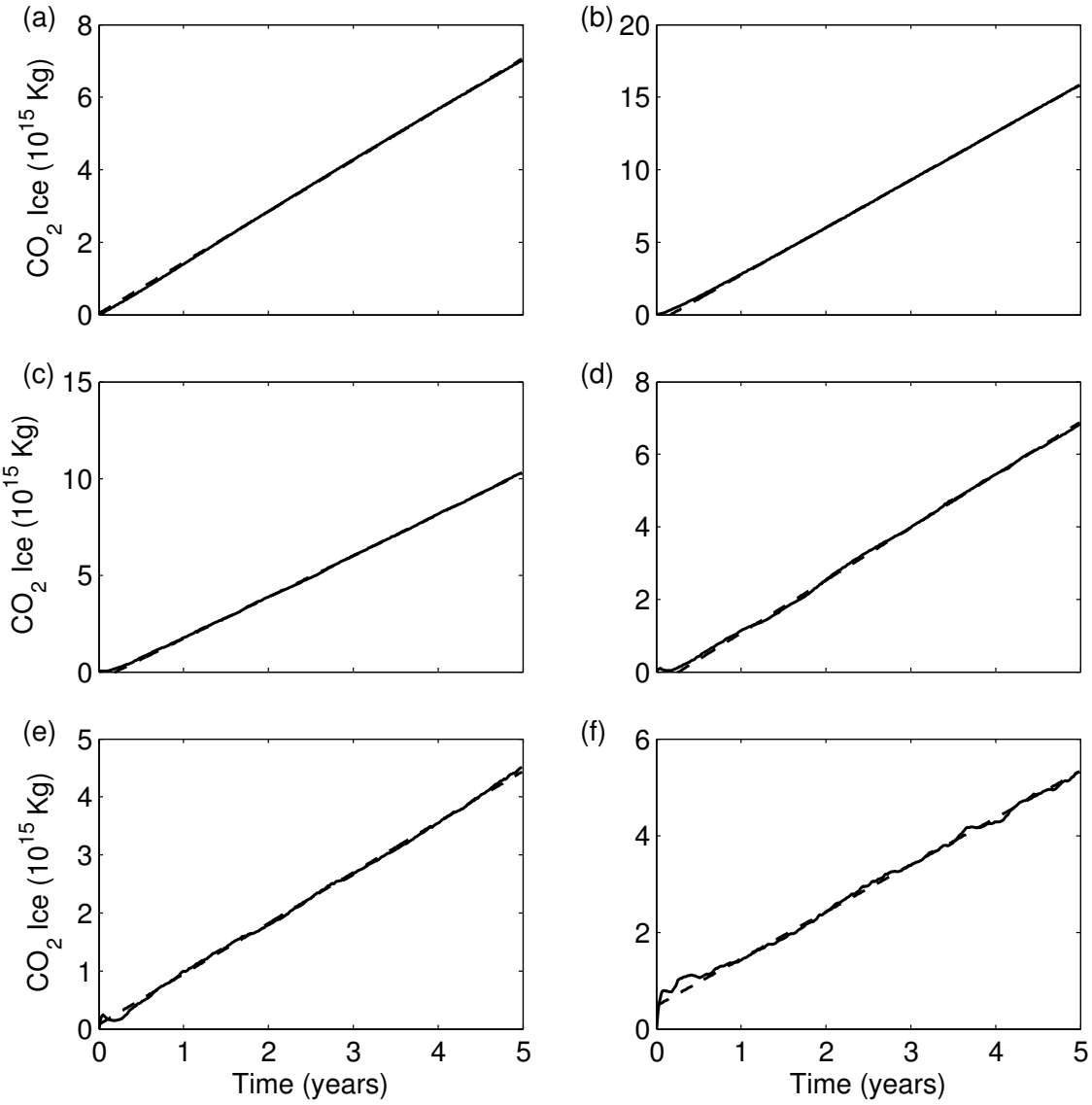

Figure 3.18: Linear regression fits to the CO_2 accumulation for the 0° obliquity simulations at the current solar luminosity. Fits are shown for the (a) 6 mb, (b) 60 mb, (c) 300 mb, (d) 600 mb, (e) 1200 mb, and (f) 3000 mb simulations. The solid black line is the accumulated global CO_2 ice and the dotted line is the linear regression. See the text for the slopes, intercepts, and confidence intervals for the fits.

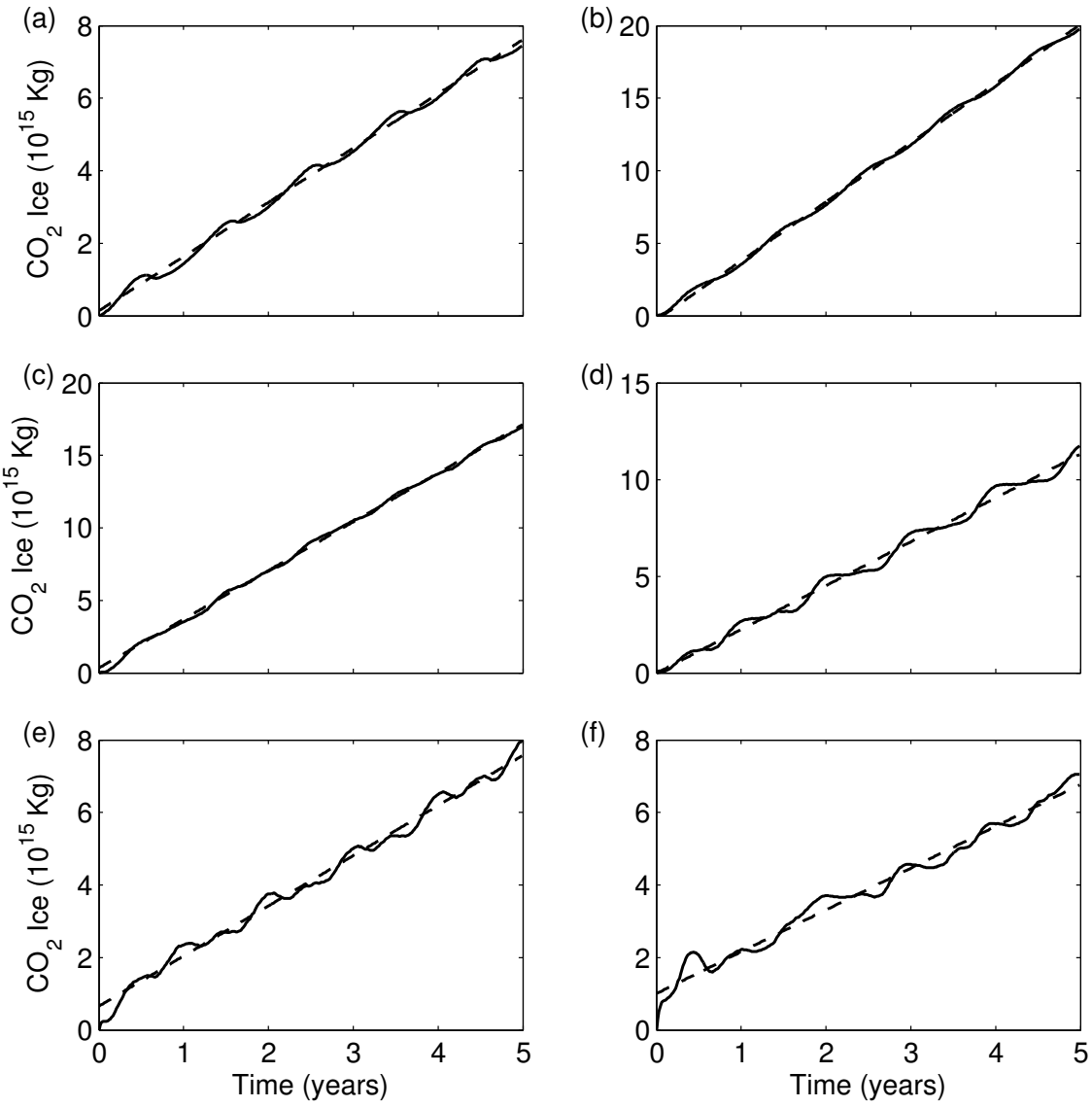

Figure 3.19: Same as Figure 3.18 but for 5° obliquity at the current luminosity.

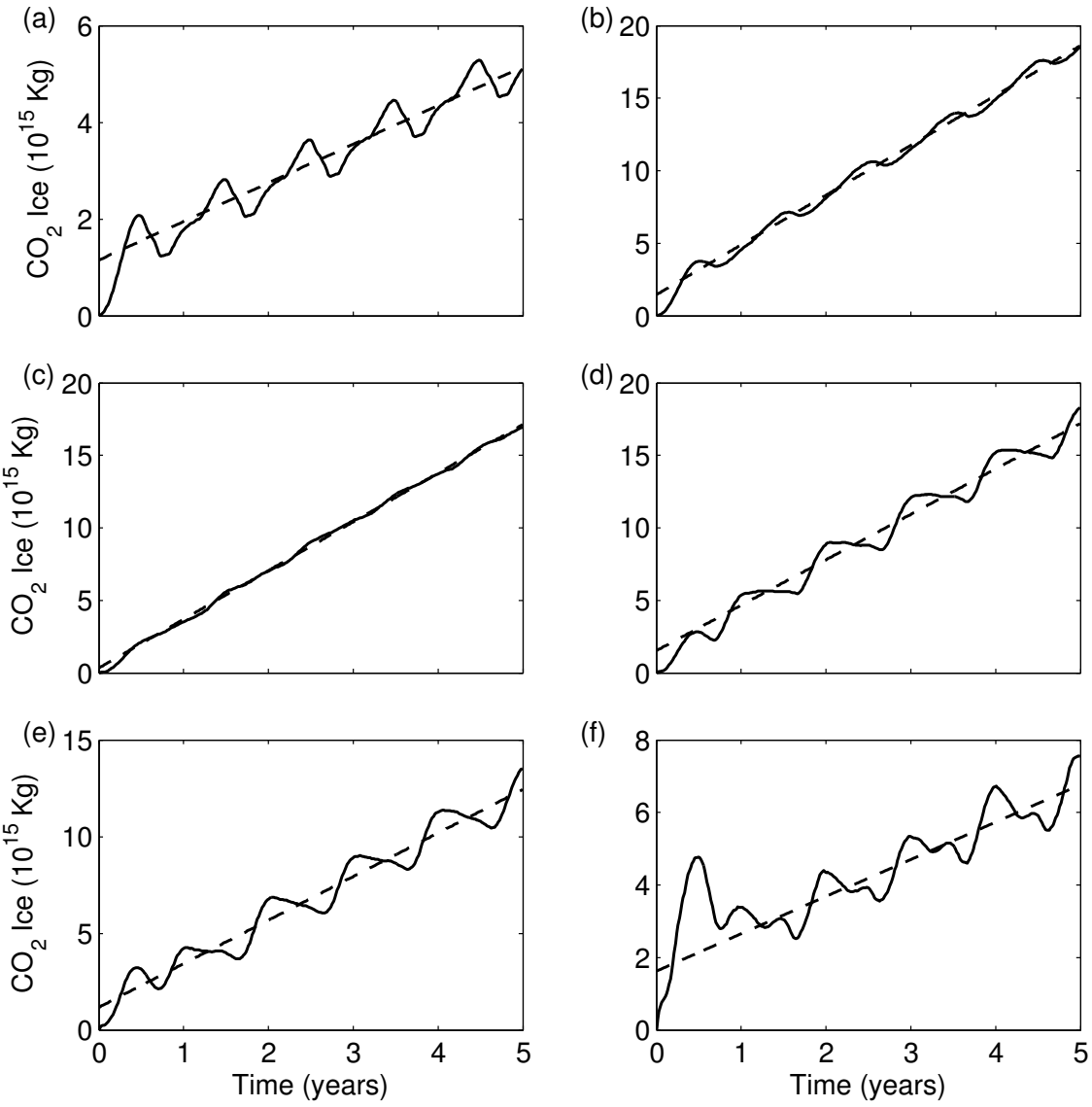

Figure 3.20: Same as Figure 3.18 but for 10° obliquity at the current luminosity.

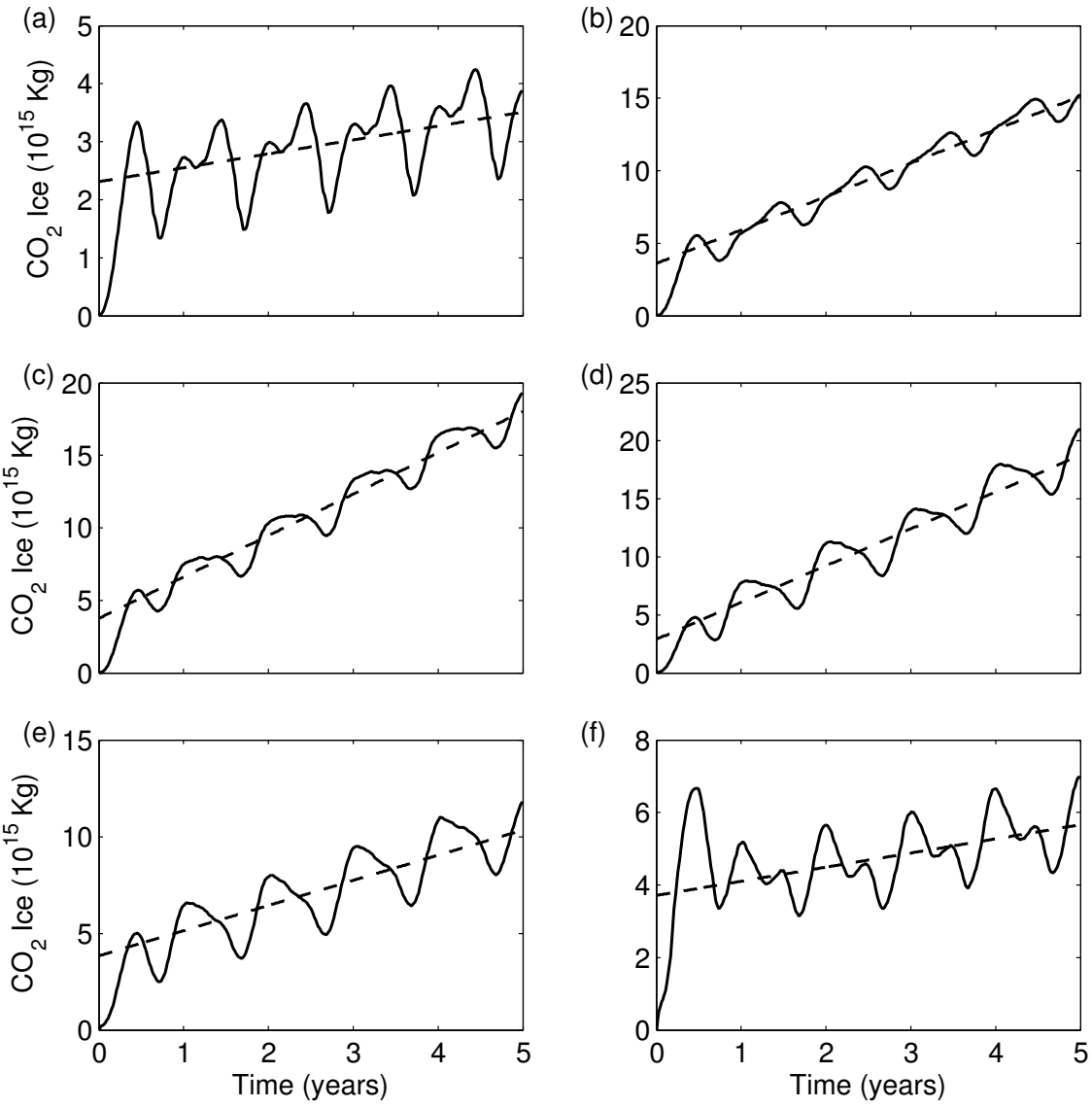

Figure 3.21: Same as Figure 3.18 but for 15° obliquity at the current luminosity.

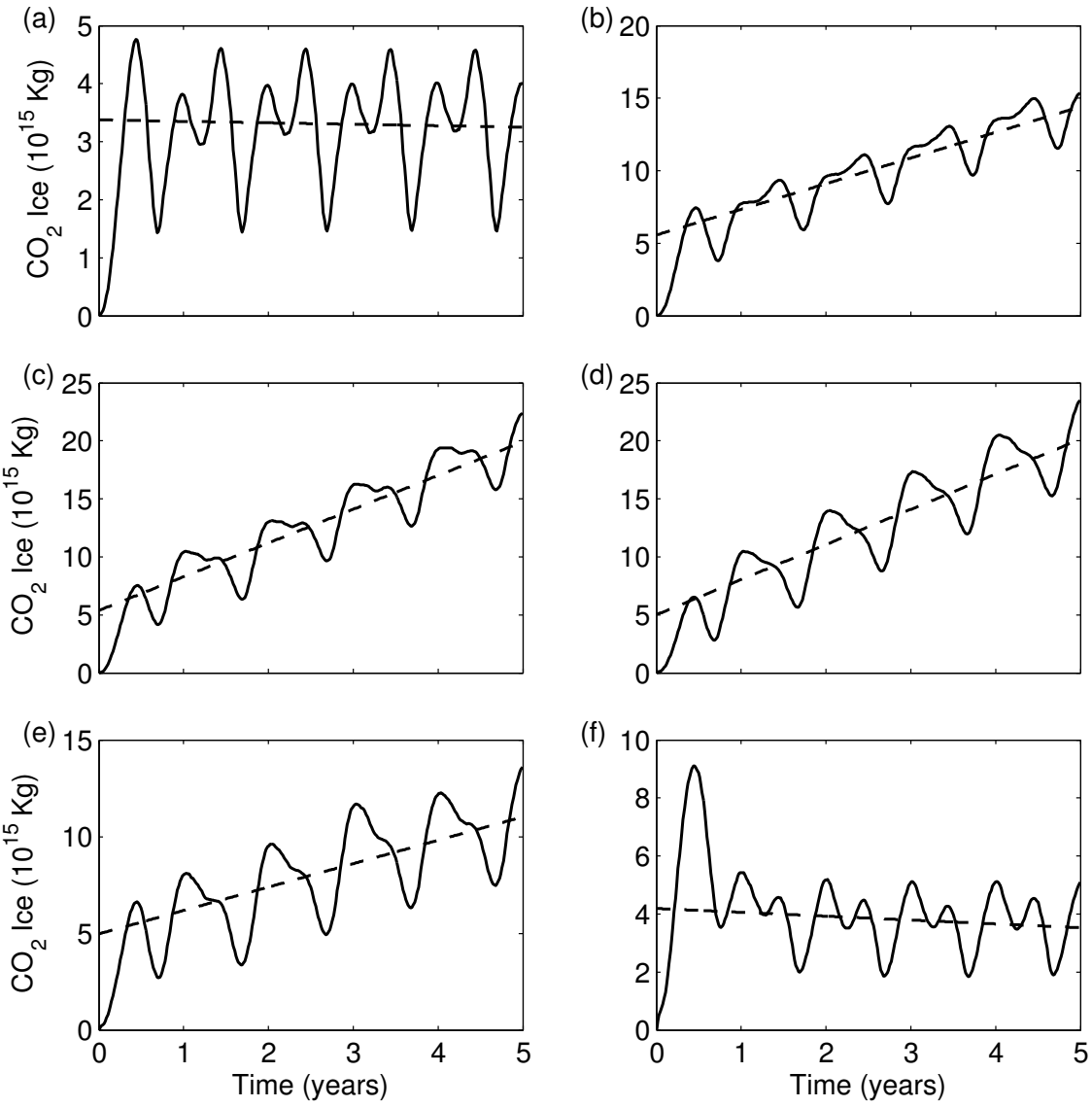

Figure 3.22: Same as Figure 3.18 but for 20° obliquity at the current luminosity.

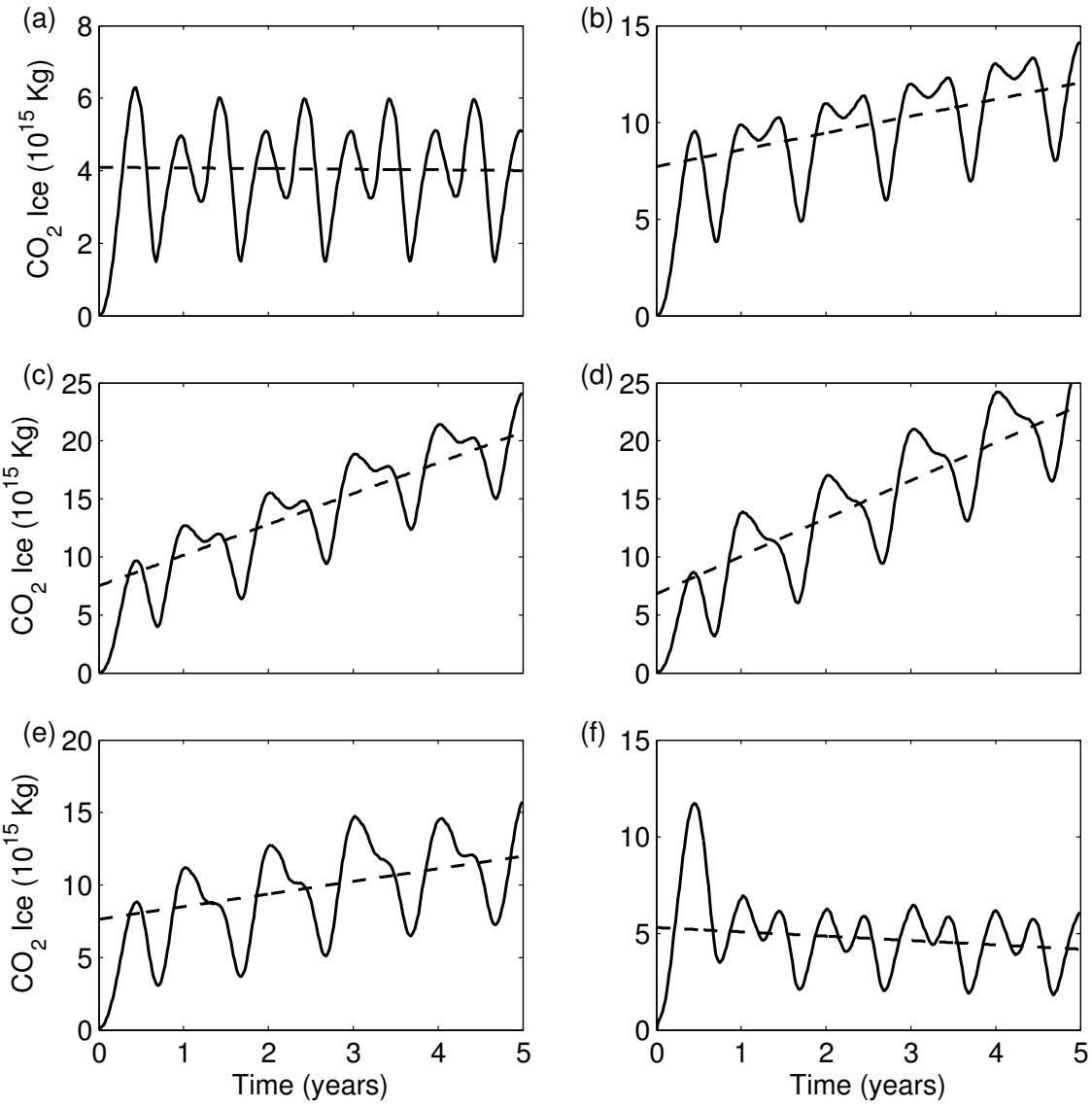

Figure 3.23: Same as Figure 3.18 but for 25° obliquity at the current luminosity.

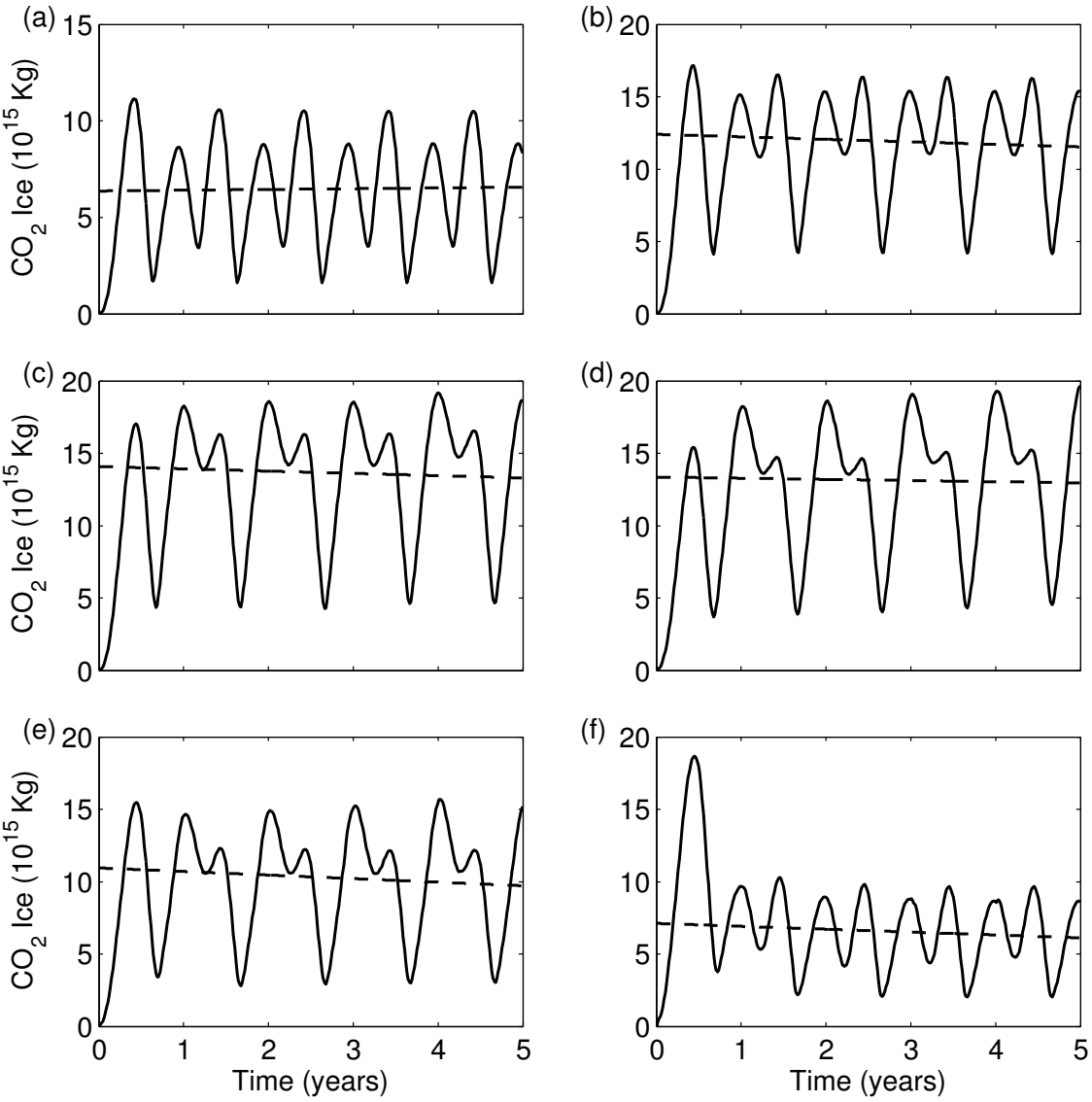

Figure 3.24: Same as Figure 3.18 but for 40° obliquity at the current luminosity.

Andrew Ingersoll of Caltech. I am especially grateful to Itay Halevy, of the Weizmann Institute of Science, who while at Caltech helped clarify my ideas in terms of radiative transfer in carbon dioxide atmospheres and simple green house models.

Chapter 4

Precipitation and Aridity on Ancient Mars

The paradigm of a warm, wet early Mars has been invoked since the first observation of ancient flow channels and other potentially fluvial features on the surface of Mars (*Sagan et al.*, 1973). The mechanism of rainfall and surface runoff is appealing to explain these features on the Martian surface, but it remains problematic from a climate dynamic perspective for several reasons. First, for rainfall to occur the climate must be thermally capable of sustaining surface liquid water. Second, the abundance and distribution of surface liquid water will affect the humidity and potential for rainfall. Previous investigations have only addressed the first of these mechanisms (*Haberle*, 1998). Here we show that the abundance and geographical distribution of available surface water can dramatically change the aridity of a planet, even when the global mean temperature is significantly above freezing. For plausible ocean extents with a favorable thermal state ancient Mars is still predominantly dry with precipitation concentrated on the southern summer intertropical convergence zone (ITCZ). These results suggest that the thermal state of the atmosphere and the abundance and geographical distribution of water both need to be considered when contemplating early

Martian climatic states, and that they place equally important, and orthogonal, constraints on planetary aridity.

The distribution of landmasses is a key consideration when simulating paleoclimatic states of the Earth (*Barron and Washington*, 1982; *Chandler et al.*, 1992; *Hay et al.*, 1990a). The degree to which the landmasses are consolidated and their location relative to the poles and the tropics have a dominant influence on aridity of the Earth's land surface (*Hay et al.*, 1990b). Indeed, one of the driest periods in the Earth's historical record was the late Permian and early Triassic, when the supercontinent of Pangaea sat astride the equator (*Crowley and North*, 1991). In this configuration, global circulation models suggest that much of the continent sat under a monsoonal circulation in which both the rising and sinking branches were located over land (*Parrish*, 1993). Lacking contact with a water source, this circulation yielded a harsh, continental interior desert over much of the land surface. These results from climate studies of ancient Earth have an important consequence for paleoclimate studies of Mars: a warm climate does not necessarily guarantee rainfall and runoff.

Thus, instead of asking how was Mars warmed, we instead ask: In the most extreme limiting case of Earth-like temperatures on early Mars, how wet could Mars have been? The constraints on this problem are in some ways stronger than those we have for ancient Earth. The topography has not changed significantly since the formation of Tharsis several billion years ago (*Phillips et al.*, 2001), and thus the reconstruction of possible ancient land-water boundaries becomes a question of choosing the total available surface water inventory, and thereby setting the mean sea level.

Other aspects of ancient Mars are much less well understood, namely the trace gas and

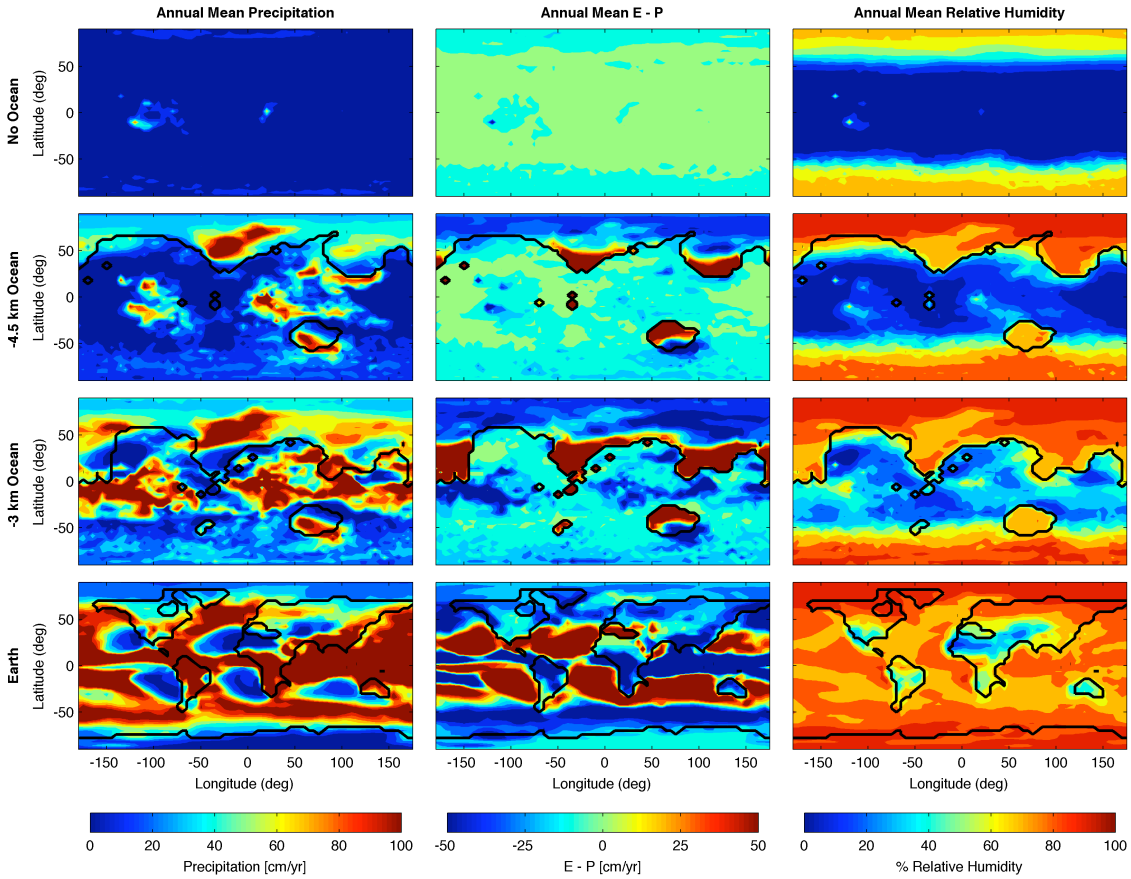

Figure 4.1: Maps of annual mean precipitation, evaporation minus precipitation, and relative humidity. Each row of maps corresponds to the no-ocean/wet-regolith simulation, the -4.5 km sea level ocean simulation, the -3 km sea level ocean simulation, and the current Earth simulation, respectively, from top to bottom. Each column of maps corresponds to annual mean precipitation, annual mean evaporation minus precipitation (E-P), and annual mean relative humidity, respectively, from left to right. The color bar at the bottom of each column applies to all maps in that column. The dark solid line indicates ocean-land boundary. For the -3 km and -4.5 km ocean simulations, the oceans are north of the ocean-land boundary and the Hellas and Argyre basins are partially filled in the southern hemisphere.

particulate composition of the atmosphere and hence the strength of the greenhouse effect are unknown. In order to gain some initial idea of the influence of water distribution on an ancient Mars-like world, an idealized set of simulations are considered in this study. Conceptually, the limiting case of an early Earth-like Martian atmosphere and climate is, in fact, the current atmospheric thermal state of the Earth, in which the mean global surface temperature is sufficient to sustain surface liquid water. Thus, for this study, we use the National Center for Atmospheric Research (NCAR) Community Atmosphere Model (CAM) and, specifically, the finite volume dynamical core and slab ocean model (*Collins et al.*, 2006). To examine precipitation as a function the available water fraction for various Mars landmass distributions, we have changed the topographic boundary condition in CAM to mimic the Mars Orbiter Laser Altimeter (MOLA) global topographic map (*Smith et al.*, 2001). Selecting an effective sea level elevation relative to the MOLA reference specifies the water distribution. All other environmental and orbital parameters were left at their terrestrial values. This is reasonable for a first study of the influence of water distribution since the dynamics of the terrestrial and Martian lower atmospheres are in a similar regime and there are large uncertainties in true ancient Mars conditions.

Since the evidence for an ancient ocean on Mars is debatable (*Head et al.*, 1999; *Carr and Head*, 2003; *Malin and Edgett*, 1999; *Clifford and Parker*, 2001), we first consider a limiting case where no surface liquid water is available, except as regolith (soil) moisture. Setting the CAM land surface type everywhere to that of rainforest in order to bias the simulation towards a moist state, we conducted a simulation with Mars topography and no ocean, shown in Figure 4.1, commencing with an initial Earth-like atmospheric state,

including humidity. At steady state, this dry Mars-as-Earth (hereafter Mearth) had atmospheric relative humidity below $\sim$10% for locations between 45°S and 45°N, net evaporation minus precipitation throughout most of 60°S to 60°N, and few locations within this range with annual precipitation above 2 cm/yr (compare this to terrestrial tropical rainfall which is commonly $>$100 cm/yr). This is a dry world. Indeed, had the tropical and extratropical surface been allowed to desiccate under the influence of the predicted net evaporation rates, all moisture would have been transported to, and trapped at, the poles. What we have modeled is qualitatively similar to the current Mars hydrological regime, in so far that the atmosphere is dry with volatiles trapped at the poles. The short timescale of surface evaporation and atmospheric transport of water is such that ground water flow, with its long transport timescale, could not, on a consistent basis, resupply water to tropical regions fast enough to affect rainfall (*Clifford*, 1993).

The dry Mearth simulations suggest that in the absence of a large surface water deposit, there can be no rainfall. If, as the geological observations seem to indicate, there was rainfall and runoff on ancient Mars (*Craddock and Howard*, 2002), it thus required either rapid and dramatic climatic transients, such as those following major impacts (*Segura et al.*, 2002, 2008), or a sizeable ocean. Thus we examine how the size of the ocean affects precipitation. It should be noted that volcanic emissions do not count as transient for the purposes of this discussion since their aggregate effects occur on timescales much slower than those of atmospheric mixing. For major impacts, rainfall results from the secular redeposition of massive volumes of water vaporized by the impact as the atmosphere cools back to quasi-equilibrium. While post-impact rainfall is a tempting solution to the runoff

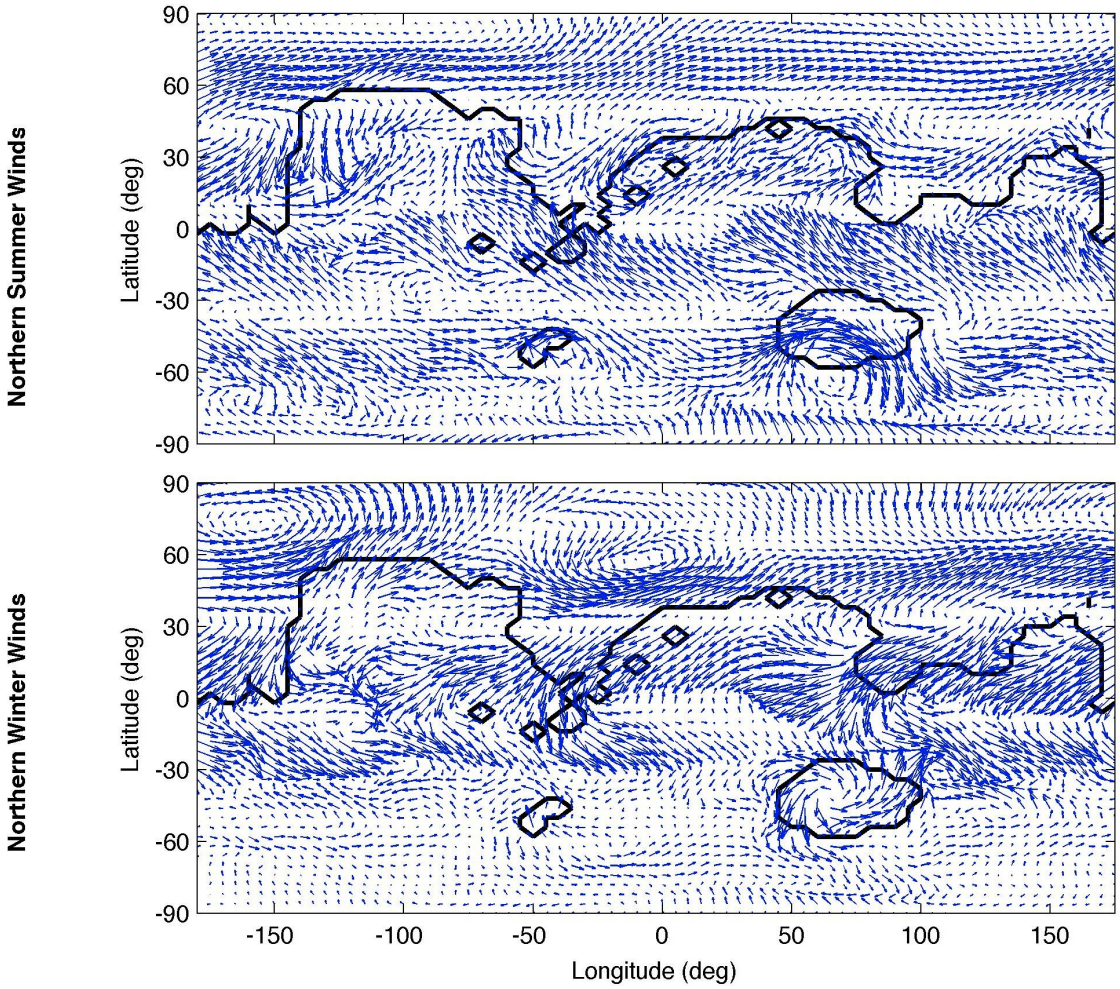

Figure 4.2: Seasonal wind patterns for the -3 km sea level ocean simulation. The northern summer winds indicated a narrow, equatorial intertropical convergence zone (ITCZ), while the northern winter exhibits a monsoonal, off-equator ITCZ. The dark solid line indicates ocean-land boundary, similar to Figure 4.1.

problem for Mars, since it does not require a long-term early warm climate to create rain, some geologists argue that impact-related rain is inconsistent with some of the geological evidence (*Barnhart et al.*, 2009; *Hynek and Phillips*, 2003). Our investigation focuses on the constraints levied on a Mars-like planet if rainfall is required to be a natural part of the climate system.

We examined water amounts such that the Martian topography is filled to 3 km and 4.5 km below the MOLA reference geoid (*Smith et al.*, 2001), which are comparable to proposed ocean shorelines (*Carr and Head*, 2003), as shown in Figure 4.1. These elevations create dry land fractions of 7% and 85%, respectively. Both cases yield precipitation values much higher than the no-ocean case, and up to levels similar to those of the current Earth (*Xie and Arkin*, 1997). While the annual mean relative humidity (RH) in the tropics is generally less than 50% and 30%, for the -3 km and -4.5 km simulations, respectively, annual precipitation in the tropics reaches 100 cm/yr in some regions (more commonly in the -3 km case than the -4.5 km case). In the -4.5 km case, most precipitation takes place over the northern ocean and is associated with low-pressure (baroclinic) weather systems. In the -3 km case, much more tropical rainfall is predicted in association with intertropical convergence zone (ITCZ) convective systems. The difference between these cases is the location of the northern ocean shoreline closer to the equator in the -3 km case, and, specifically, its location within the region of the tropical meridional overturning circulation. The increased ability of the atmosphere to extract evaporated water from the northern ocean can be seen in the comparison of evaporation minus precipitation (E-P) between the two ocean level cases. Much larger fingers of positive E-P can be seen in the regional lows near 260°

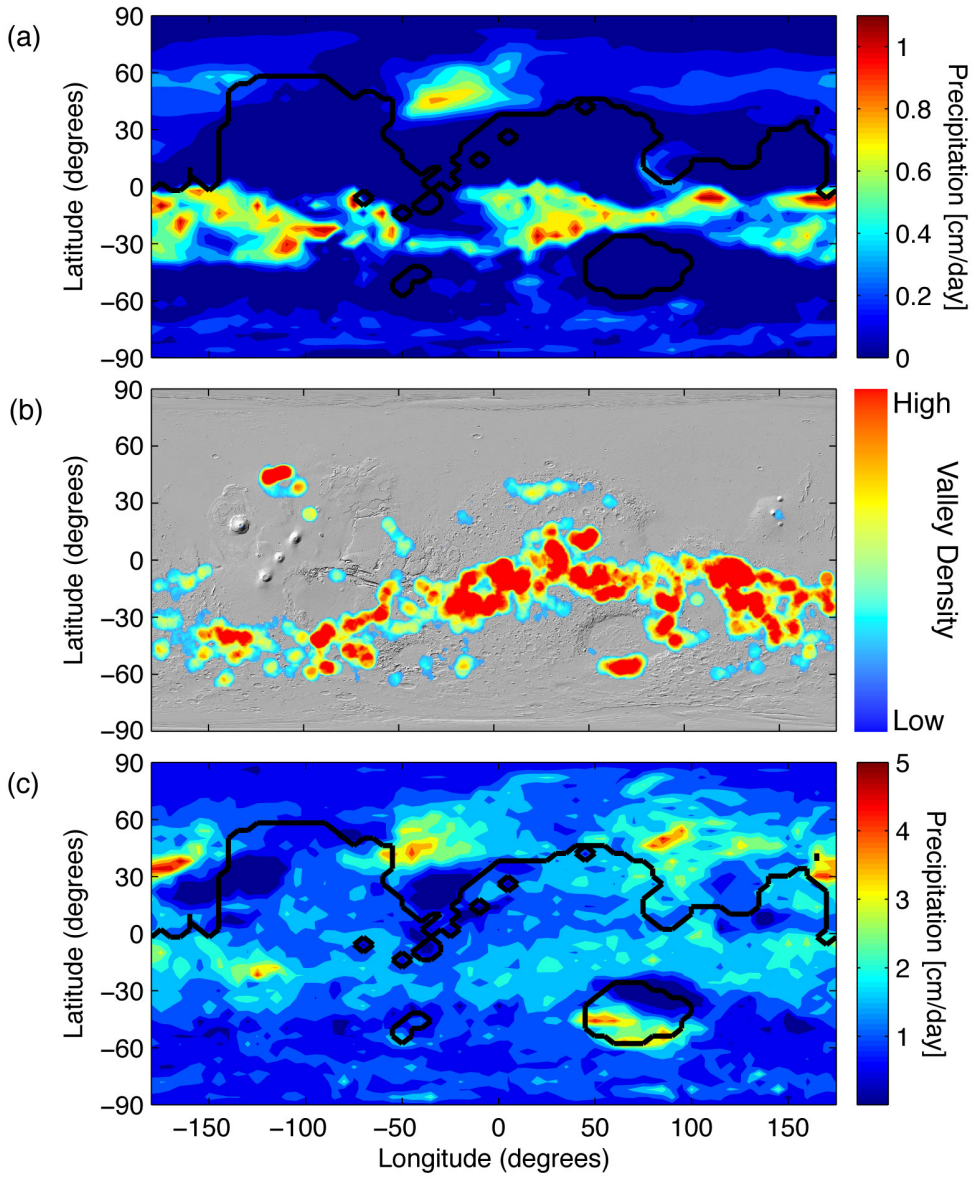

Figure 4.3: Comparison of simulated precipitation patterns with observed Martian valley network locations. From the Mearth simulations, the distribution of the southern summer mean precipitation (A) is similar to the observed distribution of valley networks on Mars (B) (*Hynek et al.*, 2010). Similarly, the maximum daily precipitation for a given year (C) shows a distribution comparable to the Mars valley network distribution. For (A) and (C), the dark solid line indicates ocean-land boundary, similar to Figures 4.1 and 4.2. The valley density map in (B) is modified from *Hynek et al.* (2010).

W, 180°, and 30° W. These positive E-P values are reflected in much higher values of RH in these same regions. The large E-P and RH in the southern hemisphere near 270° W is associated with the large sea within the deep Hellas basin.

Despite limited locations of nearly terrestrial tropical rainfall, much of the model domains show very low precipitation rates, especially in the southern mid- and high-latitudes and for the -4.5 km ocean. In the latter case, much of the land surface experiences precipitation rates below 5 cm/yr and with positive E-P. These locations would be considered deserts by terrestrial categorization. Even in the wetter -3 km ocean case, much of the southern mid- and high-latitudes are deserts. Additional higher obliquity Mearth simulations (at 45 and 60 degrees) only strengthen this pattern of wet ITCZ and dry mid- and high- latitudes, as seen in Figure 4.4. Although the mean precipitation in the southern latitudes increases as the obliquity increases, there is still a sharp drop in the extreme rainfall around -30° latitude, even at high obliquities, and thus the southern mid-latitudes and polar regions remain dry. The reason for this insensitivity to obliquity remains to be determined, but the result remains: even with deep oceans and high orbital obliquities, the southern regions of Mars remain extremely arid.

A novelty of the Mearth simulation results is the strong hemispheric asymmetry in the climate. In this case, the asymmetry has nothing to do with the Martian orbital eccentricity since terrestrial orbital parameters have been used. Instead, the behavior is associated with the asymmetry in ocean cover, where most of the water is located in the Northern Lowlands. As shown in Figure 4.2, the large contrast in thermal capacity of the ocean versus the land yields an ITCZ much more confined around the equator in northern summer, and a mon-

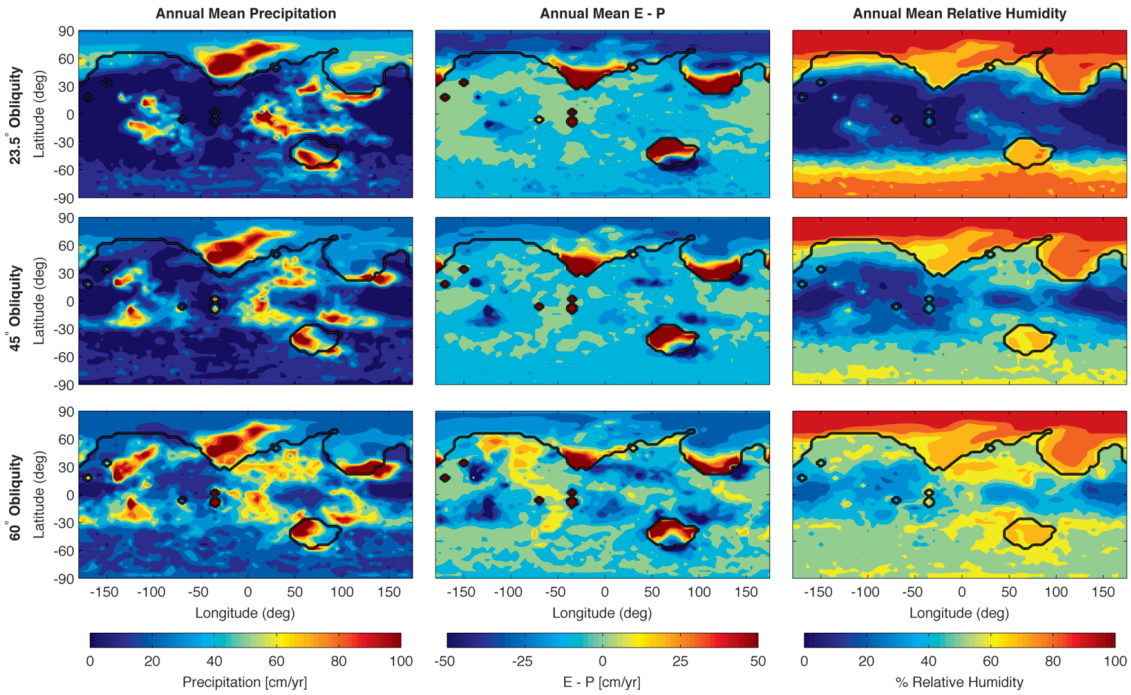

Figure 4.4: Simulation results are shown for three different obliquities for the -4.5 km ocean scenario. Each row of plots corresponds to a particular obliquity, indicated by the labels on the left-hand side. The left column shows the annual mean precipitation, in units of centimeter per year. The central column shows the annual mean of evaporation minus precipitation (E-P), in units of centimeters per year. The right column shows the annual mean relative humidity. The thick black line marks the land-ocean boundary.

soonal, significantly off-equator ITCZ during southern summer. This circulation pattern yields mean equatorward advection throughout the year in the north, and alternating equatorward/poleward transport in the south during southern winter and summer. Depending on whether the northern ocean falls within the tropical circulation, the strong monsoonal flow in southern summer can yield significant ITCZ rainfall, as shown in Figure 1. In the -3 km case, the ocean is within the tropical circulation at certain longitudes, while the -4.5 km ocean terminates mostly poleward of the tropical overturning circulation. It is interesting to note the general similarity of the tropical surface wind patterns in the southern summer Mearth simulation with the wind patterns predicted by contemporary Mars GCMs and validated against surface wind indicators like dust streaks (*Fenton and Richardson*, 2001; *Greeley et al.*, 1993), reaffirming the similarity of the circulation regimes.

Interestingly, the geographical distribution of precipitation associated with southern summer monsoonal flow is similar to the observed geographical distribution of ancient valley network, lake, and delta fan features, as seen in Figure 4.3. The marked tropical distribution of these features has been noted before (*Fassett and Head*, 2008; *Hynek et al.*, 2010), sometimes in the context of the dichotomy boundary. These simulations suggest that the geological features carved by liquid water runoff were likely formed due to ITCZ convective rainfall largely during southern summers, if rainfall were climatically controlled. The confinement of ancient fluvial features to the tropics and the southern hemisphere near the Hellas basin is then simply a natural consequence of where peak rainfall occurred resulting from a combination of availability of water sources (seas) and the mean circulation patterns. Much of the southern mid- and high-latitudes are free of fluvial features because

winter storm rain would have been rare due to the vast distance from seas (save for the areas around Hellas and possibly Argyre). Since the north would have been covered by an ocean the formation of fluvial landforms would not have been expected, and in any case the north was volcanically resurfaced after the era of fluvial feature formation (*Head et al.*, 2002). The expected distribution of impact-induced rainfall is not clear. The vapor would initially have been uniformly distributed over the globe, and its evolution would not have been controlled by the distribution of surface reservoirs that is critical to the desiccation of much of the southern mid- and high-latitudes (*Segura et al.*, 2008). Further work modeling the distribution of rainfall expected from the nonequilibrium state following a major impact is needed in order to assess whether rainfall geographical distribution can be used as a means of differentiating between impact and ocean-related mechanisms for rainfall.

The Mearth simulations illustrate some important constraints on global precipitation and aridity. First, the simulations suggest that for atmospheric humidity to be high enough to allow precipitation, a large exposed surface water deposit is necessary (or more provocatively no ocean, no rainfall.) Second, even in the presence of a large northern ocean and temperatures such as those seen on Earth today, much of the planet, and almost all of the southern mid- and high-latitudes would have been extremely arid by terrestrial standards — much drier than the continental interior during the Permian and Triassic period on Earth. Finally, the simulations predict that if extensive rain were to occur, the ocean location and Martian topography suggest that most rain, and the most intense rain, would fall in association with the southern summer ITCZ. The location of this ITCZ is rather insensitive to obliquity, and agrees suggestively well with the observed distribution of valley networks

and other ancient fluvial features on Mars (*Craddock and Howard*, 2002; *Fassett and Head*, 2008; *Hynek and Phillips*, 2003).

Methods

Previous research on the Martian paleoclimate has focused on how to achieve a warm, wet Martian climate. Such an approach has generally encountered difficulties in generating a combination of radiative and atmospheric parameters that produce a warm, wet Mars climate. We avoid the difficulties that previous research has faced by addressing a different paleoclimate question. Instead of asking how the ancient Martian climate was warm and wet, we ask: What did a warm and wet ancient Martian climate look like?

We qualitatively investigated the controls on precipitation and aridity, with a particular emphasis on how the abundance and distribution of surface water controlled precipitation and aridity. Therefore, we required a global circulation model that used well understood and tested physics schemes and thus provided qualitatively accurate insights into the controls on precipitation and aridity. We used NCARs Community Atmosphere Model (CAM), version 3 (*Collins et al.*, 2006), which includes a slab ocean and a range of land surface properties. For our investigation, we set the surface to have "rainforest" levels of moisture. This surface parameter choice fits one of our hypotheses, namely that even in extremely wet regimes large portions of Mars would be dry. Since we were testing the importance of surface water and land distribution, we changed the topography map in CAM to reflect Mars topography. We downsampled the Mars Orbiter Laser Altimeter (MOLA) global topographic map (*Smith et al.*, 2001) to match the $4^\circ \times 5^\circ$ horizontal resolution in our sim-

ulations. For various scenarios, we changed the amount of water in the system, from the equivalent of a saturated regolith all the way to a deep northern ocean. The water volume was set by filling all depressions to a common geodetic height, either -4.5 km or -3 km with respect to the Martian geoid.

All other model parameters were left at Earth values. This was a reasonable choice because despite the differences in gravity, planetary radii, and atmospheric thicknesses, the current Martian atmosphere exhibits similar structure to the current atmosphere of Earth. Both planetary atmospheres generate classic Hadley cell circulations, though the upper extent of the Earth's Hadley cell is limited by the tropopause, whereas the Martian atmosphere lacks a tropopause (*Lewis*, 2003). Still, the bulk of the mass flow even on Mars is within the first few scale heights, which is comparable to the height of the Earth's troposphere. On both Earth and Mars, heat transport at low latitudes is handled by the Hadley cell while mid-latitude heat transport is driven by baroclinic instabilities (*Lewis*, 2003). The current Martian atmosphere has a large asymmetry in solstitial circulation that is not seen on the Earth. However, this asymmetry in the Martian solstitial circulation is due to the Martian topographic dichotomy (*Richardson and Wilson*, 2002). For the Mars ocean case, this topography difference between the northern and southern hemisphere is minimized. For the qualitative nature of our investigation, the similarities outweigh the differences and allow us to understand the impact of surface water abundance and distribution on the precipitation and aridity of a warm, wet Mars.

Acknowledgements

I would like to thank Mark Richardson of Ashima Research for the conversations that lead to this project. I am also grateful for the model development help provided by Claire Newman of Ashima Research. As well, conversations with Jeffrey Andrews-Hanna of the Colorado School of Mines, Robert Craddock of the Smithsonian Institute, and Brian Hynek of the University of Colorado were extremely helpful in providing geological context to this work.

Bibliography

Andrews-Hanna, J. C., and K. W. Lewis (2011), Early Mars hydrology: 2. Hydrological evolution in the Noachian and Hesperian epochs, *J. Geophys. Res.*, *116*(E2).

Arakawa, A., and V. Lamb (1997), Computational design of the basic dynamical processes of the UCLA general circulation model, in *Methods of Computational Physics*, vol. 17, pp. 173–265., Academic Press, New York.

Armstrong, J. C., and C. B. Leovy (2005), Long term wind erosion on Mars, *Icarus*, *176*(1), 57–74, doi: 10.1016/j.icarus.2005.01.005.

Baker, V. R., M. H. Carr, V. C. Gulick, C. R. Williams, and M. S. Marley (1992), Channels and valley networks, in *Mars*, pp. 493–522, University of Arizona.

Bandfield, J. L., V. E. Hamilton, and P. R. Christensen (2000), A Global View of Martian Surface Compositions from MGS-TES, *Science*, *287*, 1626–1630.

Bandfield, J. L., T. D. Glotch, and P. R. Christensen (2003), Spectroscopic identification of carbonate minerals in the Martian dust, *Science*, *301*(5636), 1084–1087.

Barnhart, C. J., A. D. Howard, and J. M. Moore (2009), Long-term precipitation and late-stage valley network formation: Landform simulations of Parana Basin, Mars, *Journal of Geophysical Research*, *114*(E01003), doi: 10.1029/2008JE003122.

Barron, E. J., and W. M. Washington (1982), Atmospheric circulation during warm geologic periods: Is the equator-to-pole surface-temperature gradient the controlling factor?, *Geology*, *10*, 633–636.

Bibring, J.-P., Y. Langevin, A. Gendrin, B. Gondet, F. Poulet, M. Berthe, A. Soufflot, R. Arvidson, N. Mangold, J. Mustard, P. Drossart, and the OMEGA team (2005), Mars surface diversity as revealed by the OMEGA/Mars Express observations, *Science*, *307*(5715), 1576–1581, doi: 10.1126/science.1108806.

Bibring, J.-P., Y. Langevin, J. F. Mustard, F. Poulet, R. Arvidson, A. Gendrin, B. Gondet, N. Mangold, P. Pinet, and F. Forget (2006), Global Mineralogical and Aqueous Mars History Derived from OMEGA/Mars Express Data, *Science*, *312*, 400–404, doi: 10.1126/science.1122659.

Bohren, C., and B. Albrecht (1998), *Atmospheric thermodynamics*, Oxford University Press.

Brain, D. A., and B. M. Jakosky (1998), Atmospheric loss since the onset of the Martian geologic record: Combined role of impact erosion and sputtering, *Journal of Geophysical Research*, *103*, 22,689–22,694, doi: 10.1029/98JE02074.

Byrne, S., and A. P. Ingersoll (2003), Martian climatic events on timescales of centuries: Evidence from feature morphology in the residual south polar ice cap, *Geophysical Research Letters*, *30*, 29–1.

Caballero, R., R. Pierrehumbert, and J. Mitchell (2008), Axisymmetric, nearly inviscid

circulations in non-condensing radiative-convective atmospheres, *Quarterly Journal of the Royal Meteorological Society*, *134*(634), 1269–1285.

Carr, M. H. (1996), *Water on Mars*, Oxford University Press.

Carr, M. H., and J. W. Head (2003), Oceans on Mars: An assessment of the observational evidence and possible fate, *Journal of Geophysical Research*, *108*(E5), 5042, doi: 10.1029/2002JE001963.

Carr, M. H., and J. W. Head III (2010), Geologic history of Mars, *Earth and Planetary Science Letters*, *294*(3–4), 185–203.

Chandler, M. A., D. Rind, and R. Ruedy (1992), Pangaean climate during the early jurassic: Gcm simulations and the sedimentary record of paleoclimate, *Geological Society of America Bulletin*, *104*(5), 543–559.

Christensen, P. R., J. L. Bandfield, V. E. Hamilton, S. W. Ruff, H. H. Kieffer, T. N. Titus, M. C. Malin, R. V. Morris, M. D. Lane, R. L. Clark, B. M. Jakosky, M. T. Mellon, J. C. Pearl, B. J. Conrath, M. D. Smith, R. T. Clancy, R. O. Kuzmin, T. Roush, G. L. Mehall, N. Gorelick, K. Bender, K. Murray, S. Dason, E. Greene, S. Silverman, and M. Greenfield (2001), Mars Global Surveyor Thermal Emission Spectrometer experiment: Investigation description and surface science results, *Journal of Geophysical Research*, *106*, 23,823–23,872, doi: 10.1029/2000JE001370.

Clifford, S. M. (1993), A model for the hydrologic and climatic behavior of water on Mars, *Journal of Geophysical Research*, *98*, 10,973.

Clifford, S. M., and T. J. Parker (2001), The Evolution of the Martian Hydrosphere: Implications for the Fate of a Primordial Ocean and the Current State of the Northern Plains, *Icarus*, *154*, 40–79, doi: 10.1006/icar.2001.6671.

Colaprete, A., and O. B. Toon (2003), Carbon dioxide clouds in an early dense martian atmosphere, *J. Geophys. Res.*, *108*(E4), doi: 10.1029/2002JE001967.

Colaprete, A., and O. B. Toon (2003), Carbon dioxide clouds in an early dense Martian atmosphere, *Journal of Geophysical Research (Planets)*, *108*, 6–1, doi: 10.1029/2002JE001967.

Collins, W., P. Rasch, B. Boville, J. Hack, J. McCaa, D. Williamson, B. Briegleb, C. Bitz, S. Lin, and M. Zhang (2006), The formulation and atmospheric simulation of the community atmosphere model version 3 (cam3), *Journal of Climate*, *19*, 2144–2161, doi: 10.1175/JCLI3760.1.

Craddock, R. A., and A. D. Howard (2002), The case for rainfall on a warm, wet early Mars, *Journal of Geophysical Research*, *107*(E11), 5111, doi: 10.1029/2001JE001505.

Crowley, T. J., and G. R. North (1991), *Paleoclimatology*, Oxford Monographs on Geology and Geophysics, Oxford University Press, New York.

Cutts, J. A., and B. H. Lewis (1982), Models of climate cycles recorded in Martian polar layered deposits, *Icarus*, *50*(2–3), 216–244, doi: DOI:10.1016/0019-1035(82)90124-5.

di Achille, G., and B. Hynek (2010), Deltas and valley networks on mars, in *Lakes on Mars*, p. 223, Elsevier Science.

Ehlmann, B. L., J. F. Mustard, S. L. Murchie, J.-P. Bibring, A. Meunier, A. A. Fraeman, and Y. Langevin (2011), Subsurface water and clay mineral formation during the early history of Mars, *Nature*, *479*(7371), 53–60.

Fanale, F. P., J. R. Salvail, W. B. Banerdt, and R. S. Saunders (1982), Mars: The regolith-atmosphere-cap system and climate change, *Icarus*, *50*(2–3), 381–407, doi: DOI:10.1016/0019-1035(82)90131-2.

Fassett, C. I., and J. W. Head (2008), Valley network-fed, open-basin lakes on Mars: Distribution and implications for Noachian surface and subsurface hydrology, *Icarus*, *198*(1), 37–56, doi: 10.1016/j.icarus.2008.06.016.

Fassett, C. I., and J. W. Head (2011), Sequence and timing of conditions on early Mars, *Icarus*, *211*(2), 1204–1214.

Fenton, L. K., and M. I. Richardson (2001), Martian surface winds: Insensitivity to orbital changes and implications for aeolian processes, *Journal of Geophysical Research*, *106*(E12), 32,885–32,902.

Forget, F., and R. T. Pierrehumbert (1997), Warming early Mars with carbon dioxide clouds that scatter infrared radiation, *Science*, *278*(5341), 1273–1276, doi: 10.1126/science.278.5341.1273.

Fu, Q., and K. N. Liou (1992), On the correlated k-distribution method for radiative transfer in nonhomogenecous atmospheres, *Journal of the Atmospheric Sciences*, *49*(22), 2139–2156.

Gierasch, P. J., and O. B. Toon (1973), Atmospheric pressure variation and the climate of Mars, *Journal of the Atmospheric Sciences*, *30*(8), 1502–1508.

Gilliland, R. L. (1989), Solar evolution, *Palaeogeography, Palaeoclimatology, Palaeoecology*, *75*(1–2), 35–55.

Glasser, L. (2002), Equations of state and phase diagrams, *Journal of Chemical Education*, *79*(7), 874, doi: 10.1021/ed079p874.

Gough, D. O. (1981), Solar interior structure and luminosity variations, *Solar Physics*, *74*, 21–34.

Greeley, R. A., A. Skypeck, and J. B. Pollack (1993), Martian aeolian features and deposits: comparisons with general circulation model results, *Journal of Geophysical Research*, *98*(E2), 3183–3196.

Grotzinger, J. P., R. E. Arvidson, J. F. Bell, W. Calvin, B. C. Clark, D. A. Fike, M. Golombek, R. Greeley, A. Haldemann, K. E. Herkenhoff, B. L. Jolliff, A. H. Knoll, M. Malin, S. M. McLennan, T. Parker, L. Soderblom, J. N. Sohl-Dickstein, S. W. Squyres, N. J. Tosca, and W. A. Watters (2005), Stratigraphy and sedimentology of a dry to wet eolian depositional system, Burns formation, Meridiani Planum, Mars, *Earth and Planetary Science Letters*, *240*, 11–72, doi: 10.1016/j.epsl.2005.09.039.

Grotzinger, J. P., R. E. Arvidson, J. F. Bell, III, B. C. Clark, W. H. Farrand, K. Herkenhoff, J. R. Johnson, A. H. Knoll, E. McCartney, S. M. McLennan, J. Metz, T. Parker, J. Soderblom, S. W. Squyres, R. Sullivan, N. Tosca, and Athena Science Team (2006), Sedimentary Facies, Subaqueous Sediment Transport, and Depositional Environment of

the Burns Formation, Meridiani Planum, in *37th Annual Lunar and Planetary Science Conference*, edited by S. Mackwell and E. Stansbery, p. 2254.

Guo, X., M. I. Richardson, A. Soto, and A. Toigo (2010), On the mystery of the perennial carbon dioxide cap at the south pole of Mars, *Journal of Geophysical Research*, *115*(E04005), doi: 10.1029/2009JE003382.

Haberle, R. M. (1998), Early Mars climate models, *Journal of Geophysical Research*, *103*, 28,467–28,479.

Haberle, R. M., D. Tyler, C. P. McKay, and W. L. Davis (1994), A model for the evolution of CO2 on Mars, *Icarus*, *109*, 102–120, doi: 10.1006/icar.1994.1079.

Hay, W. W., E. J. Barron, and S. L. Thompson (1990a), Results of global atmospheric circulation experiments on an Earth with a meridional pole-to-pole continent., *Journal of the Geological Society*, *147*, 385–392.

Hay, W. W., E. J. Barron, and S. L. Thompson (1990b), Global atmospheric circulation experiments on an Earth with polar and tropical continents, *Journal of the Geological Society of London*, *147*(5), 749–757.

Head, J. W., H. Hiesinger, M. A. Ivanov, M. A. Kreslavsky, S. Pratt, and B. J. Thomson (1999), Possible ancient oceans on Mars: evidence from Mars Orbiter Laser Altimeter data, *Science*, *286*(5447), 2134, doi: 10.1126/science.286.5447.2134.

Head, J. W., M. A. Kreslavsky, and S. Pratt (2002), Northern lowlands of Mars: evidence

for widespread volcanic flooding and tectonic deformation in the hesperian period, *Journal of Geophysical Research*, *107*(E1), 5003, doi: 10.1029/2000JE001445.

Head, J. W., J. F. Mustard, M. A. Kreslavsky, R. E. Milliken, and D. R. Marchant (2003), Recent ice ages on Mars, *Nature*, *426*(6968), 797–802, doi: 10.1038/nature02114.

Held, I., and A. Hou (1980), Nonlinear axially symmetric circulations in a nearly inviscid atmosphere, *Journal of Atmospheric Sciences*, *37*, 515–533.

Hess, S. L., R. M. Henry, and J. E. Tillman (1979), The Seasonal Variation of Atmospheric Pressure on Mars as Affected by the South Polar Cap, *Journal of Geophysical Research*, *84*(B6), 2923–2927, doi: 10.1029/JB084iB06p02923.

Hess, S. L., J. A. Ryan, J. E. Tillman, R. M. Henry, and C. B. Leovy (1980), The annual cycle of pressure on Mars measured by Viking Landers 1 and 2, *Geophysical Research Letters*, *7*(3), 197–200.

Hurowitz, J. A., and S. M. McLennan (2007), A $\sim$ 3.5 ga record of water-limited, acidic weathering conditions on Mars, *Earth and Planetary Science Letters*, *260*(3–4), 432–443, doi: 10.1016/j.epsl.2007.05.043.

Hynek, B. M., and R. J. Phillips (2003), New data reveal mature, integrated drainage systems on mars indicative of past precipitation, *Geology*, *31*, 757–760.

Hynek, B. M., M. Beach, and M. R. T. Hoke (2010), Updated global map of Martian valley networks and implications for climate and hydrologic processes, *J. Geophys. Res.*, *115*(E9).

Jakosky, B. M., and R. J. Phillips (2001), Mars' volatile and climate history, *Nature*, *412*(6843), 237–244.

James, P. B., and G. R. North (1982), The seasonal CO_2 cycle on Mars: An application of an energy balance climate model, *J. Geophys. Res.*, *87*(B12), 10,271–10,283.

Johnson, S. S., M. A. Mischna, T. L. Grove, and M. T. Zuber (2008), Sulfur-induced greenhouse warming on early Mars, *Journal of Geophysical Research*, *113*(E8).

Johnson, S. S., A. A. Pavlov, and M. A. Mischna (2009), Fate of SO_2 in the ancient Martian atmosphere: Implications for transient greenhouse warming, *Journal of Geophysical Research*, *114*(E11).

Kass, D., and Y. Yung (1995), Loss of atmosphere from Mars due to solar wind-induced sputtering, *Science*, *268*(5211), 697–699, doi: 10.1126/science.7732377.

Kasting, J. F. (1991), CO_2 condensation and the climate of early Mars, *Icarus*, *94*(1), 1–13.

Kelly, N. J., W. V. Boynton, K. Kerry, D. Hamara, D. Janes, R. C. Reedy, K. J. Kim, and R. M. Haberle (2006), Seasonal polar carbon dioxide frost on Mars: CO2 mass and columnar thickness distribution, *Journal of Geophysical Research*, *111*(E3), 12.

Kieffer, H. (1979), Mars South Polar Spring and Summer Temperatures: A Residual CO2 Frost, *Journal of Geophysical Research*, *84(B14)*, 8263–828.

Kieffer, H. H. (2007), Cold jets in the Martian polar caps, *Journal of Geophysical Research*, *112*(E08005), doi: 10.1029/2006JE002816.

Kieffer, H. H., T. Z. Martin, A. R. Peterfreund, B. M. Jakosky, E. D. Miner, and F. D. Palluconi (1977), Thermal and albedo mapping of Mars during the Viking primary mission, *Journal of Geophysical Research*, *82*(28), 4249–4291, doi: 10.1029/JS082i028p04249.

Kreslavsky, M. A., and J. W. Head (2005), Mars at very low obliquity: Atmospheric collapse and the fate of volatiles, *Geophysical Research Letters*, *32*, 12,202, doi: 10.1029/2005GL022645.

Lacis, A. A., and V. Oinas (1991), A description of the correlated k distribution method for modeling nongray gaseous absorption, thermal emission, and multiple scattering in vertically inhomogeneous atmospheres, *Journal of Geophysical Research*, *96*(D5), 9027–9063.

Laskar, J., and P. Robutel (1993), The chaotic obliquity of the planets, *Nature*, *361*, 608–612, doi: 10.1038/361608a0.

Laskar, J., B. Levrard, and J. F. Mustard (2002), Orbital forcing of the Martian polar layered deposits, *Nature*, *419*, 375–377, doi: 10.1038/nature01066.

Laskar, J., A. C. M. Correia, M. Gastineau, F. Joutel, B. Levrard, and P. Robutel (2004), Long term evolution and chaotic diffusion of the insolation quantities of Mars, *Icarus*, *170*, 343–364, doi: 10.1016/j.icarus.2004.04.005.

Leighton, R. R., and B. C. Murray (1966), Behavior of carbon dioxide and other volatiles on Mars, *Science*, *153*, 136–144.

Lewis, K. W., O. Aharonson, J. P. Grotzinger, R. L. Kirk, A. S. McEwen, and T.-A.

Suer (2008), Quasi-periodic bedding in the sedimentary rock record of Mars, *Science*, *322*(5907), 1532–1535, doi: 10.1126/science.1161870.

Lewis, S. R. (2003), Modelling the Martian atmosphere, *Astronomy and Geophysics*, *44*, 6, doi: 10.1046/j.1468-4004.2003.44406.x.

Lindzen, R., and A. Hou (1988), Hadley circulations for zonally averaged heating centered off the equator., *Journal of Atmospheric Sciences*, *45*, 2416–2427.

Luhmann, J., R. Johnson, and M. Zhang (1992), Evolutionary impact of sputtering of the Martian atmosphere by O+ pickup ions, *Geophysical Research Letters*, *19*, 2151–2154.

Malin, M. C., and K. S. Edgett (1999), Oceans or seas in the Martian northern lowlands: High resolution imaging tests of proposed coastlines, *Geophysical Research Letters*, *26*(19), 3049–3952.

Malin, M. C., and K. S. Edgett (2003), Evidence for persistent flow and aqueous sedimentation on early Mars, *Science*, *302*(5652), 1931–1934, doi: 10.1126/science.1090544.

Manning, C. V., C. P. McKay, and K. J. Zahnle (2006), Thick and thin models of the evolution of carbon dioxide on Mars, *Icarus*, *180*, 38–59, doi: 10.1016/j.icarus.2005.08.014.

Marinova, M. M., O. Aharonson, and E. Asphaug (2008), Mega-impact formation of the Mars hemispheric dichotomy, *Nature*, *453*(7199), 1216–1219, doi: 10.1038/nature07070.

McKay, C. P., O. B. Toon, and J. F. Kasting (1991), Making Mars habitable, *Nature*, *352*(6335), 489–496.

Mellon, M. T. (1996), Limits on the CO_2 content of the Martian polar deposits, *Icarus*, *124*(1), 268–279.

Melosh, H. J., and A. M. Vickery (1989), Impact erosion of the primordial atmosphere of Mars, *Nature*, *338*(6215), 487–489, doi: 10.1038/338487a0.

Metz, J., J. P. Grotzinger, D. Mohrig, R. Milliken, B. Prather, C. Pirmez, A. S. McEwen, and C. M. Weitz (2009), Sublacustrine depositional fans in southwest melas chasma, *Journal of Geophysical Research*, *114*(E10002), doi: 10.1029/2009JE003365.

Mischna, M. A., J. F. Kasting, A. Pavlov, and R. Freedman (2000), Influence of carbon dioxide clouds on early Martian climate, *Icarus*, *145*(2), 546–554.

Nakamura, T., and E. Tajika (2001), Stability and evolution of the climate system of Mars, *Earth, Planets, and Space*, *53*, 851–859.

Nakamura, T., and E. Tajika (2002), Stability of the Martian climate system under the seasonal change condition of solar radiation, *J. Geophys. Res.*, *107*(E11), doi: 10.1029/2001JE001561.

Newman, W. I., E. M. D. Symbalisty, T. J. Ahrens, and E. M. Jones (1999), Impact erosion of planetary atmospheres: Some surprising results, *Icarus*, *138*(2), 224–240, doi: DOI:10.1006/icar.1999.6076.

Nimmo, F., S. D. Hart, D. G. Korycansky, and C. B. Agnor (2008), Implications of an impact origin for the Martian hemispheric dichotomy, *Nature*, *453*(7199), 1220–1223.

Nye, J. F., W. B. Durham, P. M. Schenk, and J. M. Moore (2000), The Instability of a South Polar Cap on Mars Composed of Carbon Dioxide, *Icarus*, *144*, 449–455, doi: 10.1006/icar.1999.6306.

Paige, D. A., and A. P. Ingersoll (1985), Annual heat balance of Martian polar caps—Viking observations, *Science*, *228*, 1160–1168.

Parrish, J. T. (1993), Climate of the supercontinent pangea, *Journal of Geology*, *101*(2), Pg 215–233.

Peixoto, J., and A. Oort (1992), *Physics of climate*, American Institute of Physics.

Phillips, R. J., M. T. Zuber, S. C. Solomon, M. P. Golombek, B. M. Jakosky, W. B. Banerdt, D. E. Smith, R. M. E. Williams, B. M. Hynek, O. Aharonson, and S. A. I. Hauck (2001), Ancient geodynamics and global-scale hydrology on Mars, *Science*, *291*, 2587–2591.

Pollack, J. B., C. B. Leovy, P. W. Greiman, and Y. Mintz (1981), A Martian general circulation experiment with large topography, *Journal of the Atmospheric Sciences*, *38*(1), 3–29.

Pollack, J. B., J. F. Kasting, S. M. Richardson, and K. Poliakoff (1987), The case for a wet, warm climate on early Mars, *Icarus*, *71*(2), 203–224.

Pollack, J. B., R. M. Haberle, J. Schaeffer, and H. Lee (1990), Simulations of the gen-

eral circulation of the Martian atmosphere 1. polar processes, *J. Geophys. Res.*, *95*(B2), 1447–1473.

Putzig, N. E., M. T. Mellon, K. A. Kretke, and R. E. Arvidson (2005), Global thermal inertia and surface properties of Mars from the MGS mapping mission, *Icarus*, *173*(2), 325–341.

Richardson, M. I., and M. A. Mischna (2005), Long-term evolution of transient liquid water on Mars, *Journal of Geophysical Research (Planets)*, *110*(E9), 3003, doi: 10.1029/2004JE002367.

Richardson, M. I., and R. J. Wilson (2002), A topographically forced asymmetry in the Martian circulation and climate, *Nature*, *416*(6878), 298–301.

Richardson, M. I., A. D. Toigo, and C. E. Newman (2007), Planetwrf: A general purpose, local to global numerical model for planetary atmospheric and climate dynamics, *Journal of Geophysical Research*, *112*(E09001), doi: 10.1029/2006JE002825.

Sagan, C. (1977), Reducing greenhouses and the temperature history of Earth and Mars, *Nature*, *269*, 224–226.

Sagan, C., and G. Mullen (1972), Earth and Mars: Evolution of Atmospheres and Surface Temperatures, *Science*, *177*, 52–56.

Sagan, C., O. B. Toon, and P. J. Gierasch (1973), Climatic change on Mars, *Science*, *181*(4104), 1045–1049, doi: 10.1126/science.181.4104.1045.

Saltzman, B. (2002), *Dynamical Paleoclimatology: Generalized Theory of Global Climate Change*, Academic Press, San Diego, CA, USA.

Segura, T. L., O. B. Toon, A. Colaprete, and K. Zahnle (2002), Environmental effects of large impacts on Mars, *Science*, *298*(5600), 1977, doi: 10.1126/science.1073586.

Segura, T. L., O. B. Toon, and A. Colaprete (2008), Modeling the environmental effects of moderate-sized impacts on Mars, *Journal of Geophysical Research*, *113*(E11007), doi: 10.1029/2008JE003147.

Skamarock, W. C., J. B. Klemp, J. Dudhia, D. O. Gill, D. M. Barker, W. Wang, and J. G. Powers (2005), A description of the advanced research wrf version 2, *NCAR Tech Note*, *NCAR/TN-468+STR*.

Smith, D. E., M. T. Zuber, H. V. Frey, J. B. Garvin, J. W. Head, D. O. Muhleman, G. H. Pettengill, R. J. Phillips, S. C. Solomon, H. J. Zwally, W. B. Banerdt, T. C. Duxbury, M. P. Golombek, F. G. Lemoine, G. A. Neumann, D. D. Rowlands, O. Aharonson, P. G. Ford, A. B. Ivanov, C. L. Johnson, P. J. McGovern, J. B. Abshire, R. S. Afzal, and X. Sun (2001), Mars orbiter laser altimeter: Experiment summary after the first year of global mapping of mars, *Journal of Geophysical Research*, *106*(E10), 23,689–23,722.

Squyres, S. W., and J. F. Kasting (1994), Early Mars—how warm and how wet, *Science*, *265*, 744–+.

Squyres, S. W., J. P. Grotzinger, R. E. Arvidson, J. F. Bell, W. Calvin, P. R. Christensen, B. C. Clark, J. A. Crisp, W. H. Farrand, K. E. Herkenhoff, J. R. Johnson, G. Klingelhöfer, A. H. Knoll, S. M. McLennan, H. Y. McSween, R. V. Morris, J. W. Rice, R. Rieder,

and L. A. Soderblom (2004), In Situ Evidence for an Ancient Aqueous Environment at Meridiani Planum, Mars, *Science*, *306*, 1709–1714, doi: 10.1126/science.1104559.

Stone, P. H. (1972), A simplified radiative-dynamical model for the static stability of rotating atmospheres, *Journal of the Atmospheric Sciences*, *29*(3), 405–418.

Szwast, M. A., M. I. Richardson, and A. R. Vasavada (2006), Surface dust redistribution on Mars as observed by the Mars Global Surveyor and Viking orbiters, *J. Geophys. Res.*, *111*(E11), doi: 10.1029/2005JE002485.

Taylor, F. W. (2010), *The Scientific Exploration of Mars*, Cambridge University Press.

Thomas, P., and P. J. Gierasch (1985), Dust devils on Mars, *Science*, *230*(4722), 175–177, doi: 10.1126/science.230.4722.175.

Tillman, J. E., R. M. Henry, and S. L. Hess (1979), Frontal Systems During Passage of the Martian North Polar Hood Over the Viking Lander 2 Site Prior to the First 1977 Dust Storm, *Journal of Geophysical Research*, *84*(B6), 2947–2955, doi: 10.1029/JB084iB06p02947.

Tillman, J. E., N. C. Johnson, P. Guttorp, and D. B. Percival (1993), The Martian annual atmospheric pressure cycle: Years without great dust storms, *J. Geophys. Res.*, *98*(E6), 10,963–10,971.

Titus, T. N., W. M. Calvin, H. H. Kieffer, Y. Langevin, and T. H. Prettyman (2008), Martian polar processes, in *The Martian Surface: Composition, Mineralogy, and Physical Properties*, edited by Bell, J., III, p. 578, Cambridge University Press.

Toon, O. B., J. B. Pollack, W. Ward, J. A. Burns, and K. Bilski (1980), The astronomical theory of climatic change on Mars, *Icarus*, *44*(3), 552–607, doi: 10.1016/0019-1035(80)90130-X.

Ward, W. R. (1974), Climatic variations on Mars 1. astronomical theory of insolation, *J. Geophys. Res.*, *79*(24), 3375–3386.

Ward, W. R., and D. J. Rudy (1991), Resonant obliquity of Mars?, *Icarus*, *94*(1), 160 – 164, doi: DOI:10.1016/0019-1035(91)90146-K.

Ward, W. R., B. C. Murray, and M. C. Malin (1974), Climatic variations on Mars 2. evolution of carbon dioxide atmosphere and polar caps, *J. Geophys. Res.*, *79*(24), 3387–3395.

Wood, S. E., and D. A. Paige (1992), Modeling the Martian seasonal CO2 cycle. I. Fitting the Viking Lander pressure curves. II. Interannual variability, *Icarus*, *99*, 1–27.

Xie, P., and P. Arkin (1997), Global precipitation: A 17-year monthly analysis based on gauge observations, satellite estimates, and numerical model outputs, *Bulletin of the American Meteorological Society*, *78*, 2539–2558.

Zurek, R. W. (1982), Martian great dust storms: An update, *Icarus*, *50*(2–3), 288–310, doi: 10.1016/0019-1035(82)90127-0.


CALIFORNIA INSTITUTE OF TECHNOLOGY
GEOLOGICAL AND PLANETARY SCIENCES
Labor Bonus et Multus


CALIFORNIA INSTITUTE OF TECHNOLOGY
GEOLOGICAL AND PLANETARY SCIENCES
Labor Bonus et Multus